Arctic Tracer Release Experiment (ARCTREX)

Applications for Mapping Spilled Oil in Arctic Waters

Final Report to the

U.S Department of the Interior Bureau of Ocean Energy Management

Cooperative Agreement No. M13AC00008

Peter Winsor[1] pwinsor@alaska.edu
Harper Simmons[1] hlsimmoins@alaska.edu
Robert Chant[2] chant@marine.rutgers.edu

[1]Institute of Marine Science
College of Fisheries and Ocean Sciences
University of Alaska Fairbanks
2150 Koyukuk Dr., Fairbanks, AK 99775
907.474.7740 (office)
907.474.7204 (fax)

[2]Institute of Coastal and Marine Science
Rutgers University
71 Dudley Rd, New Brunswick, NJ 08901
848.932.3348 (office)

Arctic Tracer Release Experiment (ARCTREX)

Applications for Mapping Spilled Oil in Arctic Waters

This collaboration between
the U.S. Department of the Interior Bureau of Ocean Energy Management,
the University of Alaska Fairbanks,
and Rutgers University

was funded by the

U.S. Department of the Interior
Bureau of Ocean Energy Management
Alaska Outer Continental Shelf Region
Anchorage AK 99503
under Cooperative Agreement No. M13AC00008

as part of the Bureau of Ocean Energy Management
Alaska Environmental Studies Program

And

The Bureau of Safety and Environmental Enforcement (BSEE)

17 November 2017

Citation: Winsor, P., H. L. Simmons, R. Chant, 2017. Arctic Tracer Release Experiment (ARCTREX): Applications for Mapping Spilled Oil in Arctic Waters, Final Report to Bureau of Ocean Energy Management, M13AC00008, OCS Study BOEM 2017- 062, University of Alaska Fairbanks, Fairbanks, AK, 79 pp.

Cover Image: Photo of a surface Rhodamine-WT dye injection in the Chukchi Sea, 2015. Visible in the center of the picture is a surface drifter that was just deployed off the aft deck of the R/V *Norseman II*.

Contents

List of Figures

List of Tables

Abbreviations and Acronyms

ACC	Alaska Coastal Current
ACW	Alaska Coastal Water
ADCP	Acoustic Doppler Current Profiler
ARCTREX	Arctic Tracer Release Experiment
AUV	Autonomous Underwater Vehicle
BBL	Bottom boundary layer
BOEM	Bureau of Ocean Energy Management
BSEE	Bureau of Safety and Environmental Enforcement
BSW	Bering Sea Water
CPH	Cycles Per Hour
CSESP	Chukchi Sea Environmental Studies Program
CTD	Conductivity, Temperature, Depth
ERMA	Environmental Response Management Application
GIS	Geographic Information System
HFR	High Frequency Radar
NASA	National Aeronautics and Space Administration
MODIS	Moderate Resolution Imaging Spectroradiometer
NCEI	National Centers for Environmental Information
NOAA	National Oceanic and Atmospheric Administration
MW	Meltwater
PE	Potential Energy
PSU	Practical Salinity Units
S	Salinity
SSMI	Special Sensor Microwave Imager
SST	Sea Surface Temperature
T	Temperature
TSG	Thermosalinograph
UAF	University of Alaska Fairbanks
UTC	Coordinated Universal Time
VMP	Vertical Microstructure Profiler
WW	Winter Water
WW3	NOAA/NWS/NCEP WAVEWATCH III (WW3) model

Executive Summary

Oil exploration and increased shipping traffic in Arctic waters significantly elevate the risk of oil spills. The Arctic Tracer Release Experiment (ARCTREX) was designed to test the ability of available observational technology to sample a simulated oil spill in the Chukchi Sea and to transmit data to a shore-based, online emergency management application. During the ice-free seasons of 2014 and 2015, three releases of Rhodamine-WT dye were performed and the subsequent plumes were sampled using fluorometers mounted on AUV gliders, a towed Acrobat vehicle, and a vessel-mounted through-flow thermosalinograph (TSG) along with a vessel-mounted ADCP and a free-falling VMP microstructure instrument (providing details on the vertical structure). These data were combined with ongoing industry and University of Alaska ocean observations including moored meteorological instruments and ADCP current meters, satellite-tracked drifters, and extended-range high frequency radars (providing two-dimensional surface current fields). Being able to view incoming data aboard the ship in real time was essential to the adaptive sampling we employed to map the plumes. During the field campaigns, data were transmitted to a version of NOAA's Environmental Response Management Application (ERMA 2015) that is configured for the Arctic region; our successful collaboration with the Arctic ERMA staff provided quick visualization of our simulated oil spill, potentially improving communication and coordination among responders and environmental stakeholders during future events. Subsequent data analysis shows that each dye injection was performed in unique conditions, in areas of: (1) strong stratification with meltwater over cold/salty winter water, (2) active subduction of surface water inshore of a front, and (3) weak stratification caused by a year of record low sea ice. Our results show that dye is dispersed at an average rate of ~7.7 m^2 s^{-1}, and that local ocean dynamics (particularly wind mixing and horizontal density gradients) have a profound impact on the fate of the dye, laterally and vertically, on time scales as short as a couple of hours. The diversity of environments and the extremely rough weather experienced during the field experiments allowed us to fully evaluate the performance of the instruments; the TSG and the towed undulating Acrobat vehicle are capable of tracking dye over time in great detail while being able to operate in stormy seas with significant wave heights approaching three meters. Dye was distributed throughout the surface mixed layer and, in one case, was subducted below the surface layer, requiring instruments capable of sustained subsurface measurements.

1. Applications for Mapping Spilled Oil in Arctic Waters

1.1. Overview

Oil exploration and increased shipping through Arctic waters bring with them the increased possibility of oil spills. Previous oil spills in other areas have demonstrated the utility of real-time data in modeling and directing the oil spill response, and it was an open question whether the challenges created by the Chukchi Sea's unique characteristics such as sea ice and extreme weather would allow the collection of this critical data. This study lays the groundwork for answering this question by using simulated oil spills to assess this capability in the Chukchi Sea.

The core of ARCTREX is the field experiments performed aboard the R/V *Norseman II*—a series of dye releases and subsequent surveys with a suite of instruments. The releases were performed during the ice-free season in the vicinity of oil leases where an oil spill might likely occur. The study area is physically complex with rapidly changing weather and oceanic conditions and interannual variability that created diverse experimental conditions. The area also presents challenging logistical complications due to its remoteness and extreme weather. These challenges will be detailed in this report, as will assessments of the capabilities of the instruments we used for sampling. We stress that a dye release is not an ideal or even realistic simulation of oil in water, but does enable measurement of dispersion in the area of interest while it provides an opportunity to track a known substance over time and space with modern real-time enabled observational technology.

Another important aspect of this study is our collaboration with the Bureau of Safety and Environmental Enforcement (BSEE) and NOAA's Environmental Response Management Application ERMA (ERMA 2015) configured for the Arctic region, with the goal of feeding our real-time data into their response system. Real-time field data and prediction of the plume evolution is critical for proper response to an oil spill. ERMA is a web-based GIS tool that assists both emergency responders and environmental resource managers in dealing with incidents that may harm the environment. ERMA integrates and synthesizes data—some of which happens in real time—into a single interactive map, providing quick visualization of the situation and improving communication and coordination among responders and environmental stakeholders.

ARCTREX also advances fundamental knowledge of the Chukchi's physical oceanography, including the dynamics of fronts and wind mixing. The field program was designed to provide multiple measurements of ocean surface properties using different observational platforms, and to characterize passive dispersion through the direct measurement of advection and patch spreading at small spatial and temporal scales. Measurements of ocean turbulence and microstructure in concert with highly detailed observations of dispersion aids in the understanding of how this high-latitude shelf system evolves during the ice-free season. To our knowledge, no dye release study has previously been performed in this area, and as such we view this project as a test bed for future studies.

1.2. Project Goals

- Develop a better understanding of small-scale transport processes important to fate and effects modeling used in oil impact analysis.

- Develop instrument and real-time mapping protocols that can guide oil spill responders in the event of a small offshore spill.

1.3. Scientific Project Objectives

- Conduct field tests of the dispersal and tracking of nontoxic Rhodamine dye off the Chukchi coast.

- Develop, test, and deploy instrumentation for Autonomous Underwater Vehicles (AUV) and other instrumentation that can be customized for use in the Arctic to detect the spatial and temporal locations of surface and subsurface spills.

- Track the dispersed dye plume by incorporating input from the AUVs, towed CTDs, and other real-time data collection sensors in the Chukchi Sea (e.g., surface currents from HF Radar, towed CTDs, drifters, real-time WRF high-resolution wind fields, data from meteorological buoys and other offshore instruments) to assess the fate and transport of the dye plume.

- Evaluate the effectiveness of the suite of instruments to track the released dye under diverse environmental conditions.

- Calculate parameters that quantify small-scale transport processes based on measurable oceanographic and meteorological data.

2. Northeastern Chukchi Sea—Physical Setting

The Chukchi Sea borders the northern coast of Alaska (Figure 1). The shallow (~50m) Chukchi shelf extends ~800 km northward from Bering Strait to the shelf break at the 200 m isobath. Though considered part of the western Arctic Ocean, the Chukchi shelf is oceanographically linked to the Pacific Ocean via mean northward flow through Bering Strait, which is sustained by a large-scale pressure gradient between the Pacific and Atlantic Oceans (Coachman et al. 1975; Aagaard et al. 2006). Also important to the Chukchi Shelf is the sea ice that typically covers it from October to May; the spring retreat of ice occurs earlier and fall ice formation is delayed there in comparison to most other Arctic shelves because of the northward heat flux through the strait; in September, sea ice is far from the ARCTREX study area. Major bathymetric features near the ARCTREX study area include Central Channel to the west, Hanna Shoal to the north, Barrow Canyon to the east, and the Alaska coast along the southwest.

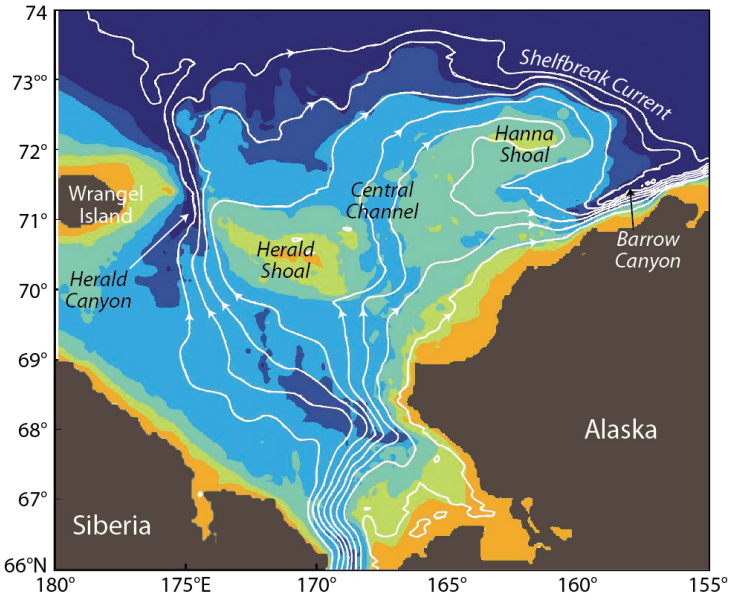

Figure 1. Mean depth-integrated streamlines in the Chukchi Sea, after Spall (2007). Streamlines are white, bathymetry is shaded, and major bathymetric features are labeled.

Figure 1, from Spall (2007) is derived from model results, but it illustrates the mean circulation over the shelf. Although the mean flow is nominally northward over much of the shelf, the bulk of the transport occurs along the canyons. Water flushing the central and western Chukchi Sea then moves eastward north of Hanna Shoal, where a portion of it turns southward along the east side of Hanna Shoal and eventually enters the head of Barrow Canyon, according to models (Winsor and Chapman, 2004; Spall 2007). Mean current speeds within Herald and Barrow canyons are swift (~25 cm s^{-1} or larger), more moderate in the Central Channel (~10 cm s^{-1}), and generally <5 cm s^{-1} elsewhere (Weingartner et al. 2005; Woodgate et al, 2005; Pickart et al. 2010).

The ARCTREX study area is influenced by several of the system's current pathways and that, in turn, creates the mosaic of water masses encountered by our hydrographic surveys and described historically (Paquette and Bourke 1974; Coachman et al. 1975; Johnson 1989). Melting sea ice creates a surface layer of meltwater (MW) that is fresh and cold (Aagaard 1988), but warms as the season progresses; this water is formed in place by melting or advected from the north. Two water masses are advected from the south by Bering Strait inflow—the fresh, warm, highly stratified Alaska Coastal Water (ACW) and the cooler, less stratified Bering Sea water (BSW) also called Chukchi Summer Water (Gong and Pickart 2015, 2016). The Alaska Coastal Current (ACC) brings ACW northwestward along the coast (Aagaard 1988; Münchow and Carmack 1997), but its influence can spread across the shelf during the upwelling events that occur in summer and fall (Weingartner et al. 2015). The ACC's northwestward transport is at maximum in July, and in September is transitioning to its fall condition of near zero transport (Weingartner et al. 2017). BSW is offshore of ACW, spreading eastward from the Central Channel along its entire length (Weingartner et al. 2013). As these waters flow eastward, they encounter dense (cold, salty) bottom waters that, because they were formed during

the previous winter over the northern Bering and Chukchi Seas (Aagaard 1988), are called winter water (WW). The model results (Figure 1) suggest that this dense water is most likely from the east side of Hanna Shoal.

In contrast to other continental shelves, tidal currents in the Chukchi Sea are weak (Sverdrup 1926; Hunkins 1965; Danielson 1996), but there are other processes that affect currents on the time and space scales of ARCTREX. While currents in the mean are forced by large-scale pressure gradients (Woodgate et al. 2006), current variations can be wind-forced. However, the contribution to the vertically averaged momentum balances by instantaneous winds is insignificant compared to geostrophic flow from pressure gradients generated by wind-driven convergences and divergences (Weingartner et al. 2013). Atmospheric forcing also generates continental shelf waves that propagate northward from the Bering Strait, though these are more significant within the ACC than at mid-shelf locations like the ARCTREX study area (Danielson et al. 2014). In addition, wind-generated surface gravity waves create Stokes drift, which can be substantial on the Chukchi Shelf depending on the depth. Weingartner et al. (2017) found that Stokes drift makes a relatively small contribution to the momentum balance of 1 m drogued drifters, but integrated over a prolonged wind event, it can account for 20% of drifters' displacement over 6 days. Undrogued drifters can travel in the opposite direction from even 1 m drogued drifters under strong wind conditions (personal observation).

As we will show, dispersion in the Chukchi Sea is greatly influenced by lateral density fronts, which are prominent features of the Chukchi Shelf—especially north of ~71.5°N (Weingartner et al. 2015). In general, fronts are created by lateral differences in surface forcing and advection and are maintained in the vertical by turbulent mixing; they slump from the vertical, causing local instabilities and horizontal mixing (Ferrari and Bocaletti 2004). Timmerman and Winsor (2013) found that in the Chukchi, horizontal temperature, salinity, and density variability extends down to O(1) km sub-mesoscales—the scale of ARCTREX's dye patches—and that lateral isopycnal slumping of the fronts acts to restratify the water column north of the fronts. Lu et al. (2015) observed fronts in the Chukchi consisting of MW over WW in the north and BSW in the south, with lateral influxes (not vertical mixing) generating intrapycnocline lenses and layers of BSW between the MW/WW layers. Their idealized numerical model results showed that instability of the surface front generates eddies and meanders that give rise to these subsurface features. This complex of water masses is precisely what is seen during ARCTREX's dye injection #1.

There are a number of processes that can alter the dispersion rate, including time dependence (Fischer et al. 1979; Young and Rhines 1982), incomplete vertical or lateral mixing (Bowden 1965; Okubo 1973), and lateral shear (Fischer 1972; Sumer and Fischer 1977); see for example Geyer et al. (2008) for discussion. Kawaguchi et al. (2015) found the minimal dissipation rate of turbulent kinetic energy in the bottom layer is consistent with the area's weak tides. The strong stratification of the northern Chukchi Shelf (buoyancy frequencies in the pycnocline are greater than 10 cph) suppresses vertical mixing, so that MW moves over WW with little exchange of heat, salt, and dissolved nutrients. However, near-inertial internal waves and shear are generated by summer

storms and erode the pycnocline (Rainville and Woodgate 2009), and could enhance turbulent energy even in deep water such as the Arctic Ocean interior (Martini et al. 2014). Observations in the two-layer system closer to the ice edge in September 2013 demonstrated that when the winds are calm and the water is stratified, internal gravity waves propagate through the water column, causing mechanical overturning near pycnocline (Kawaguchi et al. 2015). During gale force winds, turbulence deepened the surface homogeneous layer. They also noted that drifting buoys moved with oscillations at the inertial period of 12.5 hours.

3. Methods

3.1. Dye Releases

The main purpose of the ARCTREX experiment was to map the evolution of a dye plume over time and space in order to simulate an oil spill event and to provide real-time data to the Arctic ERMA system. To do this, we conducted purposeful injections of a fluorescent dye, Rhodamine-WT, as a passive ocean tracer. We conducted two successful dye injections in September 2014 and another in September 2015, all in the upper mixed layer (Table 1). A deep-water release was attempted in 2015 but was not successful (see below) so was not given an identifying number.

Table 1. Summary of dye injections

Id	Date and Time (UTC)	Latitude (°N)	Longitude (°E)	Depth (m)	S (PSU)	T (°C)	Surveys	Length (hours)
1	9/9/2014 23:05	71.2985	–162.6550	8	28.8	1.45	23	75
2	9/15/2014 03:30	70.6814	–162.0338	10	31.0	2.75	11	30
	9/7/2015 05:00	71.6270	–162.9752	35.5	36.2	0.8		
3	9/9/2015 04:09	70.7183	–162.2080	5	31.1	6.8	19	42

To prepare for each dye injection, we first conducted hydrographic surveys of the study area to define the 3-D structure of the density field using a towed Acrobat vehicle and AUV gliders, and characterized turbulence with microstructure measurements (discussed in detail later). A solution of 50 kg of Rhodamine-WT in a 20% water solution was mixed with propanol to achieve the anticipated in situ density. Use of this mixture together with rapid ~1000 to 1 dilution as the dye solution was injected through a diffusing nozzle precluded any subsequent anomalous density-driven flow. The dye was injected by pumping it through a hose attached to the CTD rosette frame suspended below the ship. The surface injections occurred in the upper 5–7 meters of the water

column, in middle of the surface mixed layer. The dye quickly spread vertically to occupy the entire mixed layer, typically the upper 10–15 m of the water column. Dilution limited the duration of the tracer experiments to 1–4 days.

Figure 2. Photo of a surface Rhodamine-WT dye injection, Chukchi Sea. Visible in the center of the picture is a surface drifter that was just deployed off the aft deck of the R/V *Norseman II*. The drogue sank within 1 minute of deployment.

Surveys of the dye patch were performed with Chelsea Ltd. Aquatracka III fluorometers mounted on a variety of instruments (see section 3.2). The Aquatracka III is able to detect Rhodamine-WT to 1 part in 10^{11} by weight, which was the expected background signal, and has a 4 decade logarithmic output. At low dye concentrations, $\sim 10 \times 10^{-11}$ signal contamination is possible due to fluorescence from a surface chlorophyll bloom. To estimate and remove this spurious signal, a separate chlorophyll fluorometer was used. A dye concentration $>500 \times 10^{-11}$ will produce a spurious chlorophyll signal but such concentrations persisted for only a few hours. Steaming at 6 knots, the dye patch was surveyed over 36–72 hours with a minimum of 11 separate surveys of each injection's patch. Real-time data from instruments allowed us to anticipate the initial dye patch displacement and to adjust the ship course in order to achieve evenly spaced tracks through the patch. Integrated transect data from the acoustic Doppler current profiler (ADCP) and Acrobat also helped adjust the ship position relative to the water column to a common reference time during subsequent data analysis.

The surveys continued until the dye concentration signal to noise ratio was ~3. When 50 kg of dye is evenly dispersed over a volume 10 km × 10 km × 10 m, the average concentration is 4×10^{-11}; that is, a signal/noise ratio of ~4. The Aquatracka III fluorometer was able to perform as expected over the duration of the surveys, displaying sensitivity to the dispersed dye concentration over several orders of magnitude.

For dye injection #1 in 2014, after patch 16, we chose not to track the whole long tail of dye, choosing instead to spend our time performing more surveys of the patch. We ended our surveys when the dye patch was too diffuse and large to survey completely over a 6-hour period and concentrations were consistently below 10^{-10}. In 2015, we surveyed the dye injection #3 for 28 hours, at which time the dye concentration was ~10^{-10}.

Analysis of the dye was conducted according to the methods outlined in Sundermeyer and Ledwell (2001) and Geyer et al. (2008) and is summarized as follows. Each patch survey consisted of a series of transects across the dye. Distortions in the shape of a patch might be caused by the advection that occurs during the time it takes to survey different areas of it. Therefore, each transect across the dye patch was adjusted for advection using velocities from the shipboard ADCP data; this translation to a central time produced synoptic realizations of the dye patches. The data were then interpolated to a regular grid, which enabled an estimate of the inventory of dye for each patch (also called the total mass, or the 0^{th} moment), the position of the dye's centroid (the first moment), the dye's variance (the second moment). Mean physical properties of the dye patch, such as temperature or salinity, were calculated by integrating over the patch:

$$\overline{P} = \frac{\int CP\,dV}{\int C\,dV}$$

Where P is the parameter (salinity or temperature) and C is the dye concentration.

The experiment in 2015 diverged from our planned operating procedure because during our first dye injection (at the bottom), flooding occurred in the analog-to-digital converter that allows the Acrobat's Rhodamine fluorometer to send data up the wire to the deck unit in real time. The dye release was successful, but tracking of the deep dye patch failed because in addition, the AUV glider was damaged and unavailable, and degrading weather conditions sidelined the VMP microstructure instrument. Because the dye was at depth, even using the TSG for sampling was impractical. The loss of the Acrobat's fluorometer also impacted the second dye release in 2015, dye injection #3, but because that injection was at the surface, we were able to sample that dye with the hull-mounted TSG. As unfortunate as this event was, it illustrates the difficulties of Arctic fieldwork, and serves as a caution to those planning oil spill response.

3.2. Observational Technologies

3.2.1. Ship-Based Dye and Hydrographic Measurements

Acrobat towed vehicle. Underway surveys using the small Acrobat towed vehicle (Figure 3) were the primary method of measuring the evolution of dye concentrations after the injections. The Acrobat enabled continuous hydrographic surveys at 5–7 knot tow speed, generating large spatial coverage over short time periods. The vehicle was piloted from the ship and was typically flown to within 1–3 m of the surface and bottom. It was equipped with a large dynamic range Chelsea Ltd. Aquatracka III Rhodamine fluorometer sampling at 6 Hz, which, in concert with a FastCAT Seabird CTD sampling

at 16 Hz and a triplet Wetlabs EcoPuck sampling at 8 Hz, enabled us to perform repeated tow sections along and across the dye plume over time. The Acrobat transmitted data through a faired Kevlar cable to an onboard deck unit, and data was stored and plotted on the ship, so we were able to adapt the sampling scheme to real-time conditions. The Acrobat system was critical to our success in tracking dye over the entire water column and provided us with real-time data to allow for adaptive sampling of the growing dye patch. Once deployed, this system was also functional during high sea states.

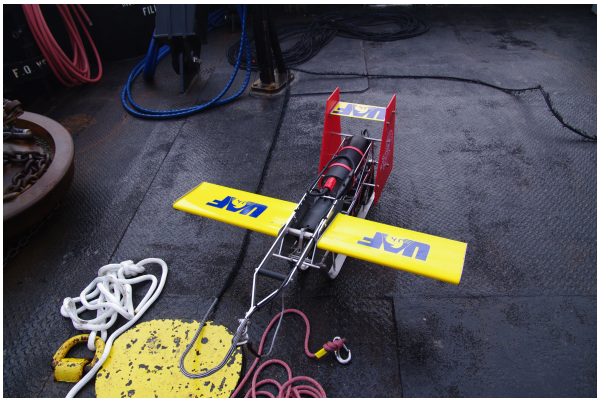

Figure 3. Photo of the Acrobat towed vehicle. Also visible on the aft deck of the R/V *Norseman II* is the faired Kevlar cable that allows for real-time data transfer to the operator.

Through-flow ThermoSalinoGraph. We installed the same model large dynamic range Rhodamine fluorometer (Chelsea Ltd. Aquatracka III sampling at 1 Hz) in the R/V *Norseman II* vessel's through-flow ThermoSalinoGraph (TSG) system, and that enabled us to sample near-surface CTD and dye concentrations continuously while underway. The TSG system collected salinity, temperature, and Rhodamine dye concentration every 5 s with the intake located at ~3 m depth; with a typical survey speed of 6 knots, our horizontal resolution from the TSG was ~30 m. This system performed excellently and was critical to the success of our fieldwork. It provided us with the capability to map dye absence, presence, and concentrations continuously and, by measuring hydrographic surface properties, gave the detailed near-surface measurements of horizontal density fronts that proved critical in understanding the dye's movement. The system was on continuously while we operated the ship, and the data was plotted in real time on a monitor onboard. Because it is constrained to the surface, its drawback was that it could not detect dye when the dye was subducted (dye injection #2) or released at depth (dye injection #4). The surface maps in the Results section were created using TSG data.

CTD/Rosette system. A third CTD system was also used during the sampling: a Seabird SBE55/SBE19+ CTD/Rosette system that was lowered from the surface at specific locations. It was used before the injections to determine the target density of the injection depth so that the Rhodamine dye could be made neutrally buoyant. In addition, during the dye release, the injection hose was attached to the rosette frame so that it could be lowered to that known depth/density surface. The CTD system enabled us to disperse the dye at a known depth while monitoring its salinity and temperature properties, but

because the ship had to stop when it was deployed, it had no utility during the dye surveys.

3.2.2. Autonomous Underwater Vehicles

Autonomous Underwater Vehicles. Slocum's electric Autonomous Underwater Vehicle (AUV or glider) surveys independently of a ship in a vertical sawtooth pattern by using changes in its buoyancy to generate forward movement (Webb et al. 2001); it obtains GPS positions upon surfacing, so it can navigate underwater by dead reckoning a compass bearing to a waypoint provided by operators on shore. Sampling is thus independent of the ship operations and weather conditions. Our gliders were each equipped with a Sea-Bird Electronics (SBE) Glider Payload CTD (GPCTD) and a Rhodamine fluorometer with a 1 Hz sampling rate. A glider's typical mean horizontal speed is 30–40 cm s^{-1} and the mean depth of the survey areas in the Chukchi Sea is ~40 m, which resulted in a survey resolution for hydrography and dye concentration of ~1 m vertically and ~300 m horizontally. Based on previous experience, we expected the glider's sampling to be faster than the evolution of submesoscale features commonly found in the Chukchi Sea (Timmermans and Winsor 2013).

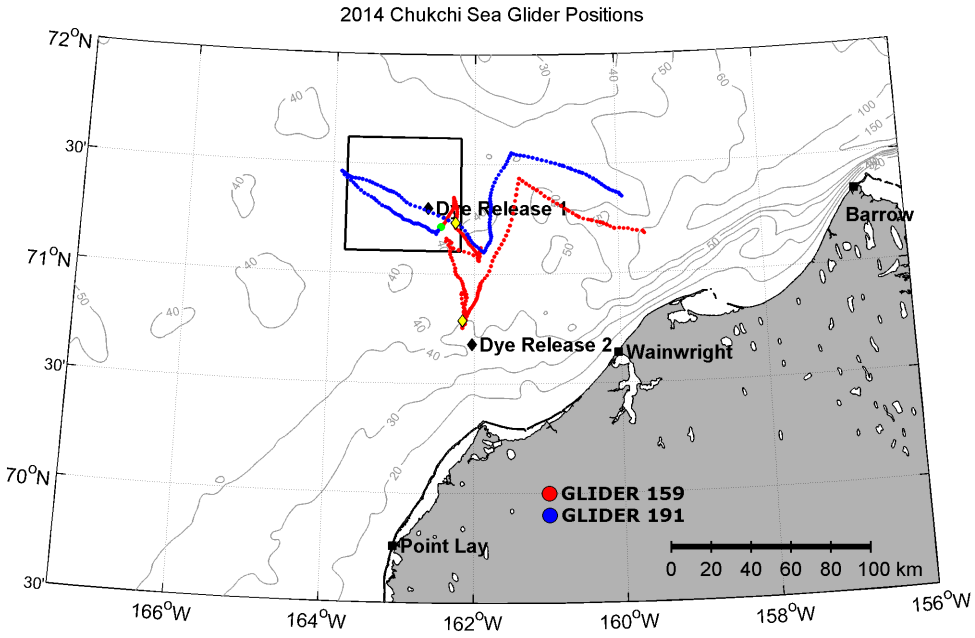

Figure 4. Glider positions during the 2014 field experiment.

For the 2014 ARCTREX field experiment, we deployed two gliders at the site of dye injection #1 (Figure 4) and programmed them to surface hourly, hoping that they could respond quickly to the dye patch position. However, the dye patch evolved faster than the gliders were able to make forward progress. Despite their ability to detect dye both at the surface and subsurface (Figure 5), we learned that individual gliders are not able to map a dye plume in time and space resolution needed for dispersion calculations. In 2015, no

gliders were deployed because the Rhodamine-equipped AUV glider had compass issues, probably due to damage caused in shipping. No glider transects or maps are included in the Results section of this report for these reasons.

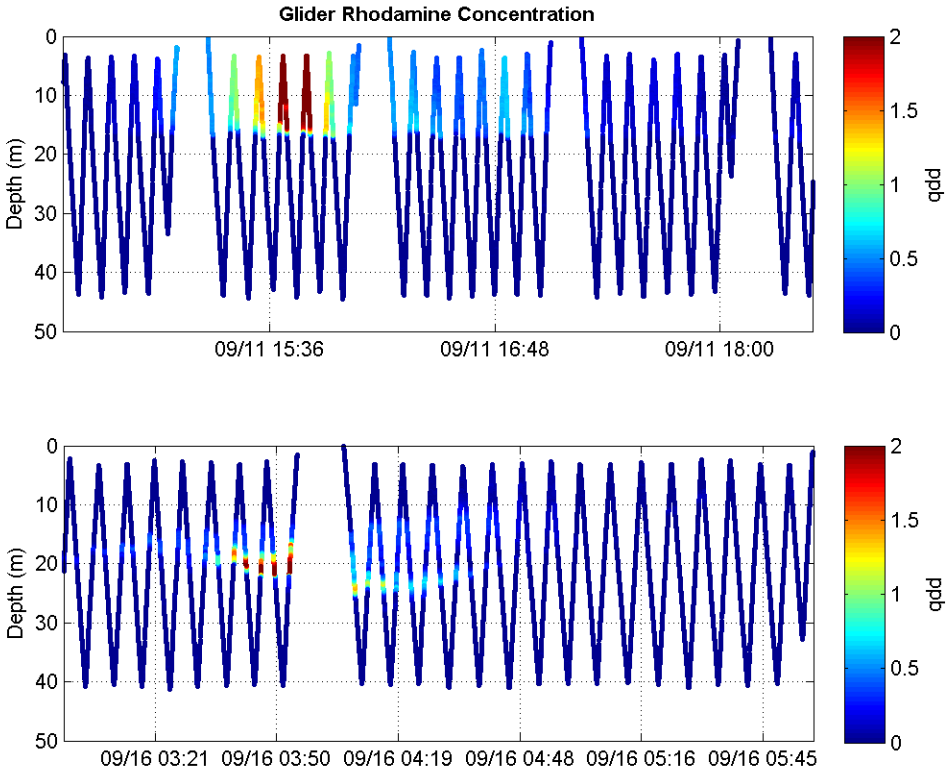

Figure 5. Vertical sections of dye concentrations measured by AUVs during dye injections #1 (top) and #2 (bottom).

3.2.3. Satellite-Tracked Drifters

We deployed satellite-tracked drifters (Microstars, Pacific Gyre Inc.) at the injection sites. Each drifter was drogued at 1 m depth and had a surface sphere that contained a temperature sensor, GPS, and Iridium satellite module for real-time data transfer to PacificGyre via Iridium SBD format. The drogue-to-surface float drag ratio is 50:1, which ensures that the floats represent ocean currents at the 1 m drogue depth. We expected the drifters to transmit the real-time position of the centroid of the dye patch automatically to onshore stations, but the trajectories of the drifters and dye diverged, as will be discussed in the Results section. Horizontal dispersion as measured by drifters was calculated by assembling the pairwise distance between drifters (Weingartner et al. 2015), so it could only be calculated when the entire cluster returned data; if drifters entered the water late or died early, this shortened the time over which dispersion could be calculated.

In 2014, a single drifter was deployed upon arrival at the first injection site to help characterize the currents there; this drifter eventually died in the sea ice four months later. Another drifter was deployed immediately before dye injection #1, with 15 more released during the injection itself. For dye injection #2, those 15 drifters were recovered and re-deployed at the second site with 13 additional drifters, for a total of 45 drifter deployments. These drifters sampled at five-minute intervals in hopes of computing dispersion via cluster analysis. However, we later discovered that waves breaking over the surface floats add noise to the GPS positions that is accentuated by the short sampling interval, making those calculations impractical. Hourly averaged position was used instead.

After the 2014 field experiment, all drifters were switched to hourly sampling and left to characterize wide-scale Chukchi circulation as part of BOEM's Chukchi and Western Beaufort Circulation Study; all initially traveled northeast along Barrow Canyon but at the shelf break turned west, crossed the Chukchi Sea, and headed for the area near Wrangel Island, Russia (not shown); one of these drifters lasted until January 2016 and went as far west as 150°W, which is another story.

In 2015, one drifter was deployed before dye injection #3, and 9 more were deployed during the injection itself, for a total of 10. All reported sea surface temperature and position hourly, and all were left in the water after the 2015 field experiment. They also traveled west, many of them beaching on the Siberian coast; the last of these also died in January 2016.

3.2.4. Microstructure

Vertical microstructure profiler. We performed turbulence profiling using a lightweight VMP-250 vertical microstructure profiler built by Rockland Scientific. The profiler free-falls through the ocean interior, connected by a slack tether to avoid any drag or vibrations on the instrument; it was deployed and recovered using a small electric winch on the R/V *Norseman II*. The VMP measures profiles of the hydrographic finestructure and velocity microstructure, which can be used to quantify the rates of turbulent dissipation, ε, in the ocean (Gregg 1999; Lueck et al. 2002). These measurements allow us to measure the vertical component of the turbulent mixing, K_v, using the method of Osborn (1980). Velocity microstructure was acquired using dual airfoil probes that measure shear and a FP07 thermistor for temperature; a Turner designs CYCLOPS-7 Rhodamine WT sensor measured dye concentration. The noise level for ε measured by the VMP is $\sim 5 \times 10^{-10}$ W kg^{-1}, as determined from examination of spectra in quiet patches.

A summary of VMP deployments is shown in Table 2 and Figure 6. In 2014, the VMP was deployed once before the first injection but was lost during the second deployment, with no data returned. In 2015, three deployments were performed before that year's first dye injection, but bad weather precluded any more. The VMP profiles allowed us to characterize turbulence in the ocean, but it was not practical to use during the dye surveys because the ship has to stop during profiles.

Table 2. Summary of VMP stations.

Year	Station	Start Date and Time (UTC)	Latitude (°N)	Longitude (°E)	Number of Casts
2014	1	9/9/2014 20:33	71.2095	–162.4350	5
2015	1	9/7/2015 02:50	71.6548	–162.9780	12
2015	2	9/7/2015 20:30	71.5851	–162.8719	20
2015	3	9/9/2015 02:51	70.7117	–162.2248	10

3.2.5. Wind, Waves, and Currents

High frequency radars. To obtain information about the background circulation over our study area, we utilized land-based high-frequency Radars (HFRs). The HFRs were deployed and maintained through the Bureau of Ocean Energy Management (BOEM) Grants 764 M12AC000008 and M09AC15207, the Alaska Ocean Observing System (AOOS)/U.S. Integrated Ocean Observing System, and the Alaska Coastal Impact Assistance Program (Dr. Weingartner, PI). Surface currents in the upper 1–2 m of the water column provided by HFR fields were mapped on a 6 km grid every hour during both the 2014 and 2015 experiments (Figure 6). The two-dimensional current vectors were displayed online (www.chukchicurrents.com) and were updated in real time, so were available during field operations. The HFR data allowed us to identify circulation patterns and convergent features (fronts) in real time from the ship.

However, Figure 6 also illustrates one of the disadvantages of HFR measurements in regards to the ARCTREX experiment. Note that there is a data gap between Point Lay and Wainwright where all the dye releases occurred. This data gap occurs because the HFR stations are too far apart given the limitations of the Arctic's power grid infrastructure (Weingartner et al. 2012; Fang et al. 2015). In 2015, a new station was established on Icy Cape to close this gap, but as of this time, processing of 2015 HFR data is not complete and should be considered preliminary. We have attempted to reduce this gap by using daily averages rather than hourly maps in the following sections, but the utility of HFR current maps is still limited.

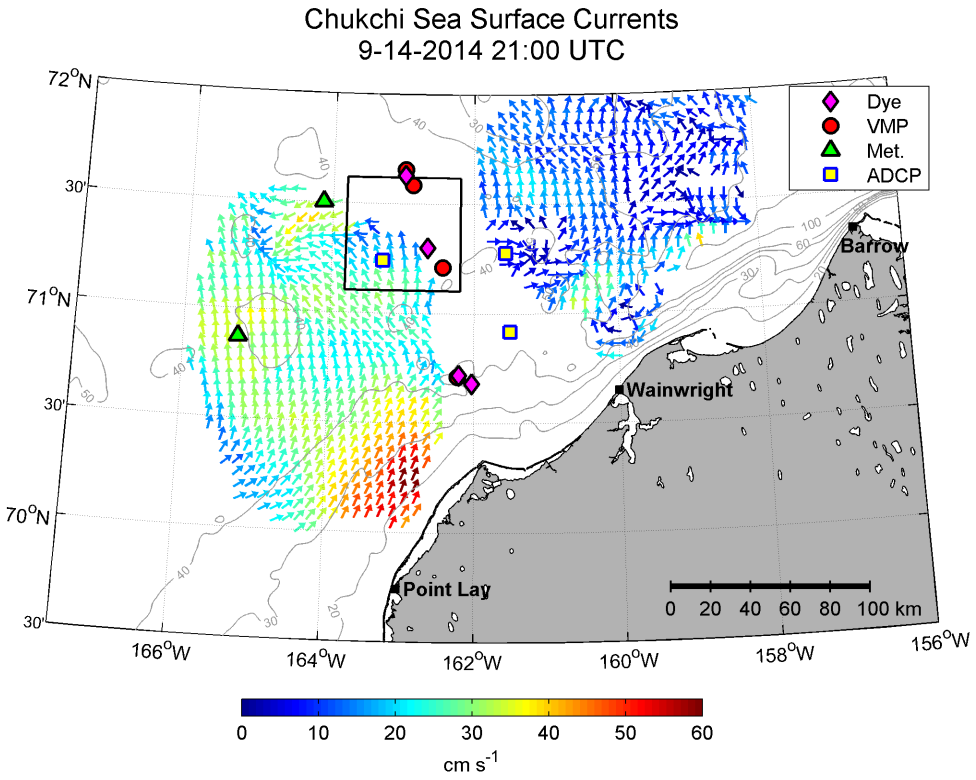

Figure 6. An example of surface currents mapped by the Chukchi Sea HFR network. Surface current vectors at 2100 UTC September 14, 2014, are colored according to current magnitude. Bathymetry is contoured at 10 m intervals (gray). The black box shows the location of CSESP's Burger study area, and pink diamonds show the dye release sites in 2014 and 2015. Additional instrumentation includes VMP stations (red), ADCP moorings (yellow), and meteorological buoys (green).

The R/V *Norseman II* is outfitted with a shipboard downward-looking ADCP current meter. Data were displayed on a screen during the cruise and were processed afterward using standard methods. Velocity data were corrected for ship heading and velocity and were edited for bad values.

Data from a variety of moored instruments were provided by the industry-sponsored Chukchi Sea Environmental Studies Program (CSESP), also archived as Accession #0164964 at the NOAA National Centers for Environmental Information (NCEI). Meteorological buoys and moored ADCP and CTD instruments were located at various locations around the Chukchi Sea, primarily at the oil and gas lease prospects called Klondike and Burger by the ConocoPhillips and Shell, respectively (Table 3; Figure 6). The Meteorological (Met) buoys were deployed during the ice-free seasons only; possible measured variables include sea surface temperature (SST), wind, surface current, and waves. ADCP data were processed by ASL Environmental Services (Mudge et al. 2017); currents were output at surface, mid-water, and bottom depths only, making determination of vertical shear imprecise.

Table 3. Mooring dates and locations.

ID	Type	Start Date	End Date	Latitude (°N)	Longitude (°E)
Klondike	Met	08/03/2014	10/08/2014	70.8718	–165.2459
Klondike	Met	07/21/2015	10/13/2015	70.8722	–165.2480
Burger	Met	08/20/2014	10/07/2014	71.5020	–164.1335
Burger	ADCP	08/5/2014	10/5/2015	71.2394	–163.2800
Site05	ADCP	08/6/2014	10/2/2014	70.9166	–161.4996
Site08	ADCP	10/16/2014	10/5/2015	71.2767	–161.5608

3.2.6. Models and Remote Sensing

Moderate resolution imaging spectroradiometer (MODIS) remote sensing. Lastly, we utilized daily Level 2 Sea Surface Temperature (SST) product from NASA's MODIS sensors to allow us to map surface thermal gradients and ocean fronts before and during our field experiments. These satellite images, together with the surface HFR current fields, aided us in determining the location for our dye release experiments. The MODIS imagery also helps visualize the complex frontal patterns between the nearshore, relatively warm ACC and colder offshore water masses.

WaveWatchIII. For the period in 2015 when the industry meteorological buoy did not measure wave data, we acquired approximations of it from NOAA's publicly available WaveWatchIII (WW3) model output (Tolmen 1997). WW3 produces NOAA's operational ocean wave predictions and is also available as a hindcast. These have been shown to accurately reflect wind and wave measurements during the vast majority of conditions, the exception being storm events where peak wave heights may be underestimated by 1–2 m (Pingree-Shippee et al. 2016). WW3 wave output was interpolated to the location of the Klondike ConocoPhillips buoy: 70.8722°N, –165.248°E.

3.3. Online Data Display

During the experiment, data had to be transmitted to shoreside stations in order to be displayed on the web. Previous experiments by the University of Alaska Fairbanks (UAF) have used Google Maps for data display, but that proved unworkable for this project because Google Maps lacks background map tiles at the spatial scales of the dye patches. Because of this, Arctic ERMA's data display capabilities were indispensable. Transmission methods for our data differed by instrument and are summarized below.

Gliders. Decimated data files were transmitted via Iridium to the onshore glider server, which is currently an Amazon cloud server administered by UAF. This preliminary data was automatically harvested by UAF, and glider positions were processed into tracklines in Google's KML format by Python scripts on a Linux server. These KML files were copied to Arctic ERMA servers and converted to shapefiles for display in their system. The original data files also contain temperature, salinity, and Rhodamine dye concentration that were not included in the GIS files; instead, these data were dynamically displayed as vertical sections in time by PHP scripts on UAF's website (http://www.ims.uaf.edu/artlab/), providing near real-time oceanographic data.

Drifters: Data was transmitted via Iridium to PacificGyre, which posted it on its website. Automated scripts similar to those for the gliders created a KML file for each drifter, and these were copied to Arctic ERMA servers, converted to shapefiles, and displayed by them. PacificGyre's data server also provides data in JavaScript Object Notation (JSON) format, a possible alternative format in the future.

The conversion of raw dye concentration data into gridded, synoptic realizations of the dye patch for delivery to Arctic ERMA was a manual process aboard the R/V *Norseman II*. After 1–4 surveys of the dye patch, time limits for each new patch were determined. The relevant dye concentration data were extracted, gridded, and smoothed for contouring; the contours were then saved as polygons to shapefiles, one for each patch. These shapefiles were delivered to the ERMA server via SFTP as soon as they were generated. The same general process was used in 2014 and 2015, although—based on the experience in 2014—details of the shapefiles and metadata were changed to allow for an automatic update of Arctic ERMA when shapefiles were delivered.

3.4. Protocol

Details varied by instance, but the basic protocol followed for a dye-tracking experiment can be summarized as follows:

1. We used wide-scale measurements of MODIS and HFR to choose the injection sites based on likely oil spill locations and physical features of interest.

2. At an intermediate scale, Acrobat, glider, and shipboard ADCP transects were performed to define the physical setting.

3. A single drifter was deployed to give an initial prediction of the dye's trajectory.

4. At the chosen injection site, VMP profiles were performed to define the mixing profile for later analysis.

5. A CTD profile was performed to define the target density for dye solution. The dye solution was mixed in accordance with the measured density.

6. The dye was released with a cluster of drifters.

7. Continual surveys using ship-based measurements were performed to track the dye patch's movement and to define the dye inventory. Surveys were performed with:

    a. Shipboard ADCP

    b. Towed Acrobat

    c. Ship's TSG

8. Drifter and glider position data were automatically transmitted to Arctic ERMA servers. Shapefiles of dye concentrations were manually produced on the ship and transmitted to Arctic ERMA.

4. Physical Setting during Field Experiments

4.1. 2014 Field Experiment

Figure 7 shows the study area for the 2014 observational effort in the northeastern Chukchi Sea. The ship track for the 2014 experiment is shown in dark gray, and includes the two dye release surveys (in black boxes) and "butterfly" surveys around the locations of each dye injection. Also shown in Figure 7 is the average SST field obtained from NASA MODIS satellite imagery. The warmer ACW of the Alaska Coastal Current can be seen in the southeast portion of the map, and in the north is the colder MW. Note that the transition from warm to colder waters is not linear but rather contains local maximums and minimums suggestive of the meandering frontal system.

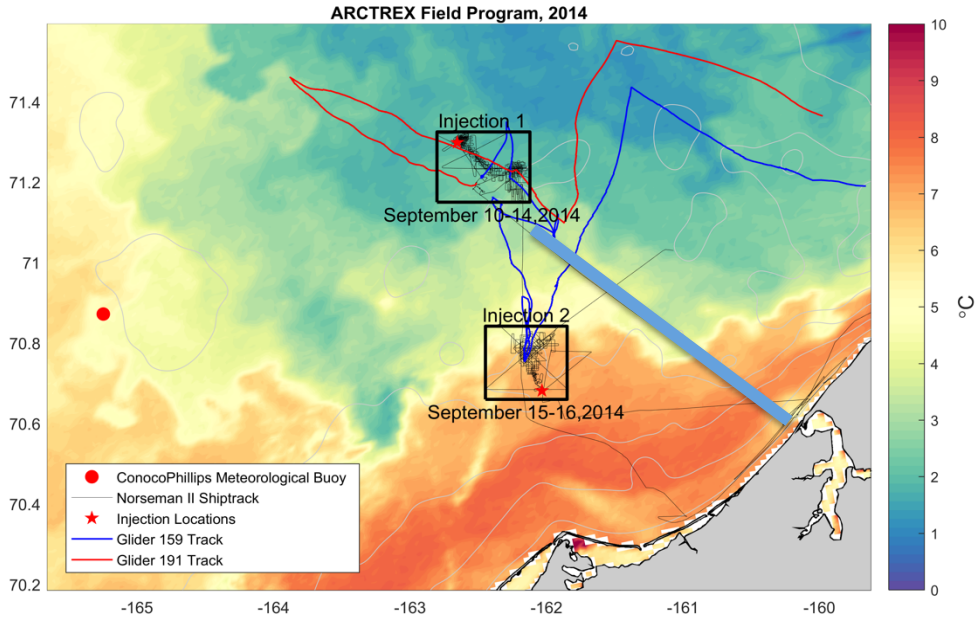

Figure 7. 2014 map of the ARCTREX study area, Northeastern Chukchi Sea. The two 2014 dye injection surveys described in this report are outlined by the black boxes. The ship track is shown in dark gray. The location of dye injections #1 and #2 are depicted by red stars and the location of the cross-shelf transect is in blue. The ConocoPhillips meteorological buoy, the location of our wind measurements, is the red dot located in the Klondike lease patch. Daily average SST from MODIS for September 15, 2014 is also shown. Isobaths are contoured at increments of 10 m depth.

Figure 8 shows cross sections of salinity, temperature, and density from the cross-shelf survey depicted in Figure 7. Far offshore, the stratification on the shelf can be characterized as a two-layer system with cold fresher waters (MW) overlaying very cold salty waters (WW). On the innermost section of the transect is the Alaska Coastal Current, which transports warm, fresh ACW along the Alaska coast. Between these environments, the water column of the shelf includes an intermediate layer of water that is warm and moderately salty. At the surface, the cross-shelf structure of density is characterized by light waters offshore with densities less than 1023 kg m^{-3}. Inshore of this are more dense waters exceeding 1024 kg m^{-3}. The intersections of the isopycnals with the surface are the signature of the fronts common in the Chukchi Sea. Density is controlled by salinity, so temperature can be used as a tracer for the intrapycnocline intrusions seen offshore of the front. It is likely that the intermediate layer of warm water has moved northward from a front in a manner similar to that observed by Lu et al. (2015). In fact, the subduction of warm saline shelf waters underneath fresher offshore melt waters was observed during dye injection #2 as will be discussed later.

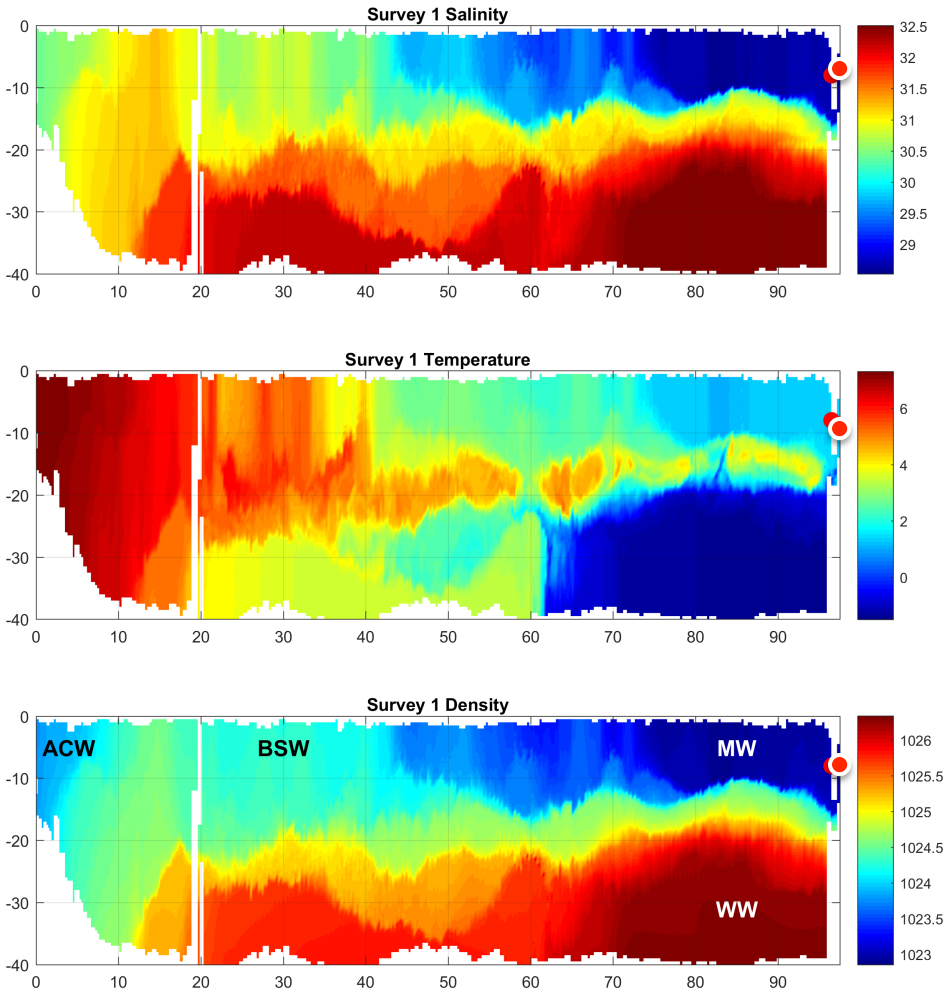

Figure 8. Cross-shelf vertical sections of water properties, September 10, 2014. Salinity (top), temperature (middle), and density (lower) collected by the Acrobat during the initial transect from Wainwright to the site of the first dye injection site. The x-axis scale is km offshore, and the red dot is the approximate location of dye injection #1.

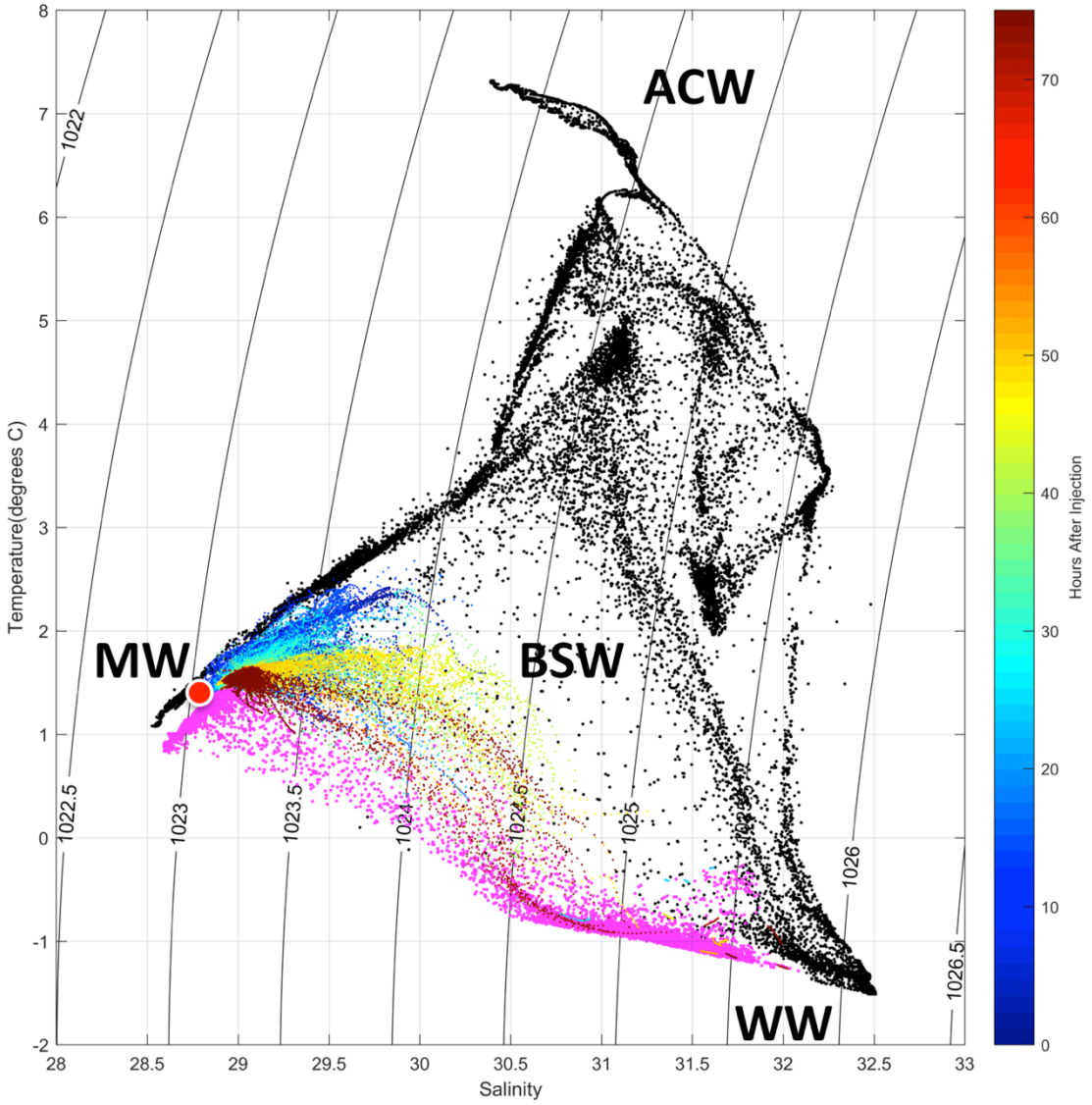

Figure 9. Temperature-salinity diagram for dye injection #1, September 2014. Points are T-S properties measured by the Acrobat outside (black) and inside (blue-to-red indicating hours after the dye injection) the dye patch and across the entire butterfly survey (pink). The red dot marks the T-S of dye injection #1.

The salinity of the offshore upper layer MW is ~29 psu and temperature is < 2°C, and it overlies dense WW with salinities exceeding 32 psu and temperatures < 0°C. Surface to bottom density difference exceeds 3 kg m^{-3}. The temperature-salinity diagram in Figure 9 illustrates these water mass properties using data collected before and during the first dye injection, and Figure 10 does the same for the second dye release. Both the WW and MW have distinct T-S properties with origins at 32.5 psu and –1.5°C and 28.5 psu and 1°C, respectively. The mid-shelf waters have a more complex T-S structure with what appears to be several water masses including ACW at the highest temperatures and BSW at intermediate temperatures; this is all typical for the Chukchi Shelf. Note that prior to dye

injection #1, there is little mixing between the MW and WW; instead, mixing occurs between each of these water masses and the intermediate layer that sits at mid-depths between them. This changes over the course of dye injection #1 as the volume of the intermediate layer decreases, and mixing occurs more and more directly between the upper (MW) and lower (WW) layers. Dye injection #2 begins in BSW, but mixes with all available water masses.

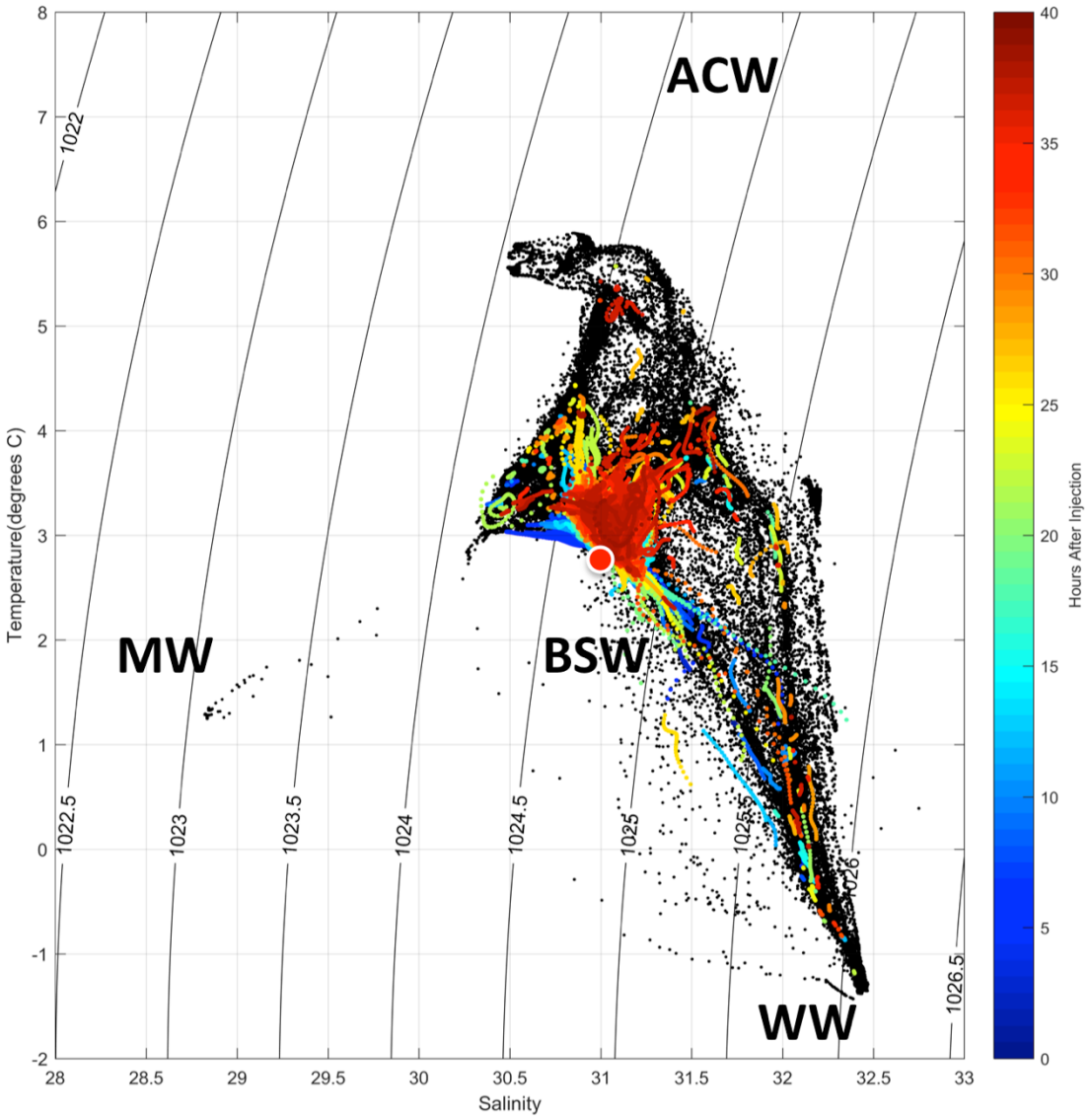

Figure 10. Temperature-salinity diagram for dye injection #2, September 2014. Points are T-S properties measured by the Acrobat outside (black) and inside (blue-to-red indicating hours after the dye injection) the dye patch. The red dot marks the T-S of dye injection #2.

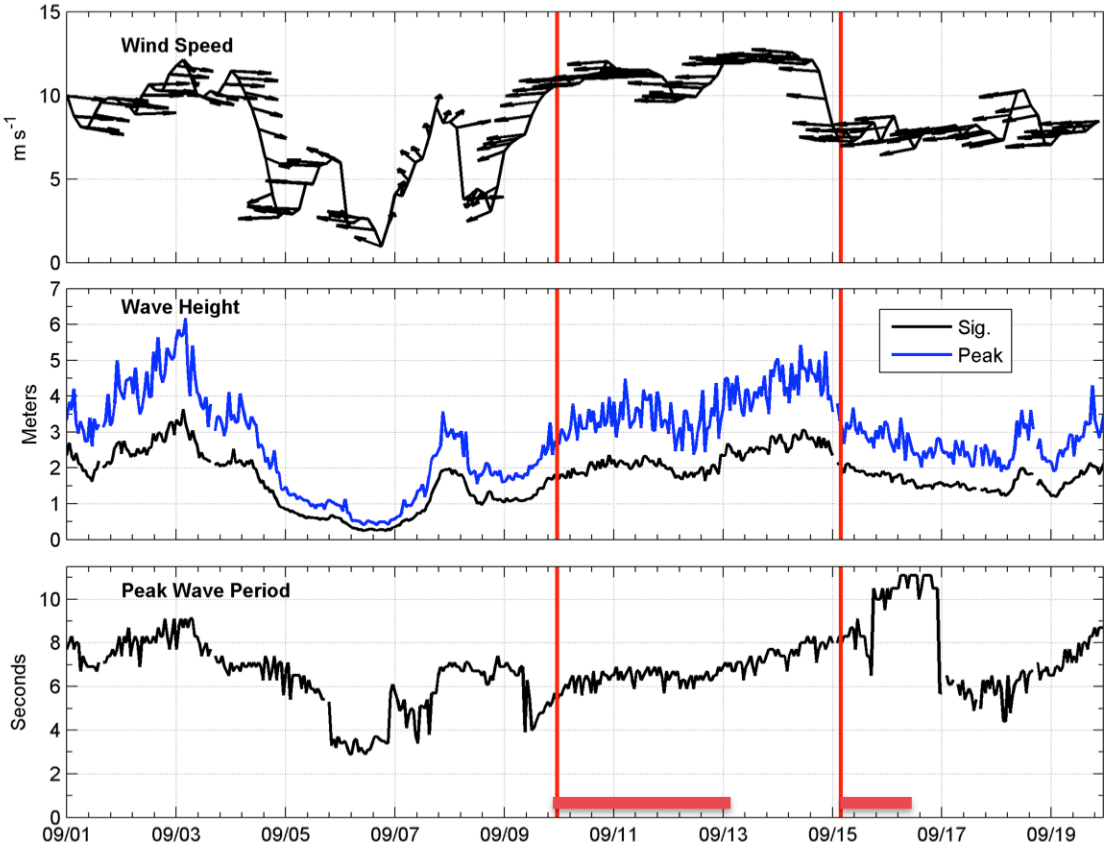

Figure 11. Environmental conditions from the Klondike ConocoPhillips meteorological buoy, September 2014. Wind vectors are presented along a time series of wind speed magnitude (top panel) with significant (black) and peak (blue) wave height (middle panel) and peak wave period (bottom panel). Red vertical lines depict the 2014 dye injections and the horizontal line indicates their duration. Arrow directions indicate the direction the wind is blowing toward.

As measured at the Klondike ConocoPhillips meteorological buoy, environmental conditions leading up to the 2014 ARCTREX experiment consisted of westerly (onshore) winds with speeds of 8–12 m s^{-1} from September 1–5 (Figure 11). A short lull in the wind on September 5 is associated with a change to easterly winds. From this period of very light winds on September 7, easterly wind speeds gradually ramped up to >10 m s^{-1} on September 9 and persisted with relatively constant intensity throughout the ARCTREX field experiment, eventually relaxing on September 15. Corresponding wave heights peaked on September 3 with significant wave heights reaching 3 m and peak wave heights near 6 m. During the dye injection #1, significant wave heights reached 1.5 m and peak wave heights were near 3 m. The conditions for field operations deteriorated slowly over the course of the experiment and during the second injection; significant wave heights reached 2.5 m with peak wave heights cresting over 4 m. Wave periods at Klondike steadily climbed from 5 to 7 seconds during the course of the two dye

injections. Note that the wind direction corresponds to an Ekman drift in the upper layer toward the west-northwest, which is relevant to the dye evolution discussed later.

The daily average surface currents from HFR for the days of dye injections in 2014 (Figure 12 and Figure 13) show that large areas of the shelf have coherent, alongshore flow fields, but that currents at dye release sites are onshore (September 10) or offshore (September 15). During this time period, the ACC is experiencing swings in direction, creating convergences and divergences offshore of Wainwright that result in the highly variable flow field there. Evidence of fronts exists where the currents abruptly change direction.

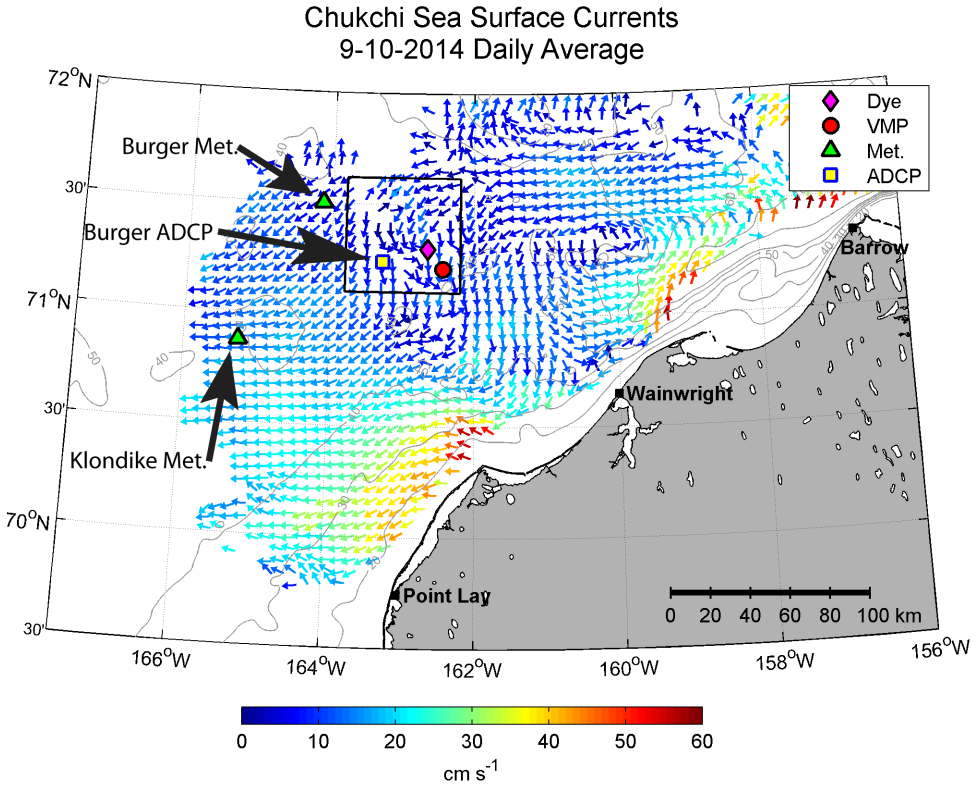

Figure 12. Daily average surface currents from HFR, September 10, 2014. The black box shows the location of the Burger lease patch, and the pink diamond shows the location of dye injection #1. Vector color indicates surface current speed.

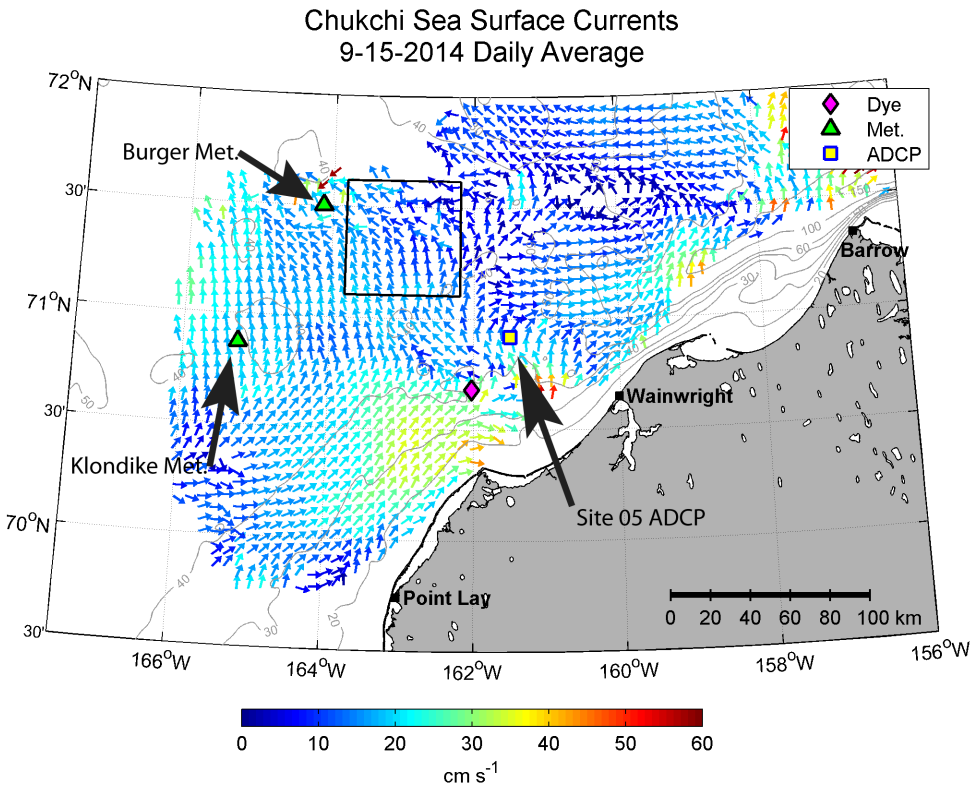

Figure 13. Daily average surface currents from HFR, September 15, 2014. The black box shows the location of the Burger lease patch, and the pink diamond shows the location of dye injection #2. Vector color indicates surface current speed.

The vertical structure of currents below these surface features can be estimated by examining the data from nearby moored ADCPs and meteorological buoys. These will not be exact versions of the currents during the dye releases, but will give a helpful estimation of vertical shear and variability in time. During the period of dye injection #1 (Figure 14), the surface currents at the Klondike meteorological buoy shows the influence of the large-scale alongshore flow noted in the HFR figure. However, the surface currents at the Burger ADCP mooring show strong but highly variable current with a prominent inertial signal. Currents in the surface layer there are vertically uniform down to at least 16 m, but the bottom layer exhibits steady onshore flow, meaning that there is strong vertical shear between the MW and WW layers. At Burger, conditions are consistent throughout the entire period of the first experiment, though given the spatial heterogeneity in this area, this may not be true at the dye injection site itself.

In contrast, the flow during the second dye injection is highly variable in time (Figure 15). A very strong north/northeastward current event at the nearby Site05 ADCP mooring ends abruptly immediately prior to the dye injection, and there are hints in the surface currents at Klondike and in the hourly HFR maps (not shown) that this adjustment has a wide scale. Below the surface, currents are variable; currents are occasionally in opposing

directions at different depths, and there is a short period of inertial motion at mid-water that is not evident at the surface or bottom.

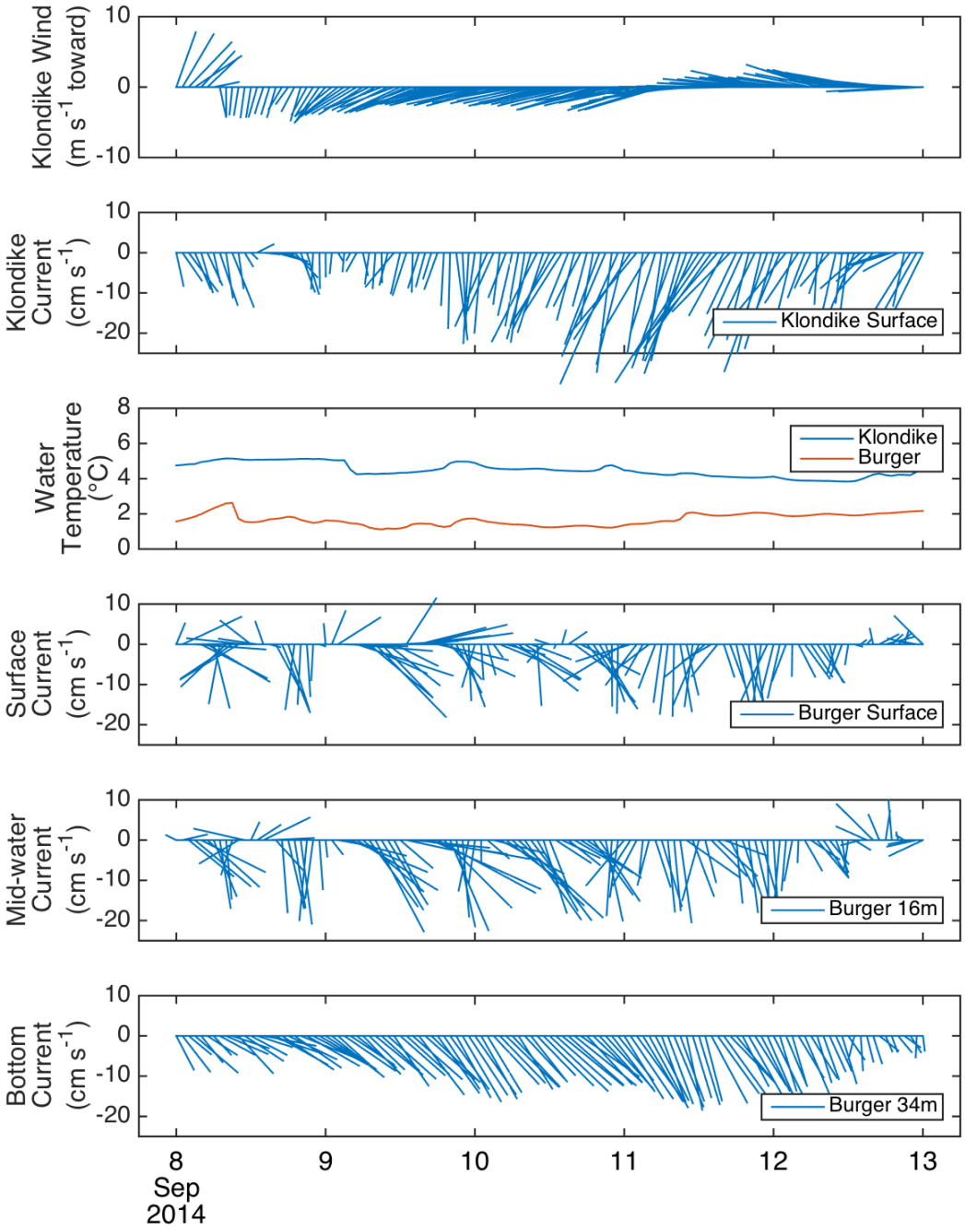

Figure 14. Meteorological buoy and ADCP mooring data, September 8–13, 2014. Winds and currents are in vicinity of dye injection #1, and vectors are oriented in the toward direction.

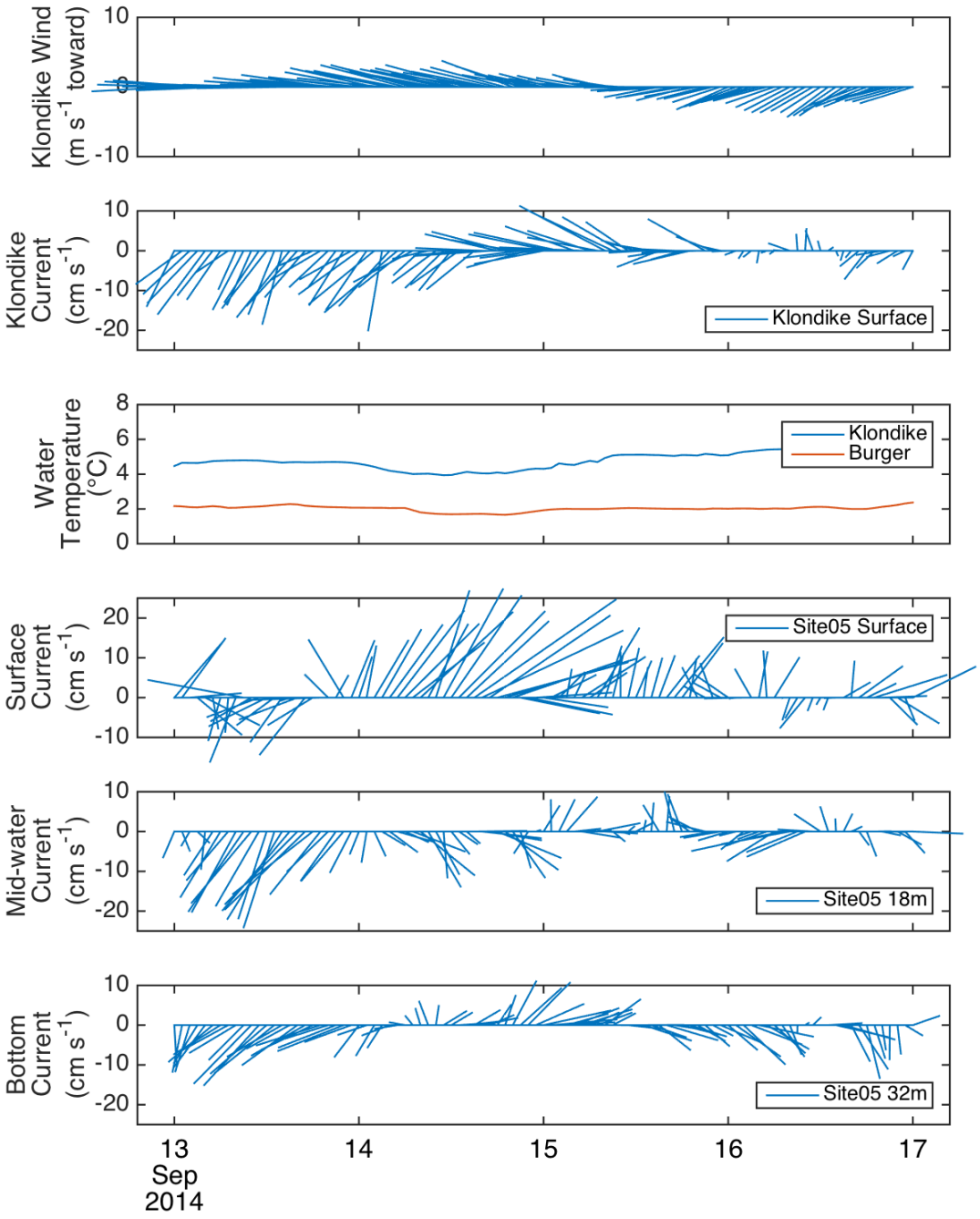

Figure 15. Meteorological buoy and ADCP mooring data, September 13–17, 2014. Winds and currents are in vicinity of dye injection #2, and vectors are oriented in the toward direction.

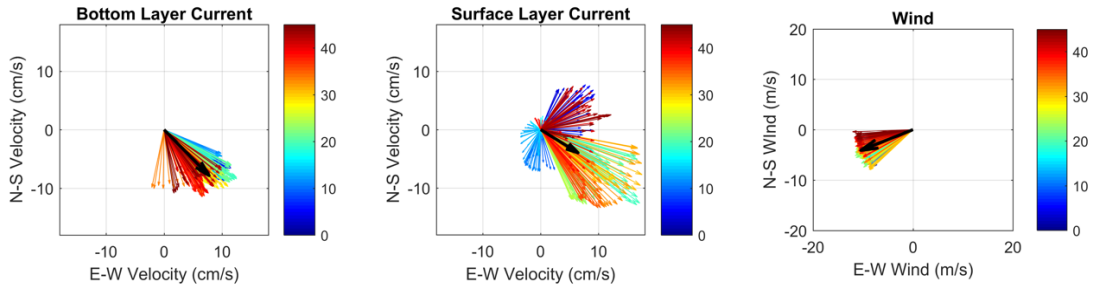

Figure 16. Currents from the shipboard ADCP, September 2014. Currents measured by shipboard ADCP in the bottom (left) and surface (middle) layers and winds measured at the Klondike buoy (right) are colored according to hours after dye injection #1. The black arrows in each figure are the mean value.

A view of currents that is more applicable to the dye releases themselves is given by an analysis of lower and upper layer currents from the shipboard ADCP during dye injection #1 (Figure 16). Like the mooring data, both surface and bottom currents have a mean shoreward direction to the south-southeast. Bottom currents are steadier than surface currents. Bottom currents have a mean flow of $u = 7.7$ cm s^{-1} and $v = -7.8$ cm s^{-1}. Surface currents have a similar mean direction but exhibit much more variability, and the mean flow in the surface layer ($u = 6.9$ cm s^{-1}, $v = -3.9$ cm s^{-1}) is weaker than in the bottom layer. The variability in the surface layer is primarily associated with the inertial period motion noted previously.

Currents during this period are in the opposite direction from that predicted by Ekman dynamics. It has been noted in previous studies (Woodgate et al. 2006; Weingartner et al. 2013) that currents in this area are primarily driven by a large-scale pressure gradient, and our dataset provides an opportunity to test this using momentum balance equations. The measured current and friction in the lower layer can be used to estimate the pressure gradient, and this pressure gradient is assumed to be the same in the surface layer. Therefore, a comparison can be made between the measured current in the surface layer and an estimate calculated from all the terms in the upper layer (pressure gradient, Coriolis, and wind stress) to test the validity of the model. If we neglect interfacial friction and advection, a steady momentum balance integrated over the lower layer can be written as:

$$-fv = -\frac{1}{\rho}\frac{\partial P}{\partial x} - \frac{\tau_b^x}{\rho H}$$

$$fu = -\frac{1}{\rho}\frac{\partial P}{\partial y} - \frac{\tau_b^y}{\rho H},$$

where u and v are the east/west and north/south velocity, P is pressure, and τ_b^x, τ_b^y, ρ, and H are the bottom friction in the E/W and N/S direction, density, and layer thickness respectively. Note that a steady momentum balance is not a bad assumption given the steadiness of the currents during dye injection #1 (Figure 14); no such assumption can be made during the other dye releases. Setting $H = 20$ m and using the mean bottom currents to estimate Coriolis and bottom drag with a quadratic drag law with a drag coefficient of 3×10^{-3}, we can solve for the pressure gradient (Figure 17), finding it is oriented in the along-shelf direction (northwest) and has a magnitude of 1.5×10^{-5} m s^{-2}.

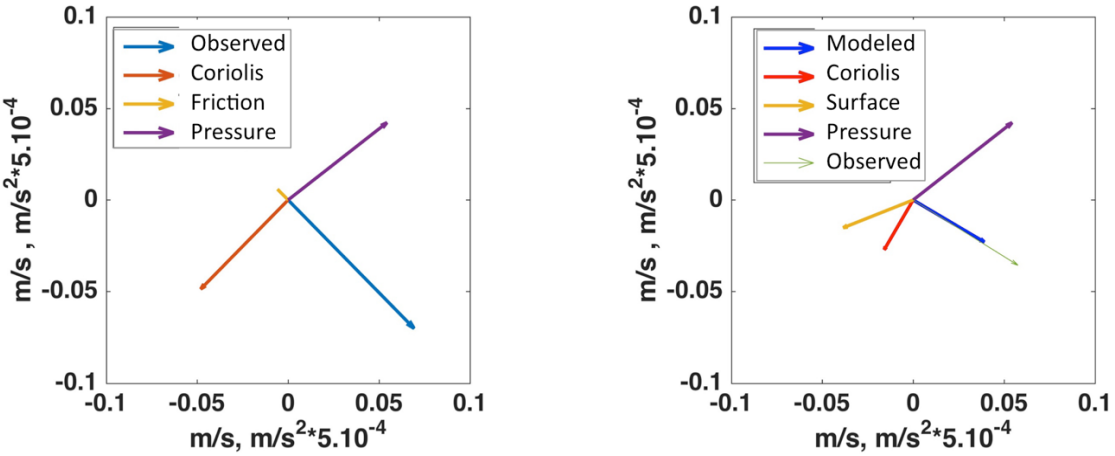

Figure 17. Results of a two-layer dynamical model. Terms in the momentum balance equations are plotted as vectors for the lower (left) and upper (right) layers of the water column.

Assuming the flow is barotropic, the pressure gradient can also be applied to the surface layer, whose set of equations becomes:

$$-fv = -\frac{1}{\rho}\frac{\partial P}{\partial x} + \frac{\tau_s^x}{\rho H}$$

$$fu = -\frac{1}{\rho}\frac{\partial P}{\partial y} + \frac{\tau_s^y}{\rho H},$$

where τ_{s_s} is the surface wind stress, which we estimate with winds from the Klondike meteorological buoy using a quadratic formulation with a drag coefficient of 1.2×10^{-3}. This simple model indicates that indeed the pressure gradient is larger than the wind stress, and thus the flow is primarily driven by the pressure gradient and resembles geostrophic flow— to the right of the pressure gradient—rather than Ekman. The estimated current (blue arrow) is slightly weaker than the observed current (thin green arrow), but qualitatively the magnitude and direction are quite similar.

4.2. 2015 Field Experiment

Figure 18 shows the study area for ARCTREX's 2015 observational effort. The ship track for the 2015 dye release surveys is shown in dark gray, and the 2015 dye injection described in this report is shown in the black box. Wind data during 2015 was obtained from the Klondike ConocoPhillips meteorological buoy, but there was no wave data collected this year and the inshore ADCP mooring, Site05, had been moved to another location. Also shown in the figure is the SST field from the MODIS satellite as an average over the time of the dye injection surveys. The warmer waters of the ACC can be seen in the southeast portion of the map, but the overall temperature gradient is lower because the very cold MW that was present in 2014 is absent in 2015, and the meanders and fronts are comparatively subtle. However, the study area for the injection does lie within a weak gradient in SST.

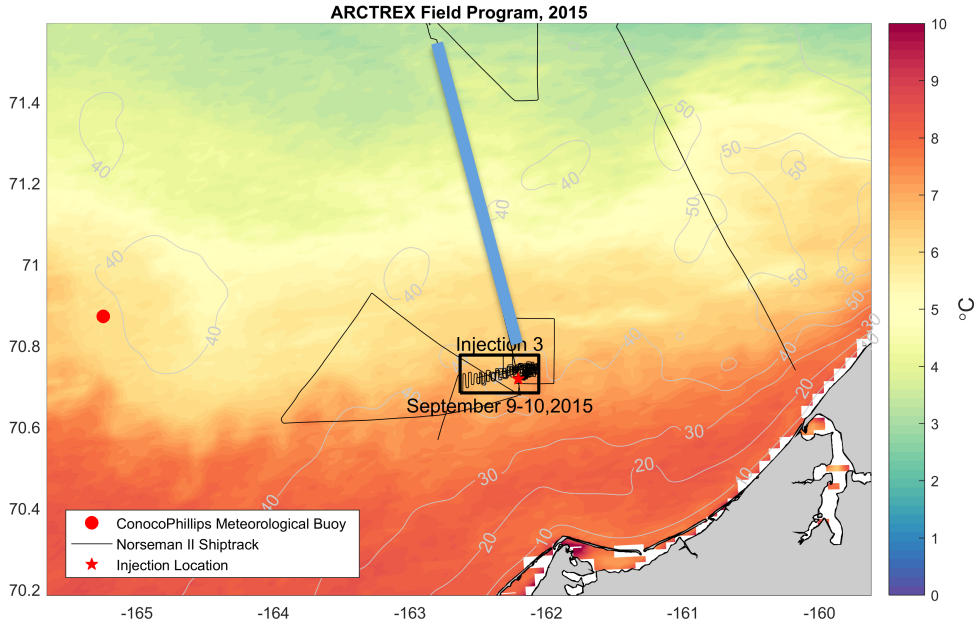

Figure 18. 2015 map of the ARCTREX study area, Northeastern Chukchi Sea. The 2015 dye injection surveys described in this report are outlined by the black box. The ship track is shown in dark gray. The location of dye injection #3 is depicted by a red star, and the location of the cross-shelf transect is in blue. The ConocoPhillips meteorological buoy, the location of our wind measurements, is the red dot located in the Klondike lease patch. Average SST from MODIS is also shown, shaded in °C. Isobaths are contoured at increments of 10 m depth.

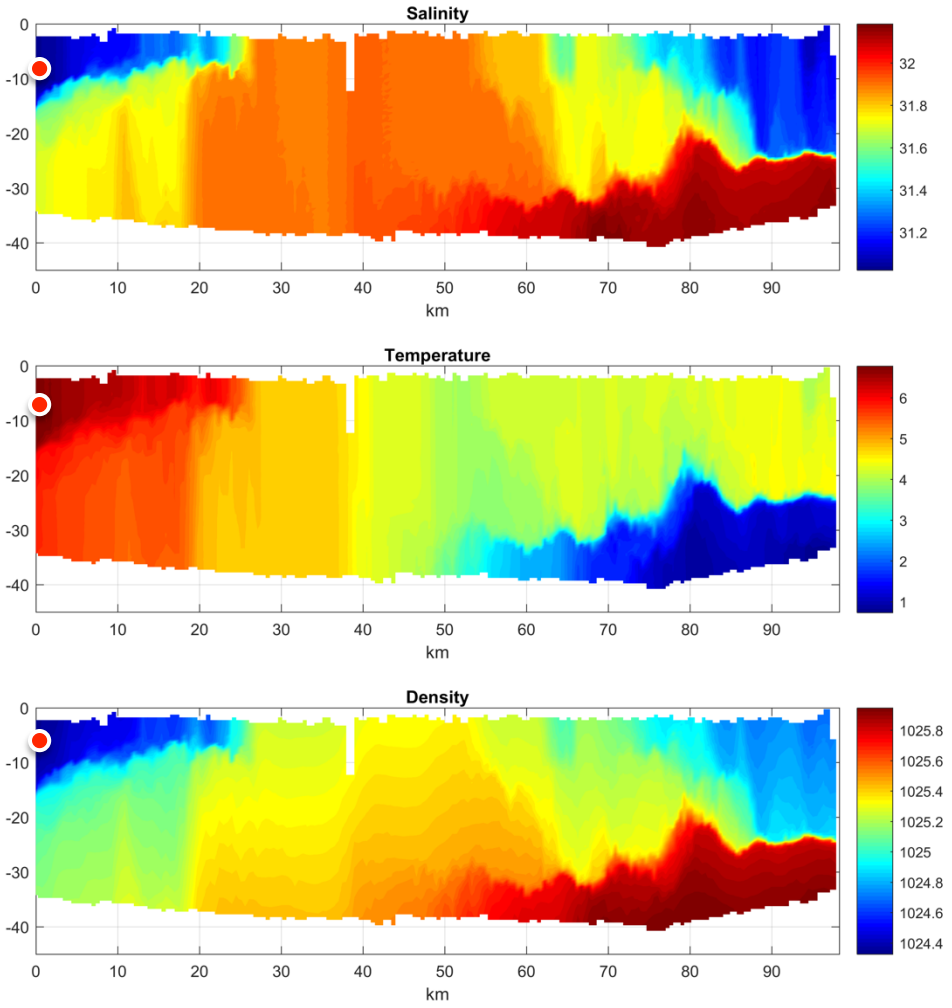

Figure 19. Cross-shelf vertical sections of water properties, September 2015. Salinity (top), temperature (middle), and density (lower) collected by the Acrobat during the transect from the northern site to the site of dye injection #3, which is marked with a red dot.

Figure 19 shows cross sections of salinity, temperature, and density from the cross-shelf survey offshore of dye injection #3 that is marked on Figure 18 above. Surface temperature ranges from 4–7°C. Inshore, the water is of similar temperature to water farther inshore in 2014, suggesting that ACW has extended farther across the shelf, whereas offshore, the water is >3°C warmer. At depth offshore, the water is also warmer than in 2014 and fresher, so that stratification is greatly reduced even offshore. The greatest portion of the shelf is occupied by vertically homogeneous water that is 4–5°C and ~32 psu, making it impossible to replicate the 2014 experiments in the two-layer, frontally complex environment found then.

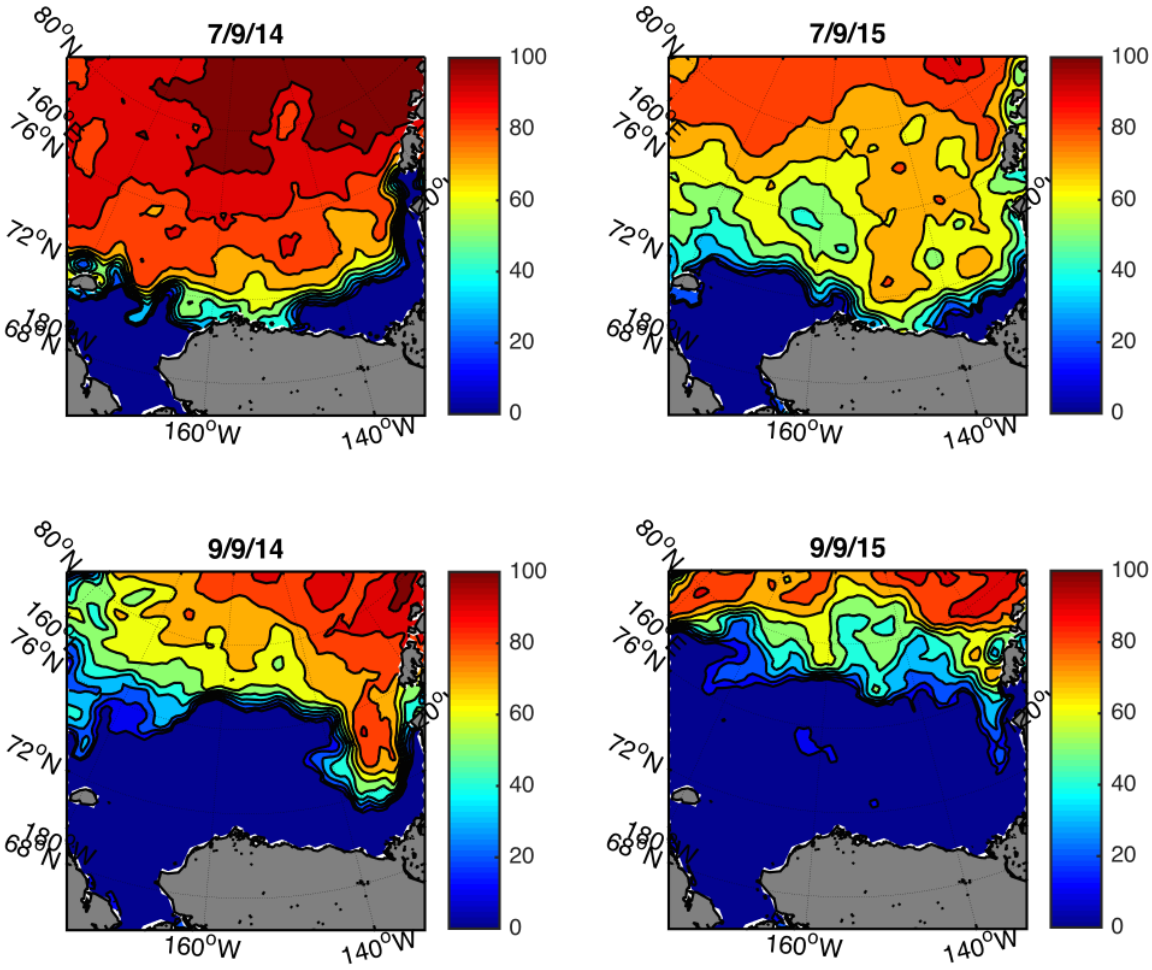

Figure 20. Sea ice concentration from special sensor microwave imager (SSMI), 2014 and 2015.

The absence of MW can be attributed to 2015's record low maximum sea ice extent. In February 2015, the maximum ice extent was the lowest in the satellite record, with below-average ice conditions everywhere except in the Labrador Sea and Davis Strait (http://nsidc.org/arcticseaicenews/2015/03/2015-maximum-lowest-on-record/). In the Chukchi Sea, this translated to earlier and farther ice retreat (Figure 20). In July 2014, portions of the Chukchi shelf had as much as 50% sea ice coverage, but by July 2015, the ice had completely retreated. In September, sea ice was far from the study area in both years, but the impact was still felt. Less sea ice formed means less WW, and less sea ice melted means less MW, leading to low stratification in 2015.

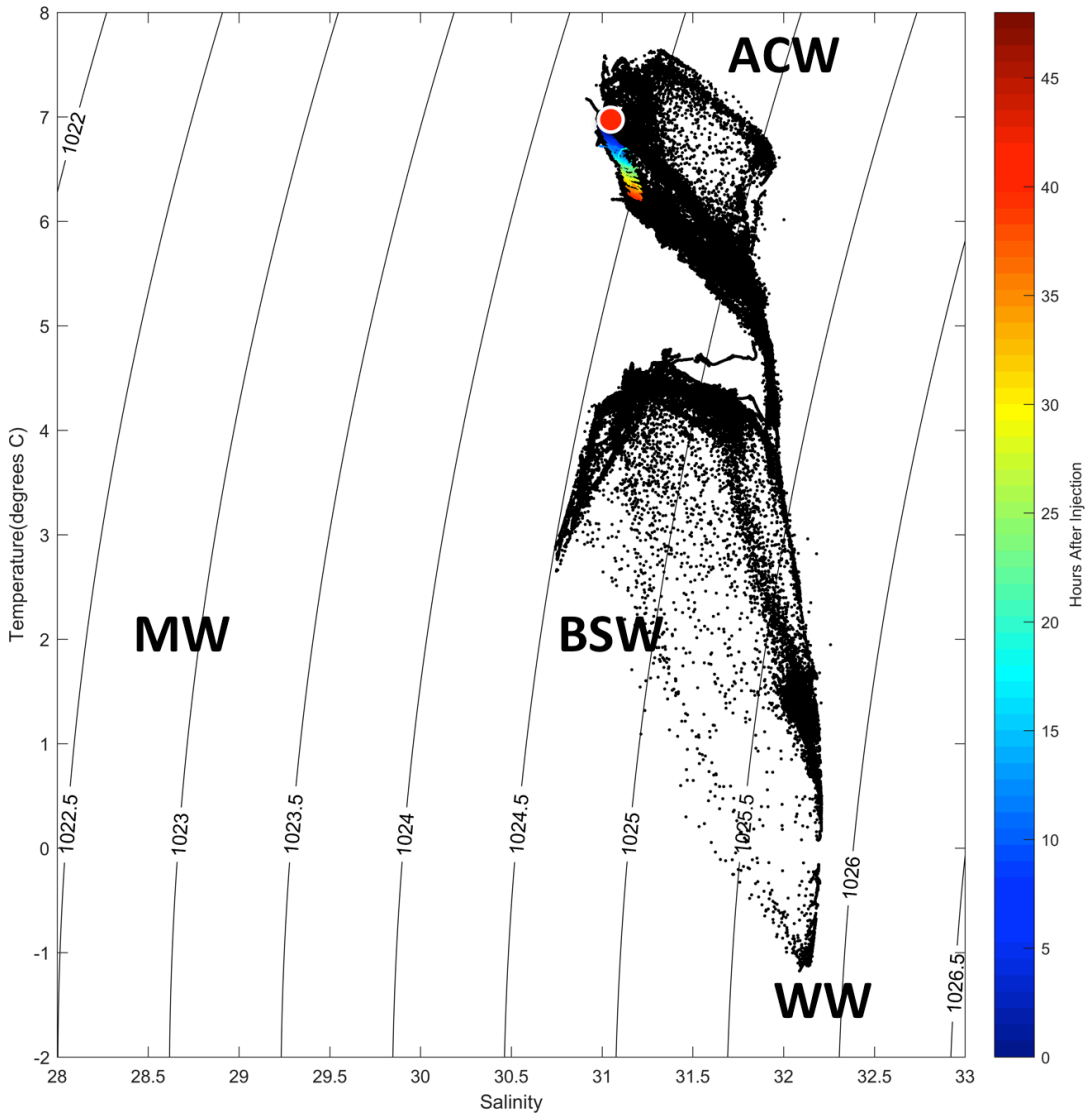

Figure 21 Temperature-salinity diagram for dye injection #3, September 2015. Points are T-S properties measured by the Acrobat outside (black) and inside (blue-to-red indicating hours after the dye injection) the dye patch. The red dot marks the T-S of dye injection #3.

The resulting differences in water masses are clearly evident in the 2015 T-S diagram (Figure 21), which depicts water mass properties from the cross-shelf section and during the dye release. Clearly, in 2015, the MW is absent. Dye injection #3 was performed in water whose properties were confined to 6–7°C temperature and 31–31.25 psu water, much warmer and saltier than in 2014 indistinguishable from the ACW as shown in Figure 21 above. The relatively small amount of WW encountered had end member properties of 32.2 psu and ~ –1°C, barely cold enough to quality as WW. Instead, the water of the dye injection was mixing only with slightly colder BSW at depth.

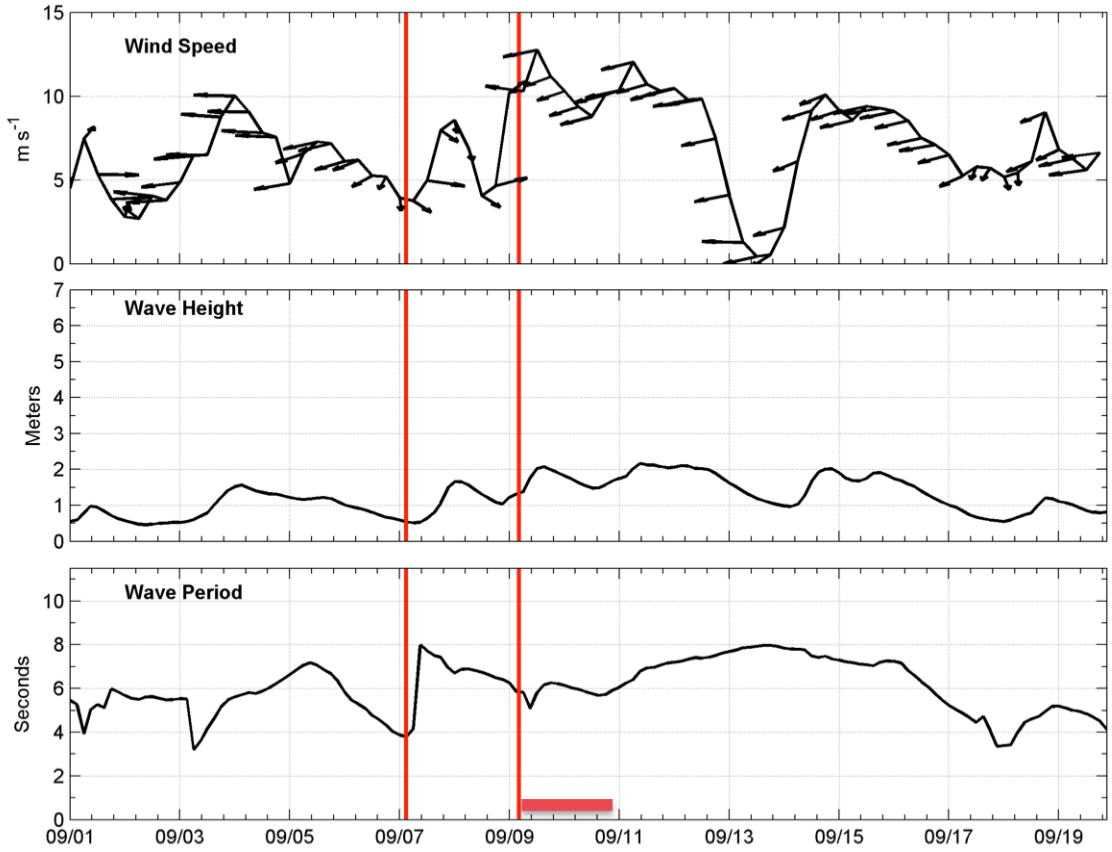

Figure 22. Environmental conditions extracted from NOAA's WaveWatchIII model, September 2015. Model output has been interpolated to the location of the Klondike ConocoPhillips meteorological buoy. Wind vectors are presented along a time series of wind speed magnitude (top panel) with significant wave height (middle panel) and peak wave period (bottom panel). Red vertical lines depict the 2015 dye injections and the horizontal line indicates their duration. Arrow directions indicate the direction the wind is blowing toward.

Wind and wave data during September 2015 are represented by output from the WW3 model (Figure 22). In contrast to 2014, the wind and wave conditions leading up to the first dye injection on September 7, 2015, were relatively calm. Winds were easterly with 5–7 m s^{-1} speeds, with the exception of a single, short-lived event on September 4, which reached speeds of 10 m s^{-1}. Leading up to ARCTREX, significant wave heights hovered around 1 m. Just after the deep-water injection on September 7, 2015, wind speeds increased rapidly, from 4 to 8 m s^{-1}, and associated wave heights increased from 0.5 to 1.75 m. After this first burst of wind, a second wind event occurred with wind speeds ramping up very rapidly from 4 to 14 m s^{-1} from the northeast; peak wind speeds were observed on September 9, the same day as the dye injection #3. Modeled wave heights increased from 1 to 2 meters during the second injection of 2015. Although sea states with greater than 2 m were safely operated in during the 2014 experiment, it was determined that the sea state after the rapid wind event on September 9 did not permit safe back-deck operations. We feel that this particular wind event was not accurately

described by the model output of WW3. Wind speeds remained at or above 10 m s^{-1} until midday on September 12, when they relaxed.

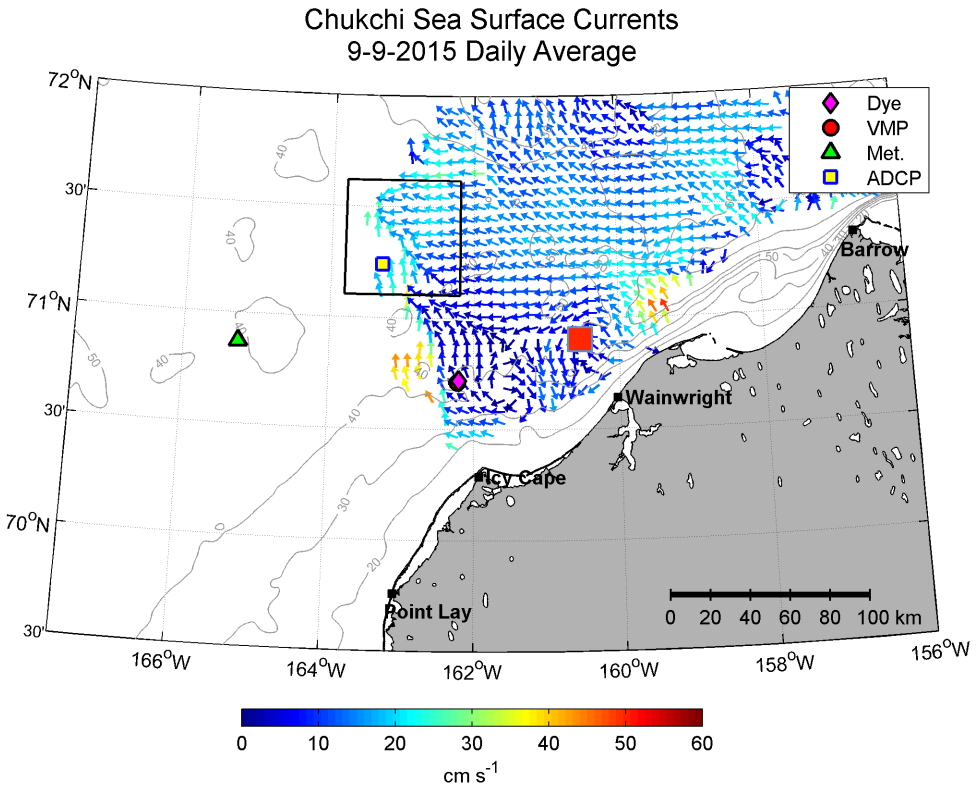

Figure 23. Daily average surface currents from HFR, September 9, 2015. The black box shows the location of the Burger lease patch, and the red square shows the location of dye injection #3. Vector color indicates surface current speed.

Figure 23 shows the daily average HFR field for the release on September 9, 2015. Note that the HFR station in Point Lay was moved to Icy Cape in 2015 in an attempt to fill the data gap in the convergence/divergence zone, moving the edge of the coverage closer to the dye injection site; also, data for this year have not been fully processed, so should be considered preliminary. However, it can be seen that once again, the dye injection occurred in an area of offshore flow, when other areas of the shelf have alongshore flow. It appears the ACC is weak, if not reversed, perhaps a consequence of the upwelling favorable winds that blew during the first half of September (Figure 22). By September 11, the ACC has fully reversed, and currents are toward the west or southwest over the entire HFR coverage area.

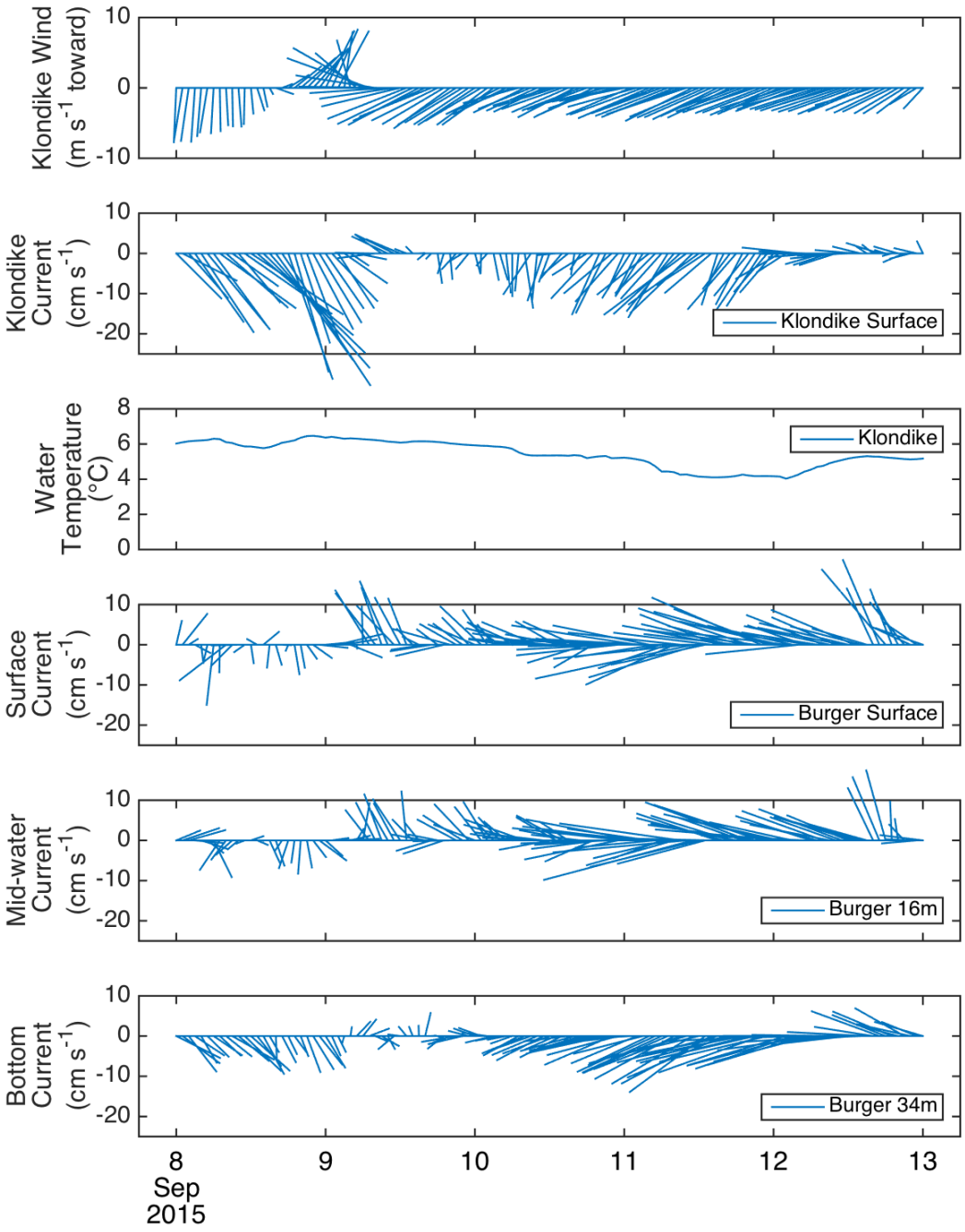

Figure 24. Meteorological buoy and ADCP mooring data, September 8–13, 2015. Winds and currents are in vicinity of dye injection #3, and vectors are oriented in the toward direction.

Mooring data is substantially reduced in 2015 due to the end of CSESP and the retreat of Shell from the Chukchi Sea. The Klondike meteorological buoy shows upwelling favorable winds prior to and after dye injection #3, while currents shift from southeast to southwest. There is no ADCP mooring near the 2015 ARCTREX survey site, but at the Burger ADCP mooring, currents are weak and variable before strengthening to nearly vertically homogeneous eastward flow. It is unlikely, though, that these currents accurately describe conditions farther inshore beyond showing that currents in early September 2015 respond dramatically to the strong and persistent southwestward wind—a condition different from the pressure gradient forced currents in 2014.

5. Dye Injection Results

5.1. 2014 Dye Injection #1

The dye study commenced with an injection of 50 kg of Rhodamine-WT dye into the surface mixed layer on September 10, 2014. The dye was tracked with shipboard surveys as the patch moved south/east throughout the 75-hour dye study. An Acrobat survey in a butterfly pattern measured wider-scale T-S properties toward the end of the first dye study (more detail in Figure 27). There is a long gap before the penultimate survey (#22) of dye injection #1 because we interrupted the dye survey to perform the survey of hydrography in the region.

5.1.1. Dye Patch Evolution and Advection

The majority of the analysis in this report focuses on dye injection #1 in 2014 because that dye release was tracked over 75 hours and provides the most detailed view of the evolution of a dye patch. Figure 25 below shows a sequence of dye patches, surface density, and drifter trajectories for the first dye experiment, where we made a total of 23 surveys of the dye patch. The red dots in Figure 25 depict the dye's centroid for each of the 23 patch surveys. The red arrows show the winds, which are from the east-northeast, while the blue arrow shows the mean current in the upper 10 m of the water column. For a select number of patches we also plot the dye's distribution along surface density field and the ship tracks that were used to map each patch. Both the drifters and the dye patch travel north somewhat before moving quickly to the southeast. The dye patch is then sharply strained along a density front for patches 11–13; we call this a "frontal straining event" in later discussion. It should be noted that a large portion of the dye patch was not included in the surveys after patch 16 due to the patch's extended tail.

In general, the movement of the dye is parallel to isopycnals, consistent with geostrophic flows, although there are numerous cases that deviate from this. During the first 8–9 surveys (the first 12 hours), the movement of the patch nearly completes a clockwise loop consistent with the inertial period motion seen in the current meter records. Between patches 10 and 14 there is a rapid movement of the dye to the south-southeast that coincides with sharper surface density gradients; this motion is consistent with geostrophy. During patches 15–21, the patch slows again as surface density gradients

weaken and its motion turns eastward. There was a gap between surveys of the patch because of the ~24 hour butterfly pattern survey, after which time the surveys of the last two patches (22 and 23) indicate an abrupt change of direction to the south. Over this entire trajectory, the mean density of the dye patch increased. However, between patches 16 and 17, we stopped sampling approximately 30% of the dye—the long tail of dye apparent in the western end of patch 16.

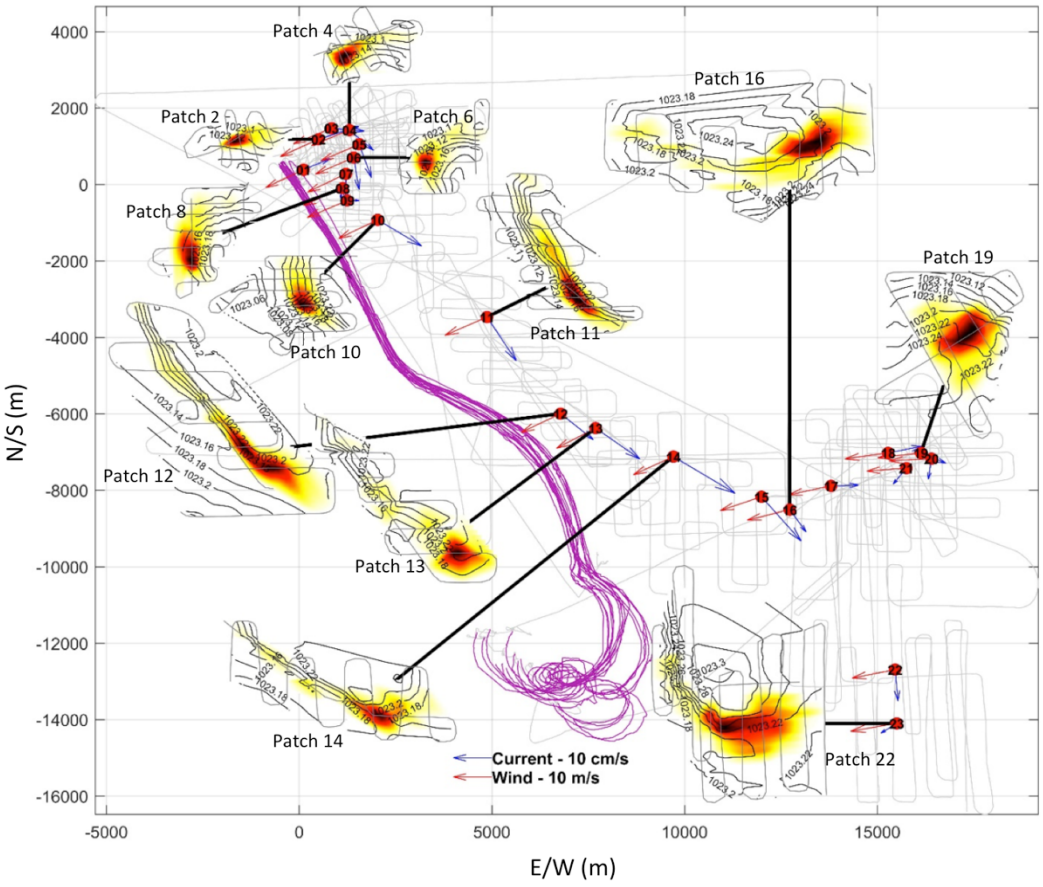

Figure 25. Mapped patches of dye for the first 75 hours after dye injection #1. The centers of mass of dye patches are shown by red dots. Shaded contours of dye concentration, contours of density, and the gray ship tracks of the sampling transects are offset from actual position but connected to them with heavy black lines and identified with the patch number. Tracks of drifters for same time period are shown in purple.

Drifters were initially deployed in the middle of the dye patch, and there is general agreement between the trajectories of the two. Initially, both dye and drifters went toward the south-southeast, though the dye seems to have experienced inertial motion whereas the drifter trajectories do not show it. However, between patches 15–21, the drifters went farther south than the dye patch, and this separation increased over time. Eventually the drifters slowed their southerly motion and followed a clockwise trajectory suggestive of inertial period motion themselves.

The general movement to the west by the drifters is consistent with the effects of wind on the drifters. It is likely that near-surface currents, which the 1 m drogued drifters follow, are more downwind than the mean currents in the mixed layer, which are more influential on the advection of the dye patch. Interestingly, the initial trajectory of the drifters, unlike the dye, shows no evidence of inertial motion; neither the wind nor shear in the mixed layer seems to explain this difference. It is also important to note that both the drifters and the dye moved in the opposite direction of the Ekman driven flows, which would be to the north-northwest. This suggests that the flows are driven by pressure gradients rather than winds. This conjecture is also consistent with the observation that the dye patch accelerated in the presence of elevated density gradients, with the momentum balances calculated earlier, and with established knowledge of the Chukchi Sea.

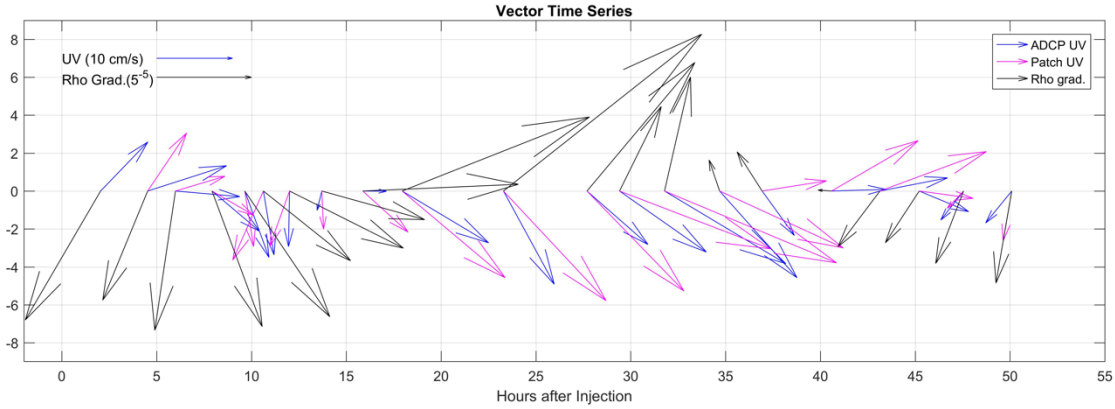

Figure 26. Currents and dye trajectory, dye injection #1. Vectors indicate the direction of mean density gradient (black), mean current in upper 10 m from shipboard survey (blue) and the mean speed and trajectory of the dye (purple) for patches 1–21. Patch trajectory is based on a centered difference estimate and thus is only estimated for patches 2–20.

To illustrate the relationship between the density gradient and advection more concisely, Figure 26 shows a timeline of the density gradient (black arrow), along with estimates of the advection based on the mean current in the upper 10 m from the shipboard ADCP (blue arrow) and the trajectory of the dye (purple arrow) for the first 20 patch surveys. The magnitude and direction of the density gradient is relatively constant for the first 4–5 patches during which time both velocity vectors rotate clockwise approximately 180 degrees. This is consistent with translation due to inertial motion. Thereafter, the density gradient rotates counterclockwise as the dye moves into an area of stronger density gradient; during this, the flow rapidly accelerates and is 90 degrees to the left of the density gradient, consistent with geostrophic flow in a surface front. Finally, the horizontal density gradient weakens and reverses, and currents weaken and become more westward.

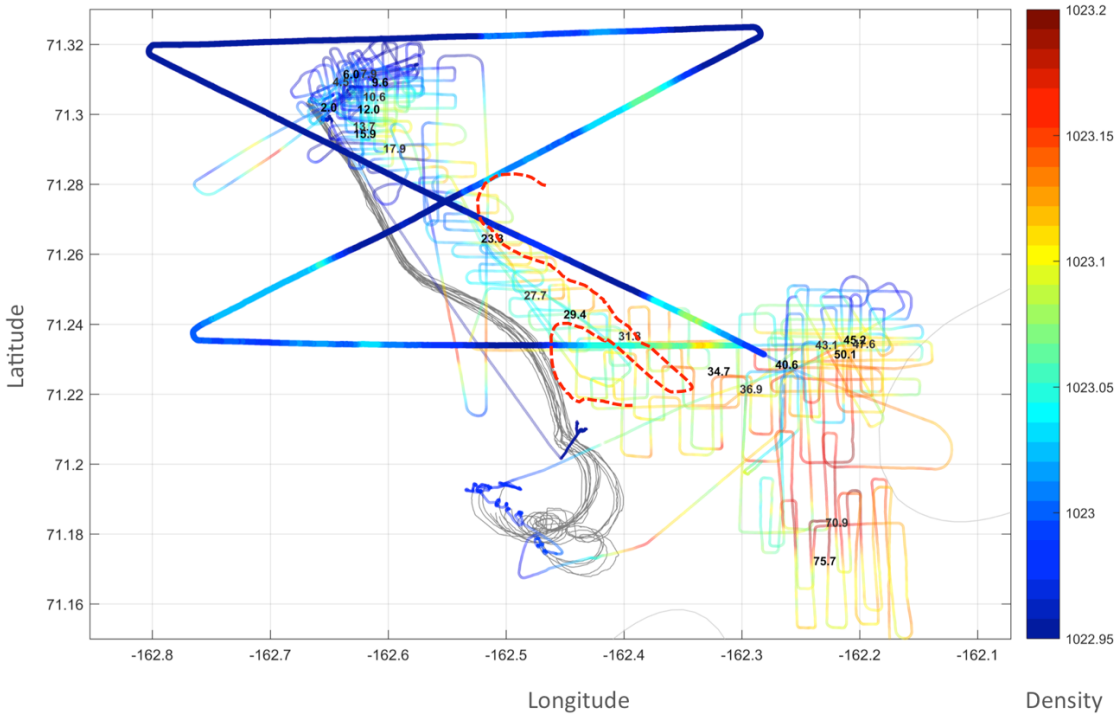

Figure 27. Surface density and drifter trajectories during dye injection #1. Surface density (color) is shown with drifter trajectories (black). The dotted red line depicts the shape of the frontal boundary inferred by surface density map. Numbers indicating hours after injection are positioned at the location of the dye patch centroid.

Figure 27 shows the surface density measured by the ship's TSG during the first dye experiment with the trajectories of the dye and the drifters. The large-scale structure of the density field is characterized by low-density water to the northwest and high-density waters to the south. Strong east/west density gradients are evident in the middle of the survey where the patch accelerated. However, the structure of this frontal system is complex, and in the vicinity of the dye's trajectory it appears to be associated with a lateral intrusion of MW into the warmer mid-shelf waters; the intrusion is 4–5 km long and 2 km wide and is indicated by the red-dotted line in the figure. The dye patch crossed this intrusion into the warmer and more saline fluid, then drifted to the east more slowly. It appears that in contrast, the drifters remained in the MW as evidenced by the densities measured when the drifters were retrieved. The dye patch's crossing of density surfaces is enabled by the fact that its density dynamically changes due to mixing processes, as will be discussed.

To relate conditions within the dye plume to those of the wider shelf, an earlier figure, Figure 9, shows the T-S properties from the cross-shelf survey, the evolving dye patch (blue to red indicating the time after injection), and the butterfly survey performed before the final two patch surveys. Initially, the dye patch appears to mix with BSW. While some of this is horizontal mixing due to the dye crossing the front into warmer water between hours 10–20, both the changing T-S properties of the dye and the crossing of

horizontal density gradients are likely primarily due to vertical mixing processes. The vertical cross-shelf sections (Figure 8) show that underlying the surface MW water mass is a subsurface intrusion of warm/salty BSW that is mixed into the surface layer from below. After hour 40, this intruded layer has been mixed away and now the mixed layer (and dye) begins incorporating WW from below. The mixing becomes increasingly diapycnal toward the end of the experiment. Data collected during the butterfly survey indicate only mixing between the upper-layer MW and the lower-layer WW. Note that this differs from the T-S properties that we observed in the larger-scale survey before dye injection #1, which indicates relatively little mixing between these water masses. We suggest that it is the strong and persistent winds during the dye experiment that generated mixing between winter and melt waters. In contrast, the weaker winds prior to the cross-shelf survey allowed the shelf water to intrude between the layers of WW and MW, creating a buffer that limited direct mixing between these water masses.

Figure 28–Figure 31 show vertical transects of dye concentration of selected patches. The transects were selected to be as parallel to the local density gradient as possible and still contain the maximum dye concentration. The horizontal coordinates were defined such that the origin of the x-axis is the maximum dye concentration. Patches 1–7 are similar; the surface layer is weakly stratified with a horizontal gradient of ~1 kg m^{-3} m^{-1}. Beneath the upper layer lies a 5–7 m thick layer of warmer BSW water that is associated with the intrusions seen in the vertical sections of physical properties (Figure 8). Below this layer is the cold salty WW. Over the first 7 patches, the maximum temperature of the intermediate layer varies from 2 to 2.5°C and its thickness varies from 3–6 m.

The evolution of the dye patch's temperature and salinity relative to the surrounding density field that was evident in the T-S diagram (Figure 9) can also be seen in Figure 28–Figure 31. Most notable is a continued increase in the dye's salinity and density, as the homogeneous water mass that the dye was injected into evolves through mixing with its surrounding waters. For example, in patch 1 the core of the dye has a salinity of 28.86 psu while by patch 7 the salinity has increased to 28.90 psu. These fields have been corrected for advection, but nevertheless, the dye moves relative to the background salt field by approximately 1 cm s^{-1} (see section 6.3). Between patches 8–12, the upper layer entrains the middle layer into the tracer patch at mid-depth which causes a permanent increase in the dye's salinity and a temporary increase in the dye's temperature. After patch 12, the intermediate layer has vanished and the temperature, salinity, and density of the upper layer have increased. Thereafter, the MW and WW mixed and the upper layer temperature have decreased while its density and salinity continue to increase. It is interesting to note that the horizontal density gradient in the upper layer has reduced significantly in the final patches.

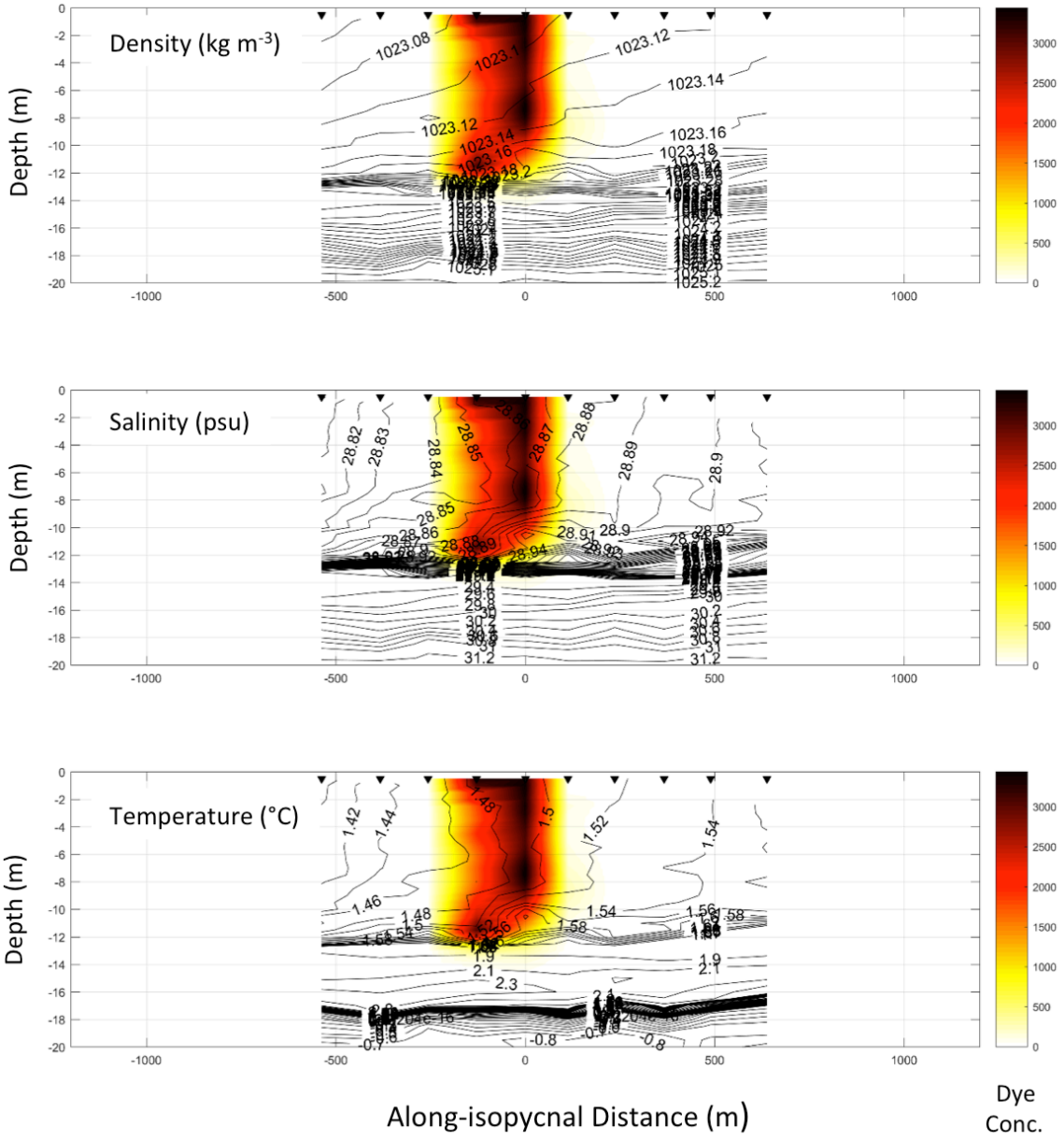

Figure 28. Vertical transects of dye concentration measured in patch 1 of dye injection #1. Dye concentration (color) is plotted with contours of density (top), salinity (middle), and temperature (bottom). The transects are parallel to the local density gradient. The horizontal coordinate system is such that the origin of the x-axis represents the maximum dye concentration.

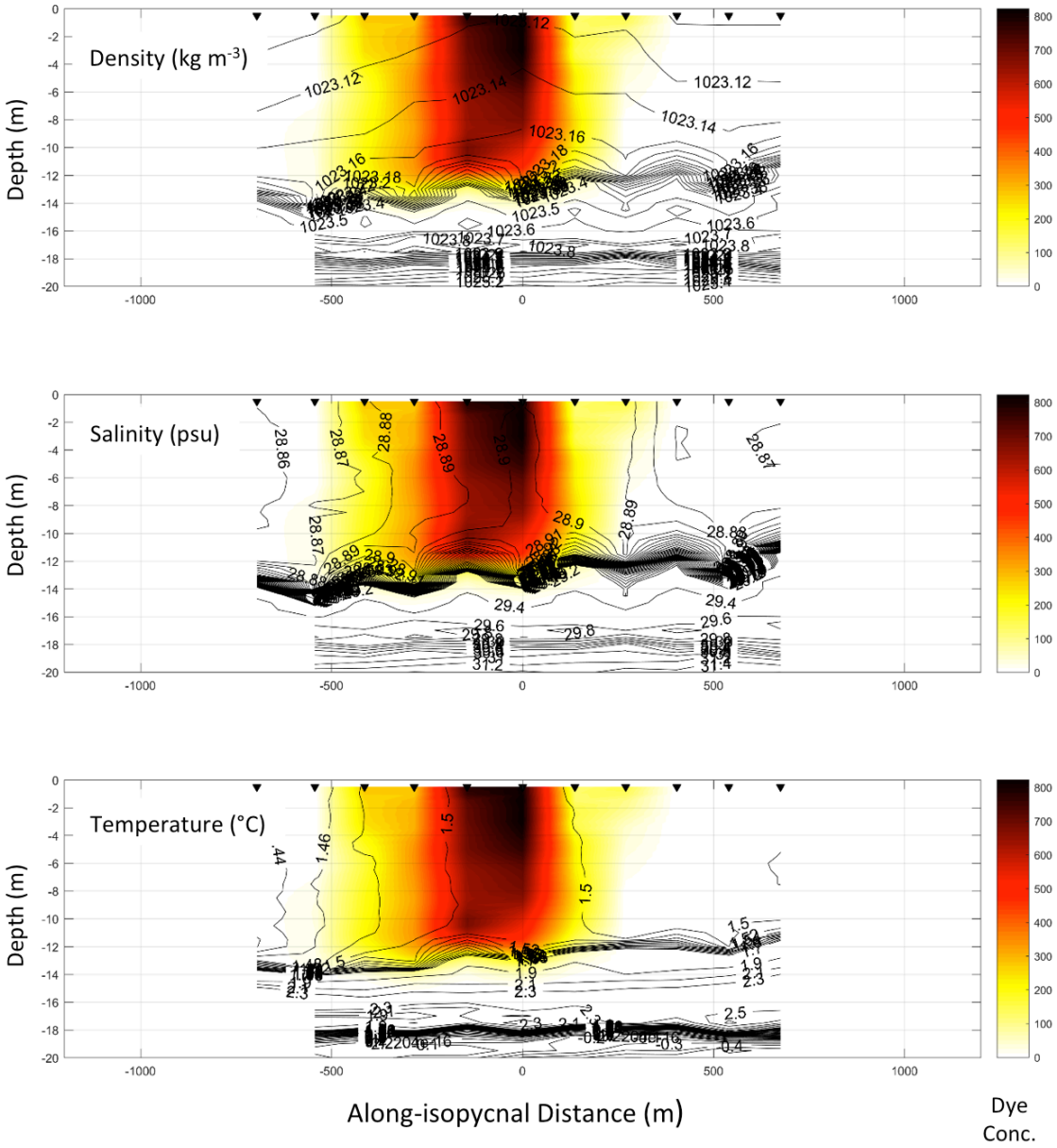

Figure 29. Vertical transects of dye concentration measured in patch 7 of dye injection #1. Plots as in Figure 28.

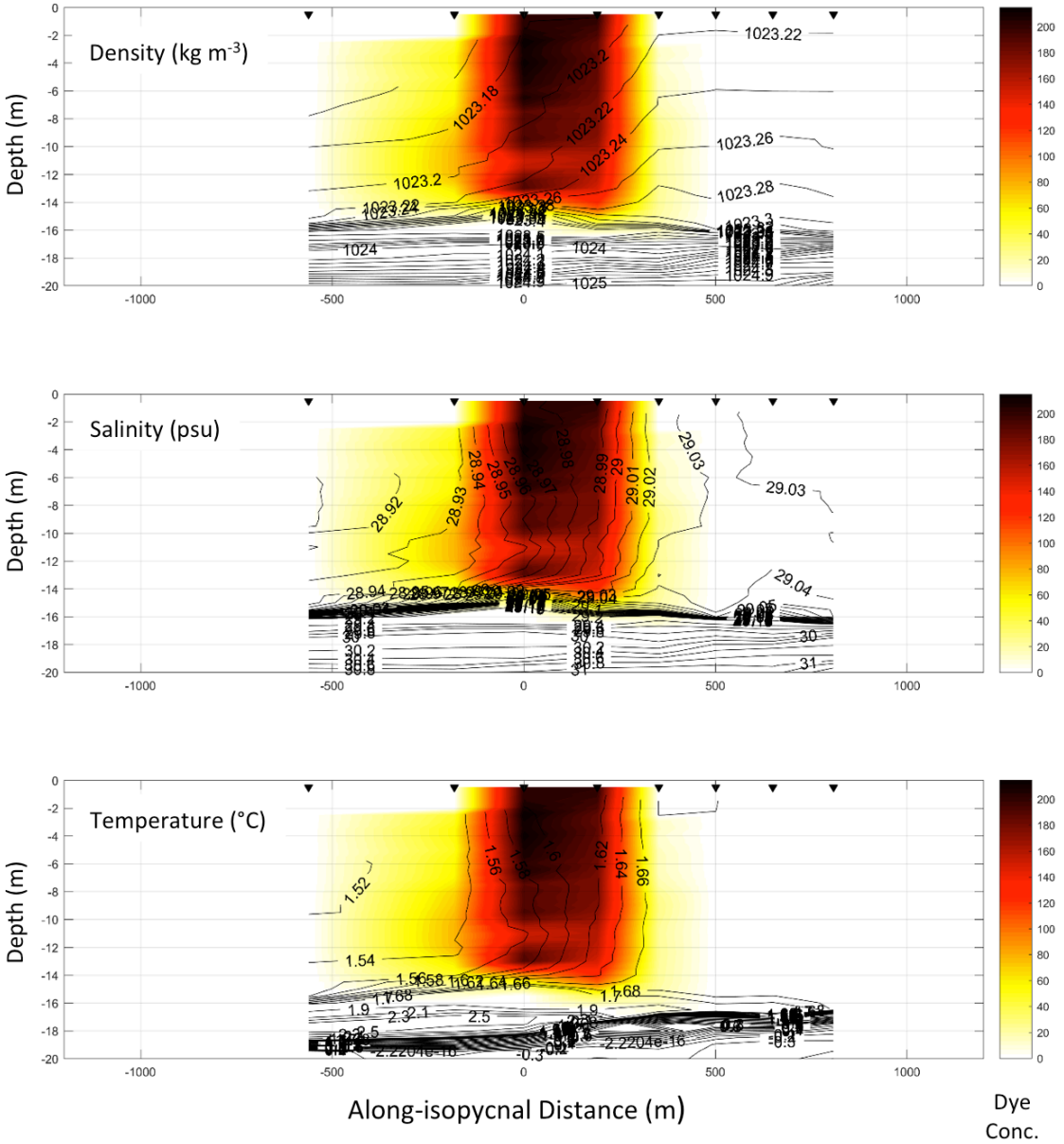

Figure 30. Vertical transects of dye concentration measured in patch 12 of dye injection #1. Plots as in Figure 28.

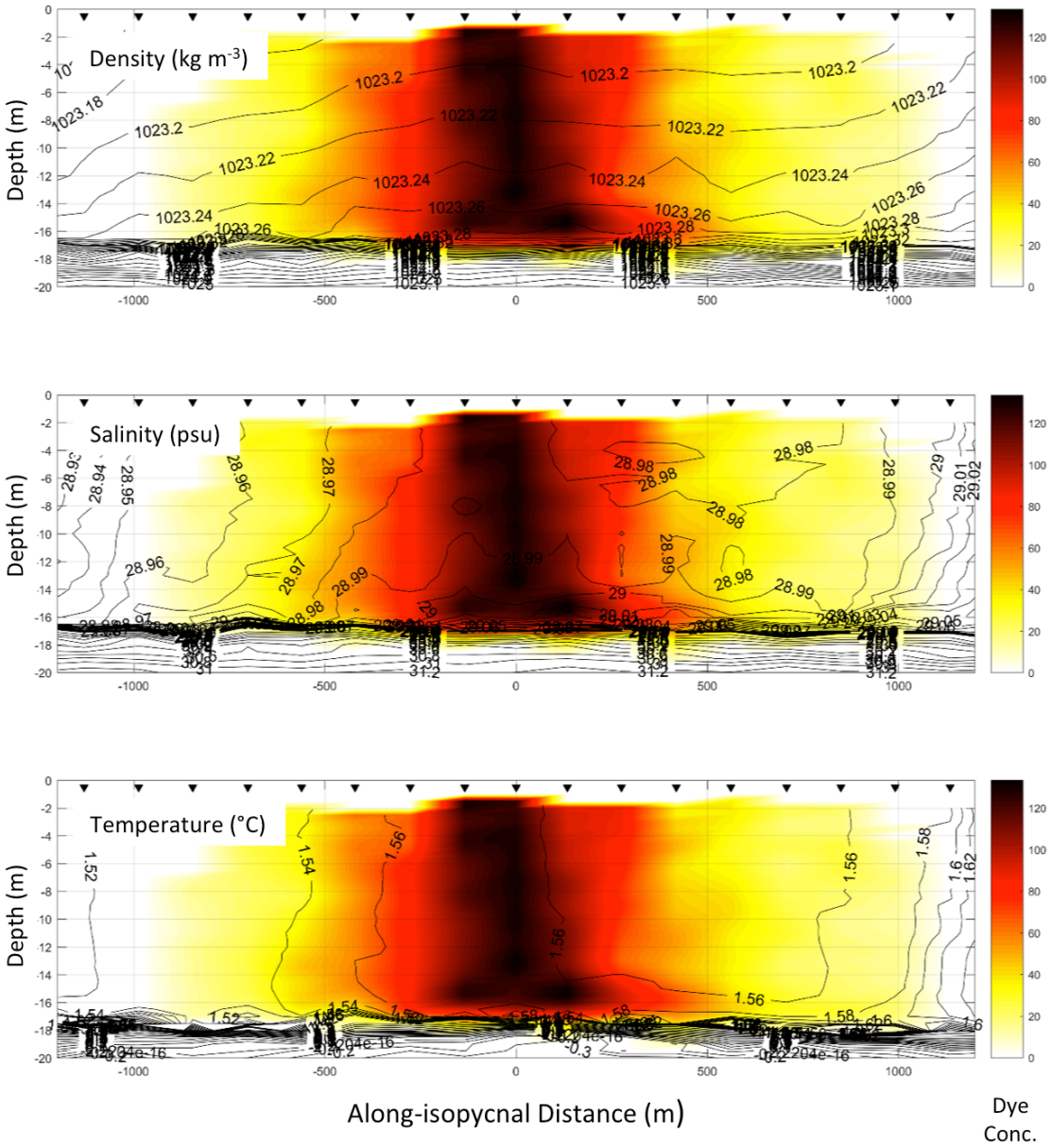

Figure 31. Vertical transects of dye concentration measured in patch 17 of dye injection #1. Plots as in Figure 28.

Changes in the physical properties of the dye patch can be summarized by plots of the mean temperature, salinity, and density over time (Figure 32). Density and salinity increase over time, consistent with the surface boundary layer mixing with denser water below. Temperature increases around the time of the frontal straining event, when the dye patch extended along a density front during patches 11–13. The temperature increases between patches 9–13 from 1.52°C to 1.6°C, and this increase occurred as the ~6 m thick layer of intermediate water of 2.2°C mixed into the 15 m thick upper layer of 1.52°C. Simple mixing of these two layers explains the observed increase in the dye's temperature. Thereafter, the water of the dye patch cools—though some of this variability

is due to the reduced area of dye sampled after patch 16.

Figure 32. Time series of mean patch temperature, salinity, and density of dye injection #1.

5.1.2. Vertical Dispersion

The evolution of the mean salinity of the dye patch, *S,* and its restriction to a clearly defined mixed layer provide an opportunity to produce a preliminary value for vertical eddy diffusivity, K_V. If we assume that *S* increases only due to vertical mixing, the mean salinity of the dye patch would increase at a rate of:

$$\frac{\partial S}{\partial t} = \frac{K_v}{H}\frac{\partial S}{\partial z}$$

Using observed values of $\frac{\partial S}{\partial t} = 8 \times 10^{-7}\ s^{-1}$, $\frac{\partial S}{\partial z} = 0.7\ m^{-1}$, and $H = 15$ m yields a vertical eddy diffusivity, K_v, at the base of the dye patch of $1.7 \times 10^{-5}\ m^2\ s^{-1}$.

An alternative measurement of vertical dispersion comes from the VMP instrument that was deployed at one station consisting of five full-depth profiles to approximately 35 m, beginning 9/9/2014 20:33 UTC. (Table 2). This station was occupied approximately 4 hours prior to beginning the first injection, 13 km to the southwest of the injection site. During this first cast, fall rate and ship handling logistics were being coordinated, and so reliable estimates of ε were returned consistently over a depth interval of 7–30 m (Figure 33).

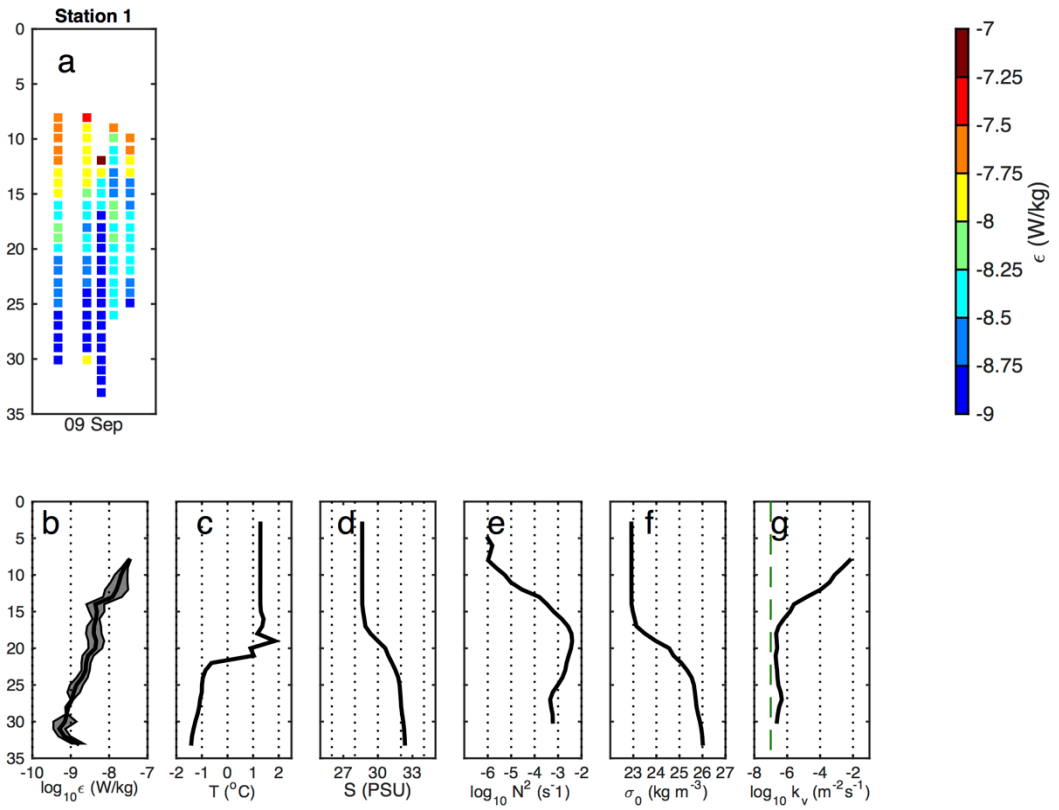

Figure 33. Summary of 2014 VMP station 1 data. The upper panel shows the vertical structure of dissipation over time. Lower panels show mean vertical profiles (from left to right) of dissipation, temperature, salinity, N^2, density, and diffusivity. The green dashed line in panel g represents background molecular levels of diffusivity.

VMP data show a two-layer system with enhanced turbulence levels in a 15–20 m thick turbulent surface mixed layer. At the base of the mixed layer, K_v measured by the VMP compares favorably with that computed from dye concentration gradients. In contrast, the bottom layer, from 20–30 m, had low levels of turbulence with almost no enhancement above background molecular levels, and no indication of a bottom boundary layer (BBL). It is likely that the BBL was not detected because the VMP was not able to get close enough to the bottom, but that one exists in a thin layer within a meter or so of the bottom. It should be noted that the turbulence and mixing levels were well within the resolvable range of the instrument, but were smaller in the bottom layer than what is typically found on continental shelves. In contrast to the tidally dominated Irish Sea (Simpson et al.1996), surface forcing dominates the weak tidal forcing of the Chukchi Shelf.

5.1.3. Horizontal Dispersion

Figure 34 shows the time rate of change of the dye's second moment ($\boldsymbol{D}^2$), from which a horizontal dispersion coefficient, K_H, can be estimated,

$$K_H = \frac{1}{2}\frac{\partial D^2}{\partial t}, \qquad (1)$$

Results indicate that horizontal dispersion is 2–3 $m^2\ s^{-1}$ in the first and last third of the experiment but increases an order of magnitude to ~25 $m^2\ s^{-1}$ in the middle third of the experiment. This increase occurred during the time that the dye became incorporated in the strongest horizontal density gradients and had the highest advective speeds; that is, the frontal straining event. The sharp decrease at around 43 hours is due to the reduced sampling of the dye patch after patch 16.

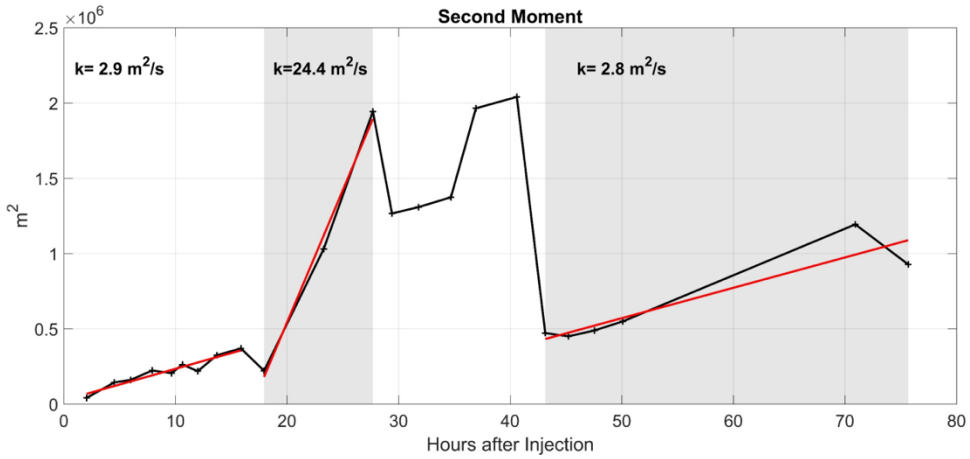

Figure 34. Second moment of the dye patches of dye injection #1.

Drifter statistics were calculated for a cluster that began when all the drifters were in the water (~1 hour after the dye) and ended the first time a drifter stopped transmitting. Plots of drifter statistics (Figure 35) show that, in contrast to the trajectories in isolation, the mean velocity of the drifter cluster shows a pronounced inertial signal like that seen in the surface current meter record (Figure 14) and velocity measured via the dye patch and shipboard ADCP (Figure 26). SST varies by a greater amount than does the mean temperature of the mixed layer as measured in the dye patch (Figure 32), but both increase during the first day and decrease in the second, as warmer then colder water is mixed from below. The second moment of the drifter cluster can be calculated via pairwise comparisons, and compares very well with that from the dye patch, despite their different trajectories. The horizontal eddy diffusivity, K_H, calculated via (1) was approximately zero the first day, then ramped up to ~15 $m^2\ s^{-1}$ by the end of the second day.

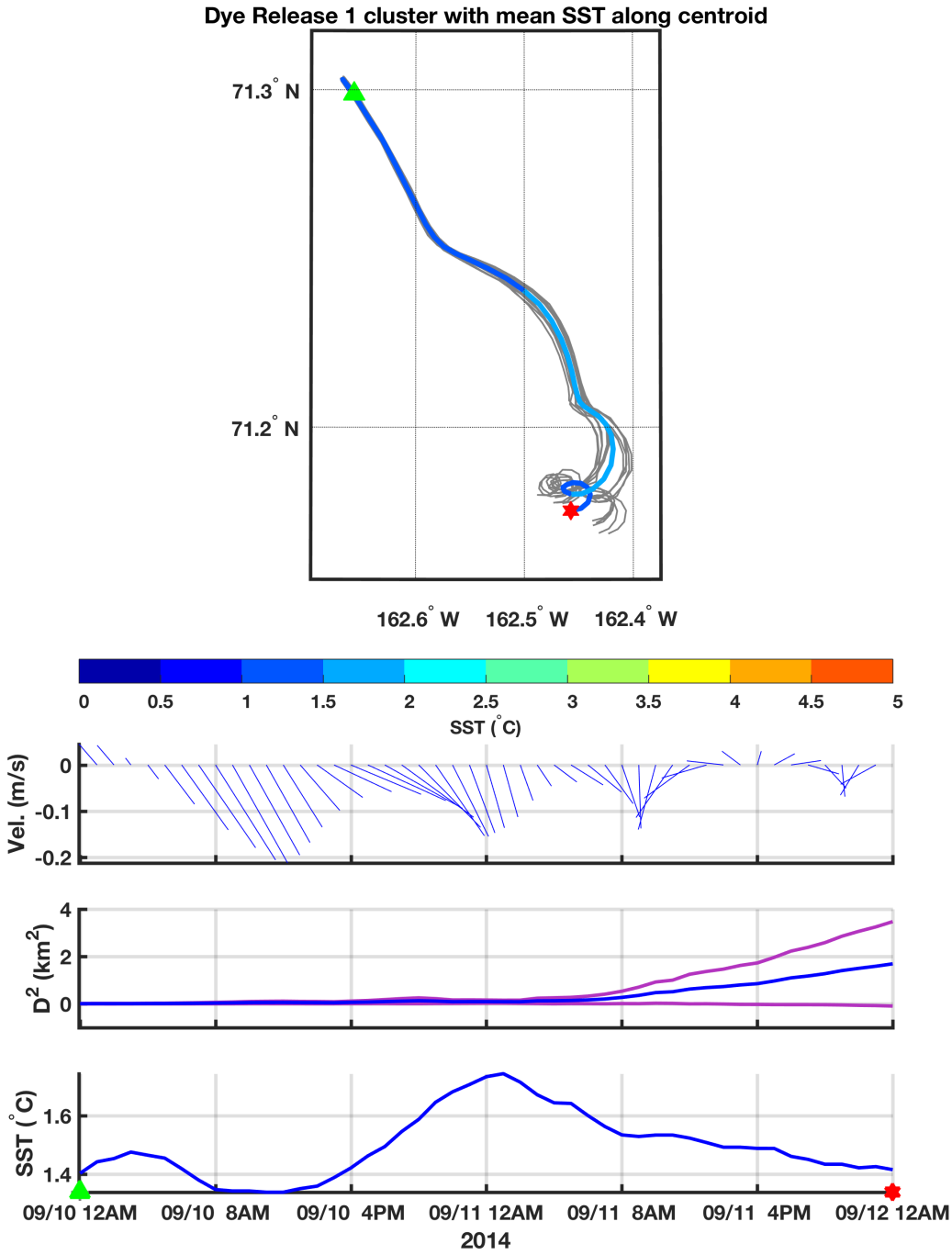

Figure 35. Drifters released during dye injection #1, September 10–11, 2014. The top panel contains the trajectories of each drifter in the cluster (gray) and the mean SST measured by the drifters plotted along the positions of the center of mass (color). Below are time series of the velocity of the center of mass, the second moment (i.e., spreading) of the drifter cluster (blue) +/– one standard deviation (purple), and the mean SST measured by the drifters.

5.2. 2014 Dye Injection #2

5.2.1. Dye Patch Evolution and Advection

During dye injection #1, the dye patch remained coherent and sampling could continue for several days. With a short amount of cruise time remaining, we decided to try sampling in a more dynamically active region where the dye would disperse more quickly. A location at a frontal boundary between offshore MW and northward flowing BSW mid-shelf water was chosen for dye injection #2. Prior to the dye release, the R/V *Norseman II* steamed south, crossing the front at approximately 162°W, 70.7°N; dye was injected inshore of the front in weakly stratified water. The dye injection system pumped ~45 kg of Rhodamine-WT fluorescent dye into the surface layer at ~10 m depth while the ship was allowed to drift. The injection took about ~20 min. After the injection, the dye was surveyed over the course of ~1 day with 11 synoptic realizations of the dye (patches) measured. Over the course of the experiment, winds were generally to the west or southwest at 7–8 m s^{-1}.

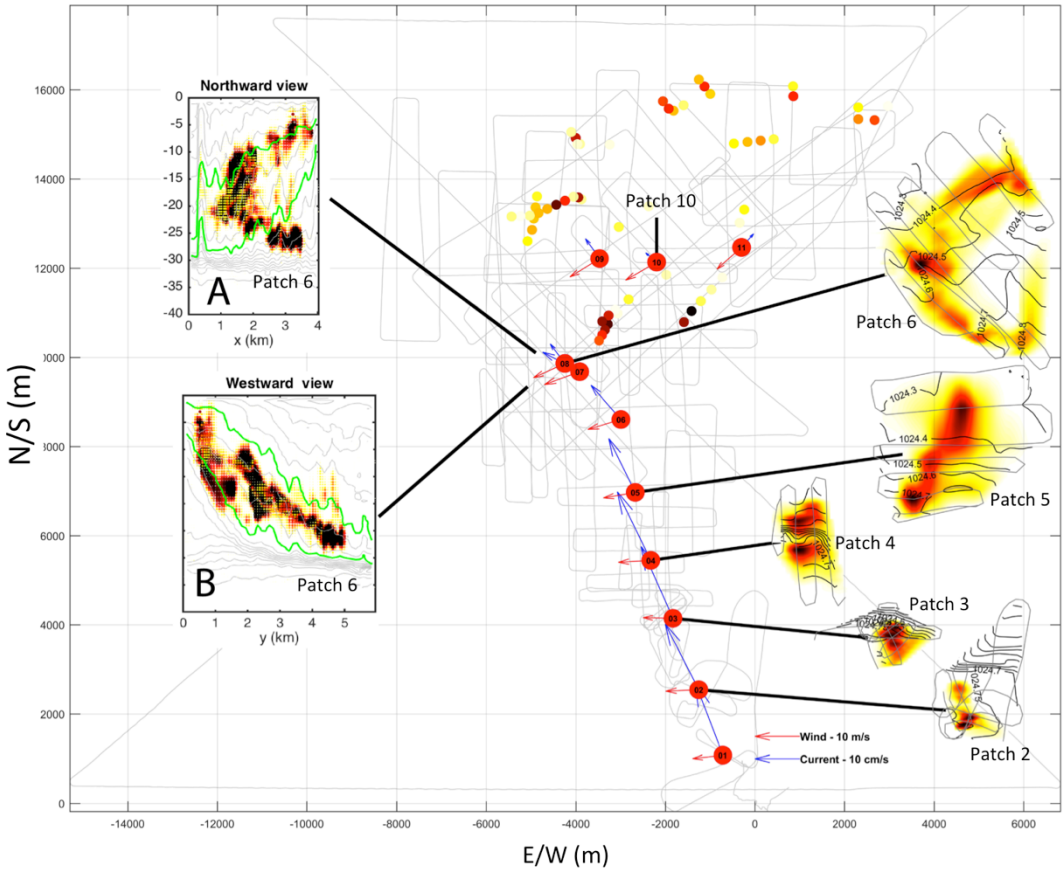

Figure 36. Mapped patches of dye for dye injection #2. The centers of mass of dye patches are shown by numbered red dots. Shaded contours of dye concentration, contours of density, and the ship tracks of the sampling transects are offset from the actual positions but connected to them with heavy black lines and identified by patch number. Insets show Patch 6 northward (Inset A) and westward (Inset B) vertical sections with shaded contours of dye concentration in kg m^{-3}, and the 30.9 and 31.2 psu salinity isohalines in green.

Immediately following the initial injection, the dye remained within the surface mixed layer and was clearly visible from the bridge of the R/V *Norseman II* for about two hours. However, the dye patch was then subducted and advected under the fresher water north of the injection site (Figure 36). The inset panels of Figure 36 show how the dye had evolved by patch 8. The tilting isohalines (green) in the westward elevation profiles represent the subsurface expression of the front. Instead of spreading evenly through a surface layer, the dye contours parallel the isohalines as they deepen northward. The northward view reveals that this subduction occurs along a downward spiral, creating a complex shape that is not easy to integrate over. The subducted dye was tracked with the towed Acrobat system only, because the hull-mounted TSG was positioned at ~3 m depth.

Figure 37 shows the density measured by the TSG at the surface along the ship track immediately before and during dye injection #2. The surface expression of the front is evident as an abrupt transition between waters with density of 1024.5 and ~1024 kg m^{-3}. Over the course of the surveys, the front, along with the dye, is advected toward the north, resulting in a checkerboard of different locations for the front as the surveys progress. Currents in this area of the shelf are variable, but this northward advection is in accordance with surface currents measured by both the HFR (Figure 13) and nearby industry ADCP mooring Site05 (Figure 15).

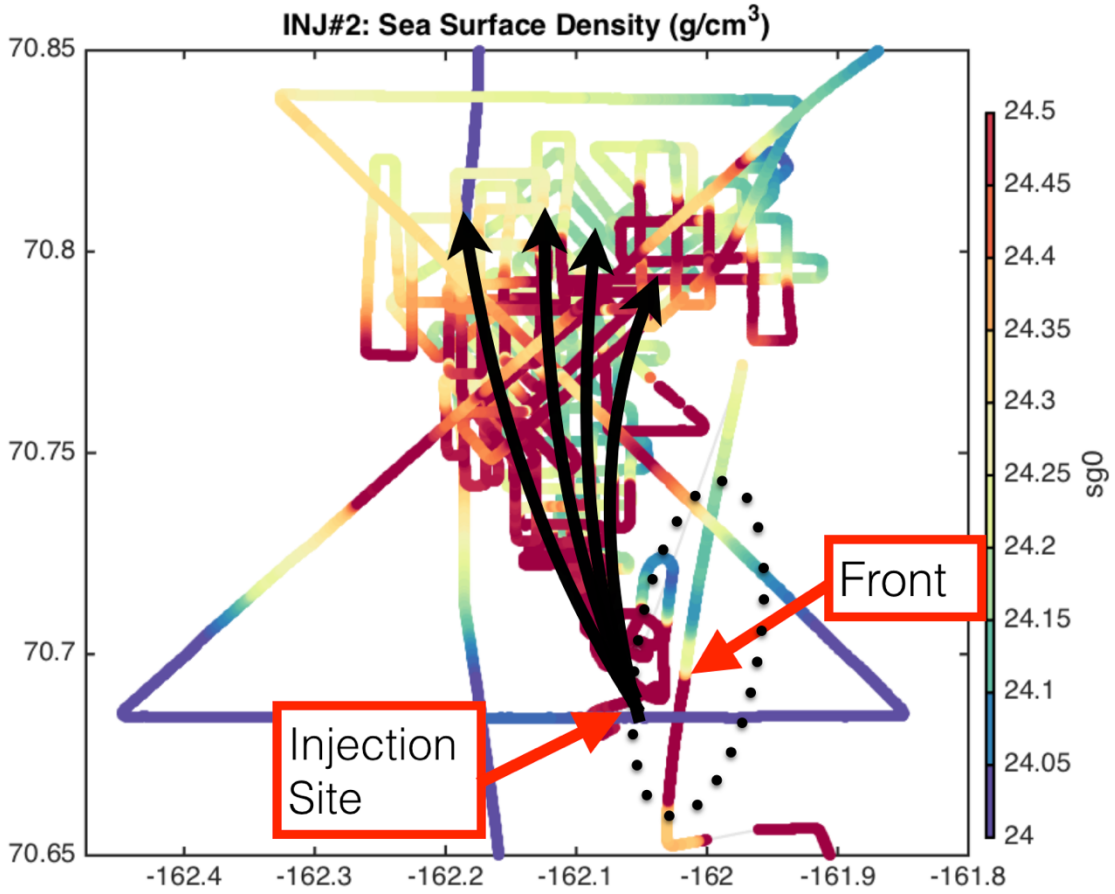

Figure 37. Surface density during dye injection #2. Ship tracklines colored according to surface density (as sigma-t = density minus 1000) measured by the TSG before and during dye injection #2. The dotted line indicates the approximate location of the front, and the black arrows indicate its approximate path.

Figure 38 shows the mean temperature, salinity, and density of each dye patch for the first 30 hours. After a brief increase in density, it and salinity remain relatively constant, with ranges of only .08 kg m^{-3} and 0.03 respectively, which indicates the subducted water is maintaining its identity as it traverses; the variability in these properties reflects the

difficulty of integrating over the dye's irregular shape. Temperature increases by ~0.2°C, which is twice the increase during injection #1.

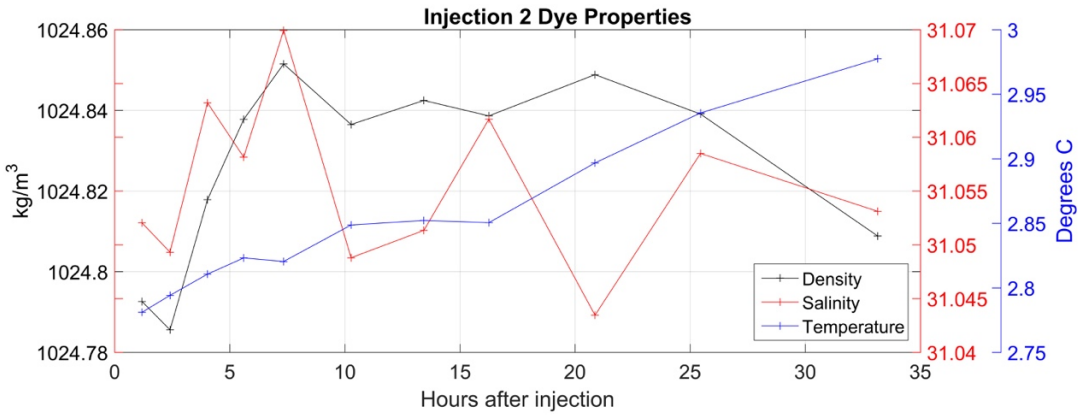

Figure 38. Time series of mean patch temperature, salinity, and density of dye injection #2.

5.2.2. Vertical Dispersion

Calculation of the vertical eddy diffusivity during dye injection #1 was possible because the dye filled the mixed layer relatively uniformly, but the active subduction of dye injection #2 created significant patchiness without a well-defined salinity gradient at the dye patch's base. However, comparison of the vertical structure of the two injections and the evolution of the patches can give hints regarding the vertical dispersion of the second injection.

Figure 39 shows density profiles and dye concentrations for both injections (upper panels) along with the dye evolution in density coordinates over time (bottom panels). Injection 1 occurred in a surface mixed layer of a two-layer system offshore of a front. The dye patch filled the upper mixed layer and remained at the surface layer throughout the experiment, though its density increased. The upper layer expanded by 5 m over the course of the experiment, and so the thickness of the dye also increased, dispersing linearly over the first 40 hours. Dye mixed mainly into higher density water throughout the experiment (Figure 39, lower left).

In contrast, during the second injection onshore of a front, the dye patch quickly subducted under the fresher body of water to the north (Figure 36). During the surveys, the mean density of the dye patch increased by 0.05 kg m^{-3} in the first 5 hours, then remained fairly constant (Figure 39), implying that the water mass the dye followed into the middle of the water column mixed little with the upper and lower layers. However, in this less stratified environment, the dye mixed into fresher/light water above as well as the denser water below, which is consistent with the warming of the dye patch noted earlier.

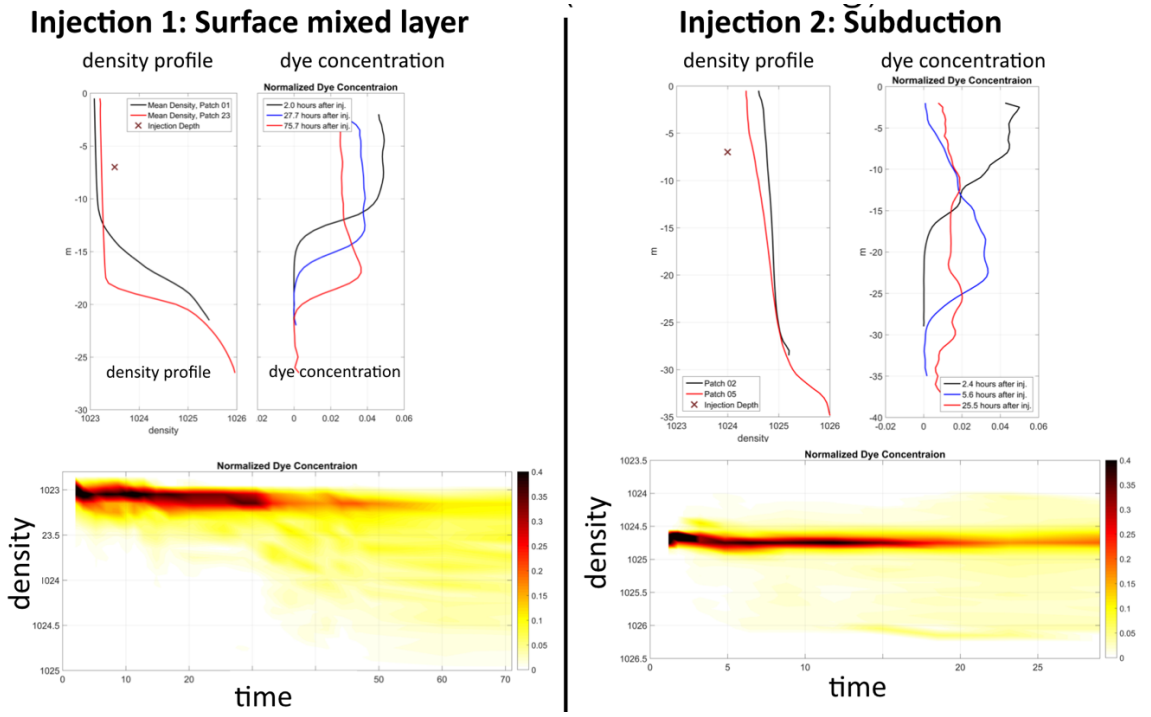

Figure 39. Evolution of dye injections #1 and #2. Left, top: injection #1 density profile and dye concentration. Left, bottom: dye evolution in density coordinates. Right, top: injection #2 density profile and dye concentration. Right, bottom: dye evolution in density coordinates.

5.2.3. Horizontal Dispersion

We were only able to calculate horizontal dispersion of dye injection #2 for the first 30 hours due to the complexity of the patch shape and its subduction. The characteristics of the patch evolution make it difficult to reliably compute dye inventories complete enough to make stable calculations of statistical moments of the dye distribution. However, the second moment of the dye patch (Figure 40) shows a steady increase during that time; K_H was calculated to be 3.7 m^2 s^{-1} before the subduction and 34 m^2 s^{-1} after subduction—an order of magnitude increase.

Figure 40. Second moment of the dye patches of dye injection #2.

In sharp contrast to the analysis of the dye, plots of drifter statistics (Figure 41) show that the variance of the drifter cluster remains low throughout the entire experiment. There is little evidence of an inertial signal in velocity, unlike the first dye injection. Unlike the mean temperature of the dye patch (Figure 38), SST increases by almost 2°C but then decrease again, confirming the complex structure of the front at the surface. The second moment of the drifter cluster, as calculated via pairwise comparisons, is an order of magnitude smaller than that of the dye patch, and even decreases as the drifters converge at the end of the day. The horizontal eddy diffusivity, K_H, calculated via equation (1) oscillates around zero as the drifters diverge and converge. It is clear from the comparison that the subduction of the dye greatly enhanced its dispersion, and that conditions at the surface were very different from those within the intrusion.

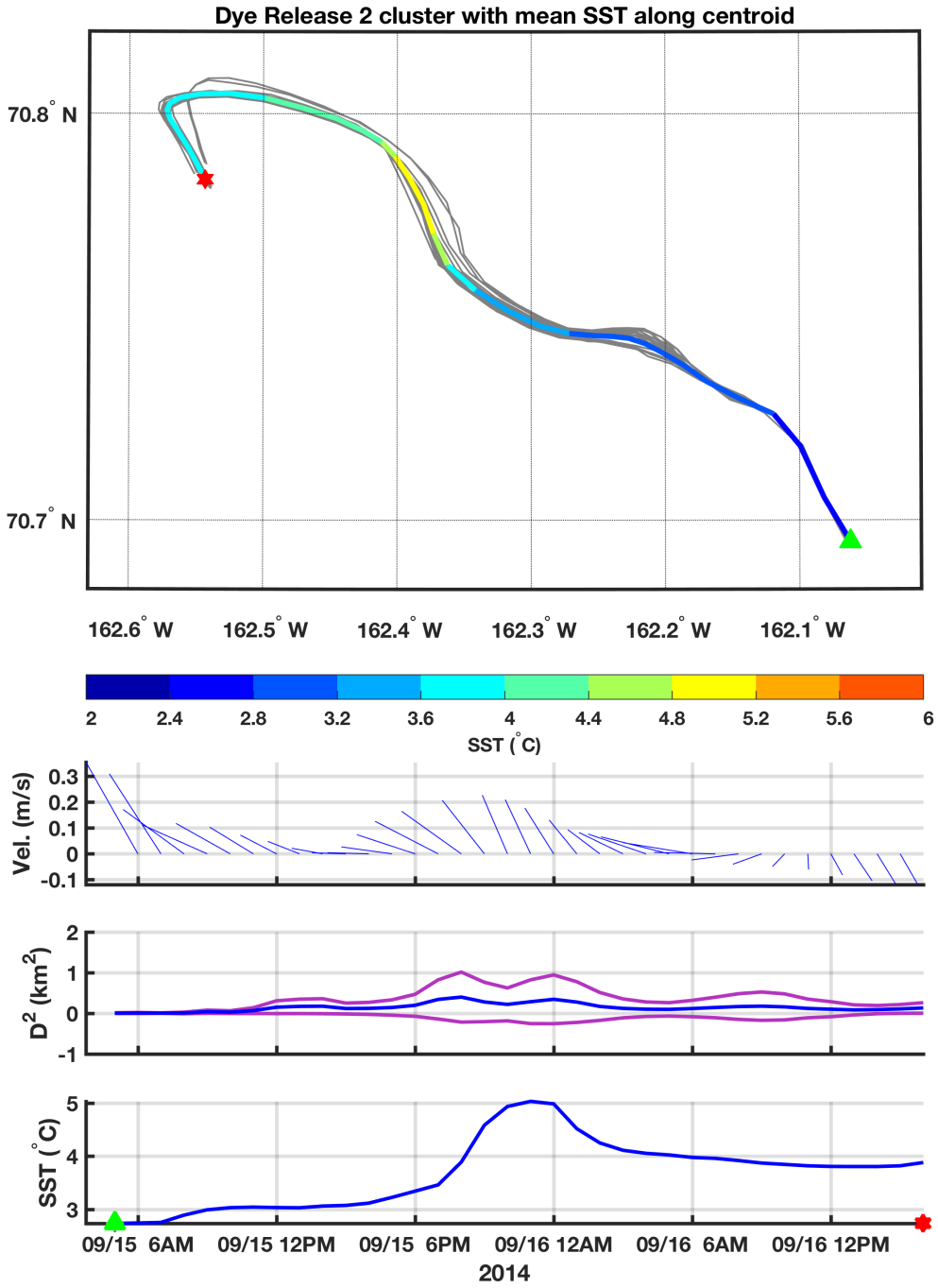

Figure 41. Drifters released during dye injection #2, September 15–16, 2014. The top panel contains the trajectories of each drifter in the cluster (gray) and the mean SST measured by the drifters plotted along the positions of the center of mass (color). Below are time series of the velocity of the center of mass, the second moment (i.e., spreading) of the drifter cluster (blue) +/– one standard deviation (purple), and the mean SST measured by the drifters.

5.3. 2015 Dye Injection #3

The 2015 dye study commenced with a surface injection of Rhodamine dye in the center of the box outlined in Figure 18. The dye was tracked with shipboard surveys as the patch evolved throughout the 42-hour dye study. The larger-scale survey was done before the dye release to measure T-S properties in the vicinity of the dye study. Dye concentration measurements are restricted to those by the TSG at 3 m depth, though the physical variables were measured throughout the water column by the Acrobat.

5.3.1. Dye Patch Evolution and Advection

In 2014, the dye injections were performed on either side of the front between MW and mid-shelf water. The setting for dye injection #3 was near the location of dye injection #2, but in 2015, the water was much warmer, slightly fresher, and distant from any MW. Again, we performed an injection into the surface layer and seeded the patch with 10 satellite-tracked drifters. Bad weather made data collection particularly challenging; winds were up to 22 knots and there were 6–7 ft seas. Despite this, we were able to successfully survey the dye extent 19 times and transmitted these maps to Arctic ERMA in near real time. The injection parameters for 2015 dye injection #3 are summarized in Table 1 and VMP parameters are summarized in Table 2.

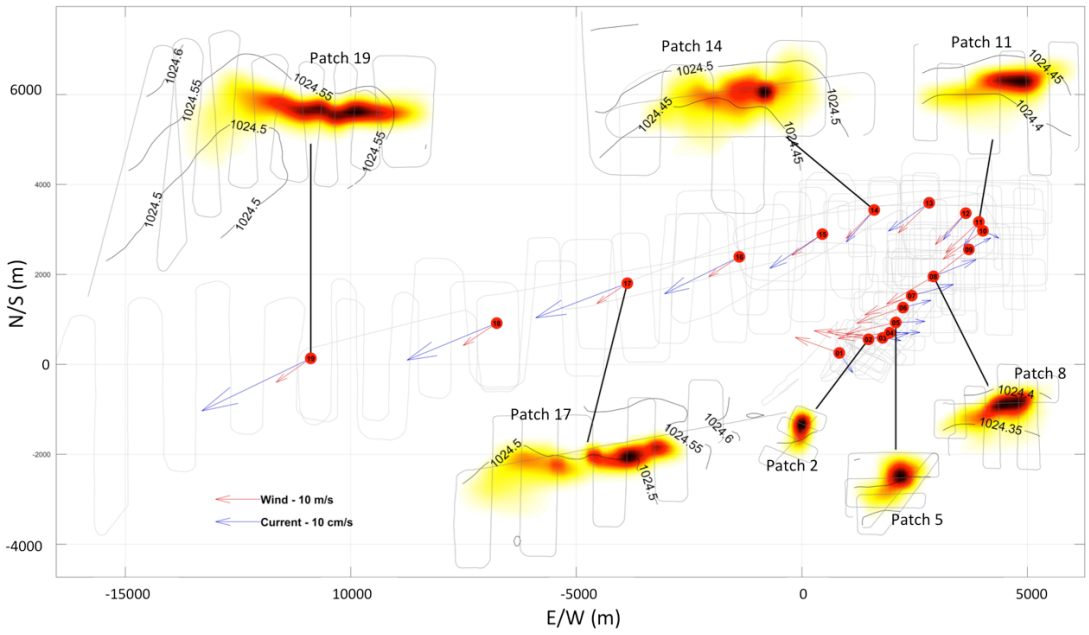

Figure 42. Mapped patches of dye for dye injection #3. The centers of mass of dye patches are shown by numbered red dots. Shaded contours of dye concentration, contours of density, and the ship tracks of the sampling transects are offset from the actual positions but connected to them with heavy black lines and identified with the patch number.

The dye moved to the northeast initially, then sharply reversed direction and went east-southeast (Figure 42). The mapped surface dye patches show that immediately after injection, the dye has a Gaussian distribution; the core of the dye path is contained within a 400 × 400 m^2 area, and at detectable concentrations, the entire patch occupies an area of 800 × 800 m^2. In the survey of the final patch, the dye has been stretched and extended along isopycnals. Dispersion and straining has elongated the patch extensively, with the dye now covering an approximate area of 2 × 60 km^2 oriented, for the most part, along the surface density gradient.

The wind was strongly northeasterly through most of the 2015 field season, though both the dye and drifters (shown below) moved up-wind initially. It isn't until patch 10, 15 hours after the injection, that the dye trajectory reverses direction. Once it does, it is swiftly advected in the direction of the wind, accelerating even as the wind slackens through patch 19.

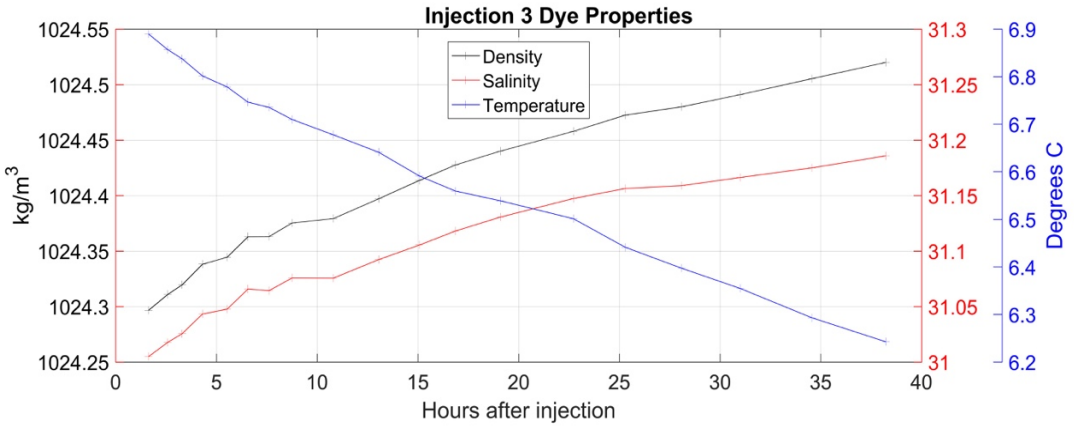

Figure 43. Time series of mean patch temperature, salinity, and density of dye injection #3.

During the surveys, the dye patch's density and salinity increased, and its temperature decreased (Figure 43). There is little variation in the rate of these changes, reflective of the more homogeneous nature of the physical environment relative to that of 2014. The changes that occur are consistent with vertical mixing and deepening of the mixed later. In the vertical sections of density (Figure 44), it appears the mixed layer did deepen slightly. The wave-like oscillations of the pycnocline in that figure are due to the ship's traversing the sloping isopycnals that the dye patch is stretched along, but there is a deepening of mixed layer depth below the dye patch from roughly 14 m deep in the transects across patch 14 (not shown) to 15–16 m deep in the transects across patch 19.

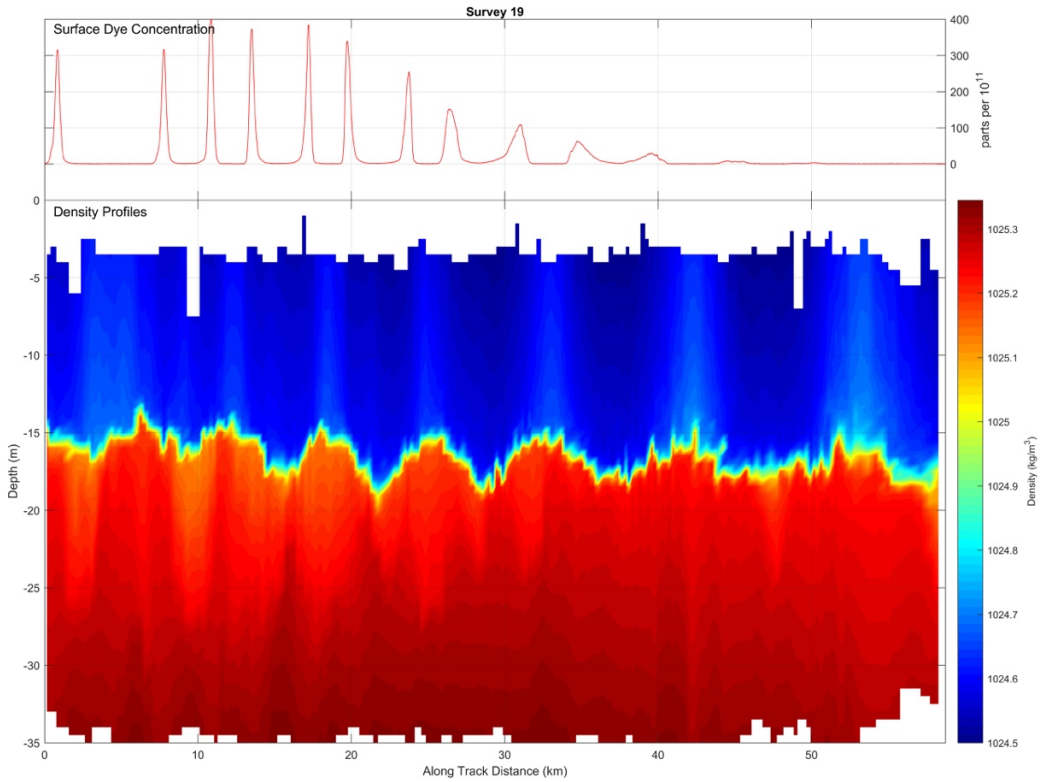

Figure 44. Vertical section of density with surface dye concentration, patch 19, dye injection #3. The top panel is surface dye concentration measured by the ship's TSG system along the ship track as it performed the survey of patch 19. High values occur when crossing the dye patch. The bottom panel is a vertical section of density along the ship track.

5.3.2. Vertical Dispersion

Because of the lack of dye concentration measurements at depth in 2015, vertical diffusion calculations based on dye are not available. However, the VMP was deployed at three stations consisting of multiple full-depth casts to approximately 35 m. The first two stations were at the site of the deep dye injection, ~1° north of dye injection #3, but the third station was conducted immediately prior to and near the surface release. Turbulence microstructure was returned consistently from 5 m to 30 m. The first two stations showed a more distinct two-layer structure, as can be seen in Figure 45, panels e and h.

Turbulence and mixing was present throughout the water column. The dissipation (ε) and mixing (K_v) decrease from a near-surface maximum, with an increase near the bottom 5 meters, likely due to the instrument penetrating into the near-bottom log-layer. It should be noted that the three turbulence stations suggest that the vertical structure of turbulence on the Chukchi is highly heterogeneous in space and time.

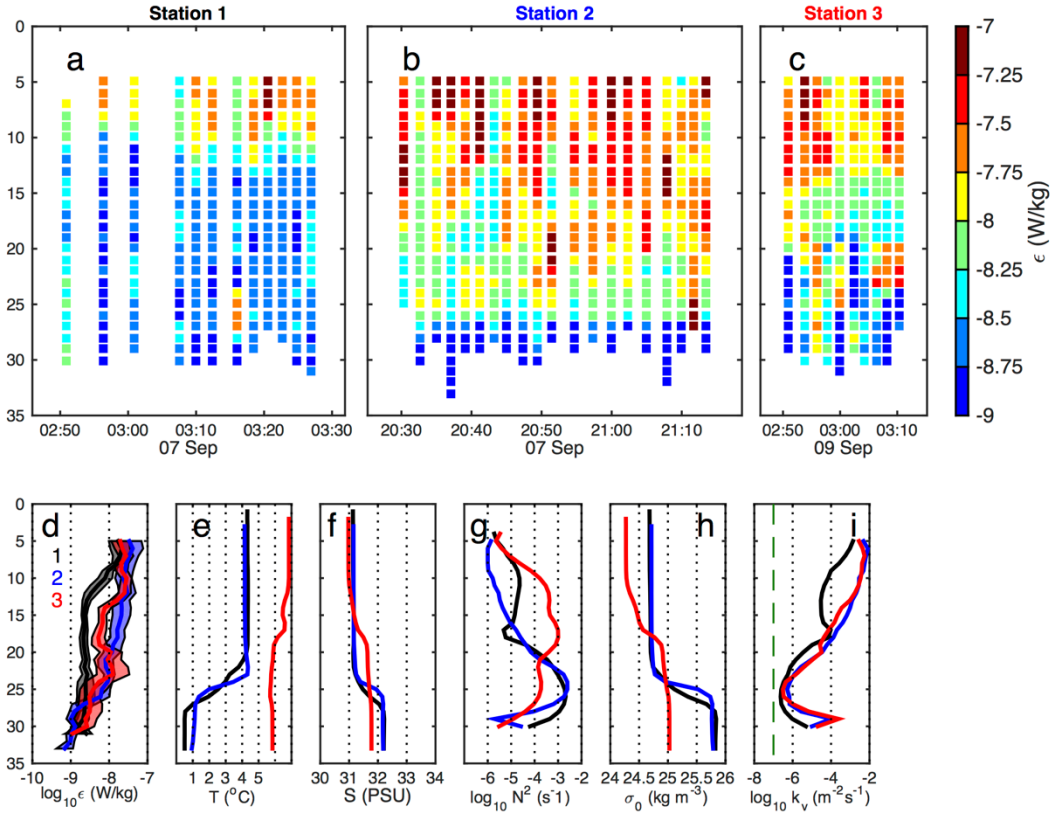

Figure 45. Summary of 2015 VMP stations 1–3. The upper three panels show the vertical structure of dissipation over time for the three stations occupied. Lower panels show mean vertical profiles (from left to right) of dissipation, temperature, salinity, N^2, density, and diffusivity.

5.3.3. Horizontal Dispersion

Comparison of K_H calculated from the second moment of the dye (Figure 46) and drifters (Figure 47) shows the two methods of measurement give consistent values; averaged over the 2 day experiment, $K_H = 7.4$ m^2 s^{-1} for dye and 7.1 m^2 s^{-1} for the drifters. That is likely because the dye calculations had to be based on surface measurements alone in 2015, so both measured the same environment. This is echoed in the similarity of SST measured by drifters and the mean temperature of the dye patch shown earlier. The trajectories of the two differ, however, because the drifters are more responsive to wind and waves than the dye is. For a surface-constrained tracer, such as oil, in an area without strong fronts, a

valuable measure of horizontal dispersion can be gained from drifters alone, even if they don't follow the same trajectory as the tracer.

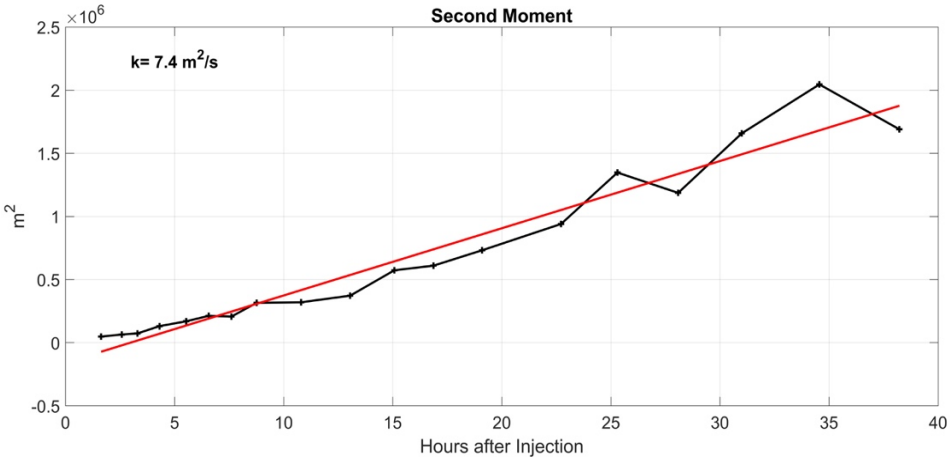

Figure 46. Second moment of the dye patches of dye injection #3.

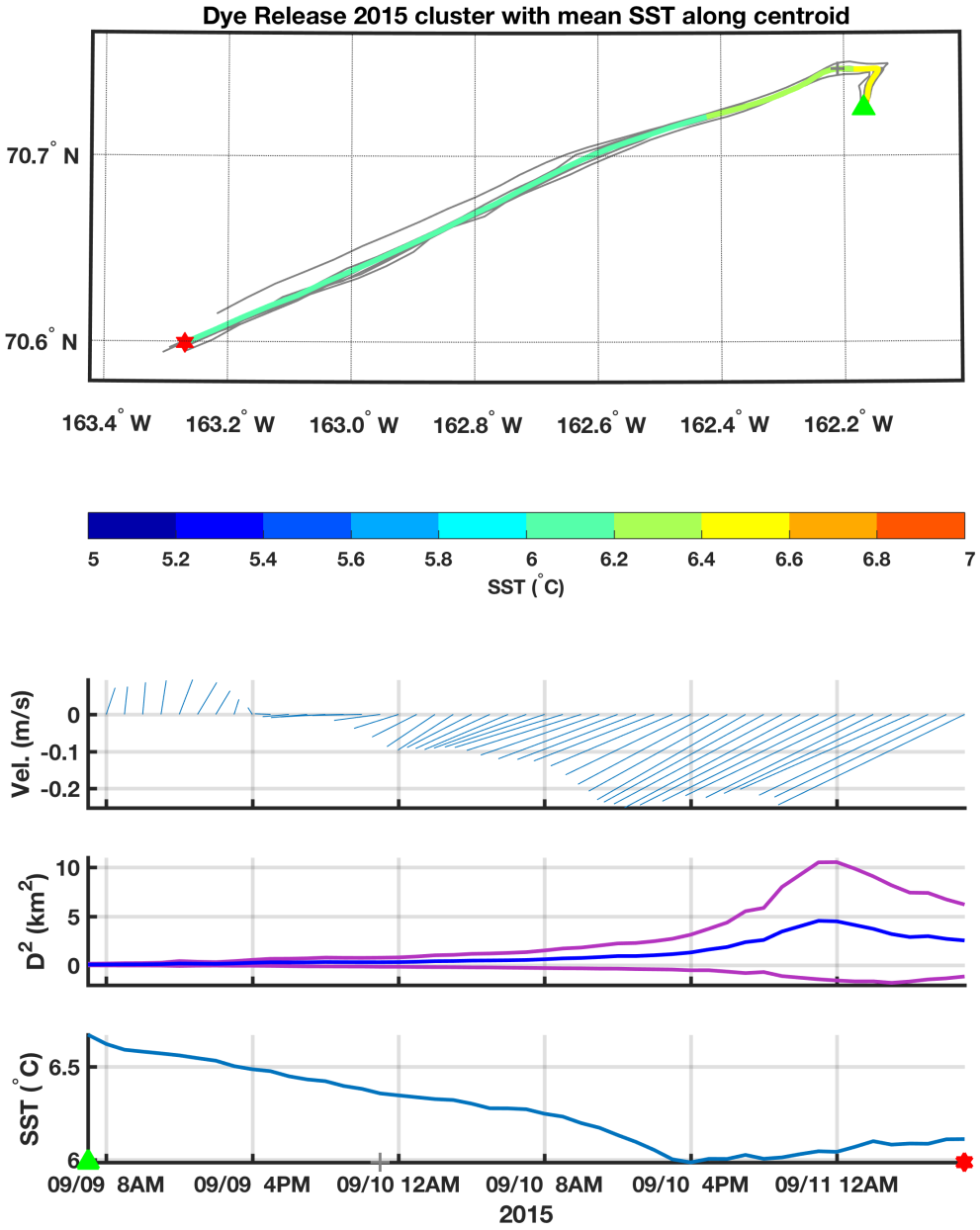

Figure 47. Drifters released during dye injection #3, September 9–11, 2015. The top panel contains the trajectories of each drifter in the cluster (gray) and the mean SST measured by the drifters plotted along the positions of the center of mass (color). Below are time series of the velocity of the center of mass, the second moment (i.e., spreading) of the drifter cluster (blue) +/– one standard deviation (purple), and the mean SST measured by the drifters.

6. Discussion

In this section we discuss the three dye releases and highlight similarities and differences between the three field efforts. All three releases were conducted in the surface mixed layer and the dye quickly occupied the entire mixed layer after initial injection. Diapycnal mixing was low to moderate during all three dye releases despite considerable wind forcing. In all cases, advection was a prominent process with the patches becoming anisotrophic as they stretched along density gradients.

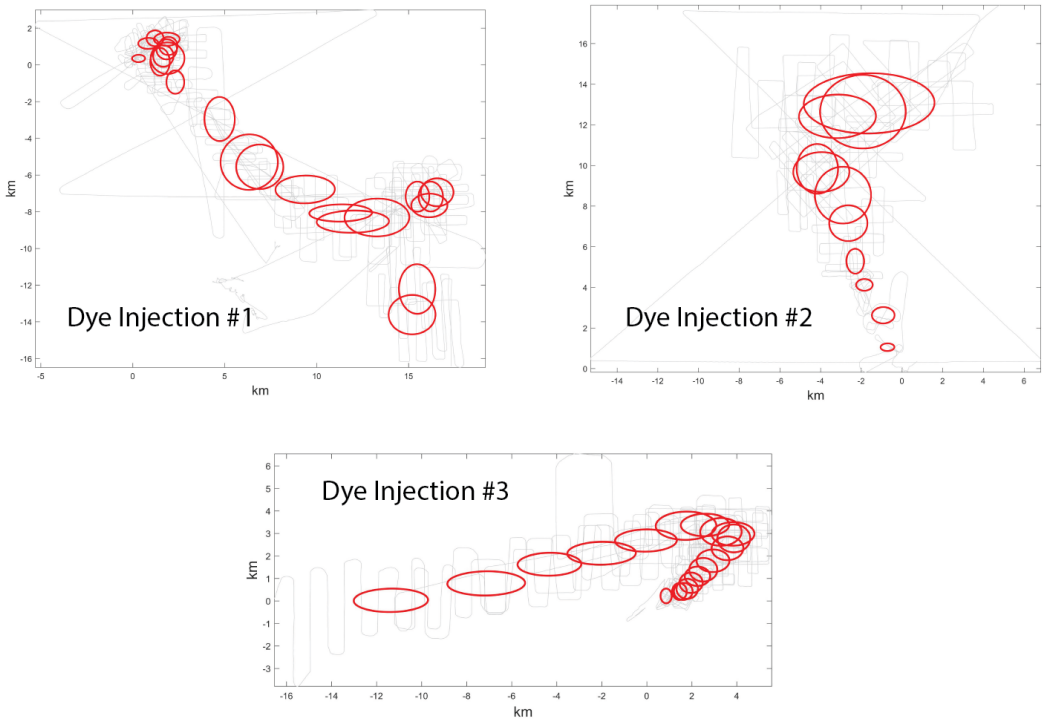

Figure 48. Summary of dye injections.

During the first dye release in 2014, the pycnocline was strong with a density difference of ~3.5 kg m^{-3} between the surface layer and bottom layer, and with, at least initially, an intermediate layer of warmer water. The surface waters consisted mainly of meltwater (MW) with low salinities (29 psu or less) from in situ ice melt and moderately cold temperatures (~2°C). The strong two-layer system inhibited diapycnal mixing and entrainment, though during the course of the experiment, the intermediate layer was mixed away and there was some mixing between the MW and winter water (WW). The VMP profiles show no turbulent mixing in the bottom layer WW. This is also evident from the evolution of the dye, which remained within the mixed layer as it was advected toward the south and southeast.

The second dye release in 2014 occurred inshore of a front in an area with strong horizontal density and temperature gradients. Initially, the dye patch evolved in a similar

manner to the first, but then there were notable differences. The dye remained visible at the surface for about two hours as it dispersed through the mixed layer, but then the dye subducted at a front between offshore MW and the northward advecting ACC. The dye transitioned into an intrapycnal subsurface dye patch with a complex shape and trajectory that could only be tracked for ~1 day (Figure 36). The subsequent dispersion was about three times larger during the subduction phase.

In September 2015, following a year of record low sea ice, the dye release took place in less stratified water with fewer surface frontal features. Turbulence and mixing was present throughout the water column as measured directly using the VMP instrument, with near-surface and near-bottom local maxima in mixing. The near-bottom maxima was likely due to the presence of a well-developed bottom boundary layer. The dye was strained and dispersed over the 19 realizations of the patch that we performed, while the mixed layer deepened.

Dispersion was estimated for each main dye release by making a detailed inventory of the dye patch over time and is summarized in Table 4 and Figure 49.

Table 4**.** Dispersion estimates for each field experiment.

Dye Injection #	Average dispersion (m^2 s^{-1})	Comment
1	7.7	Surface release and for period with well-defined dye patch
2	33.2	Surface release with subsequent subduction
3	7.4	Surface release with high wind and wave environment

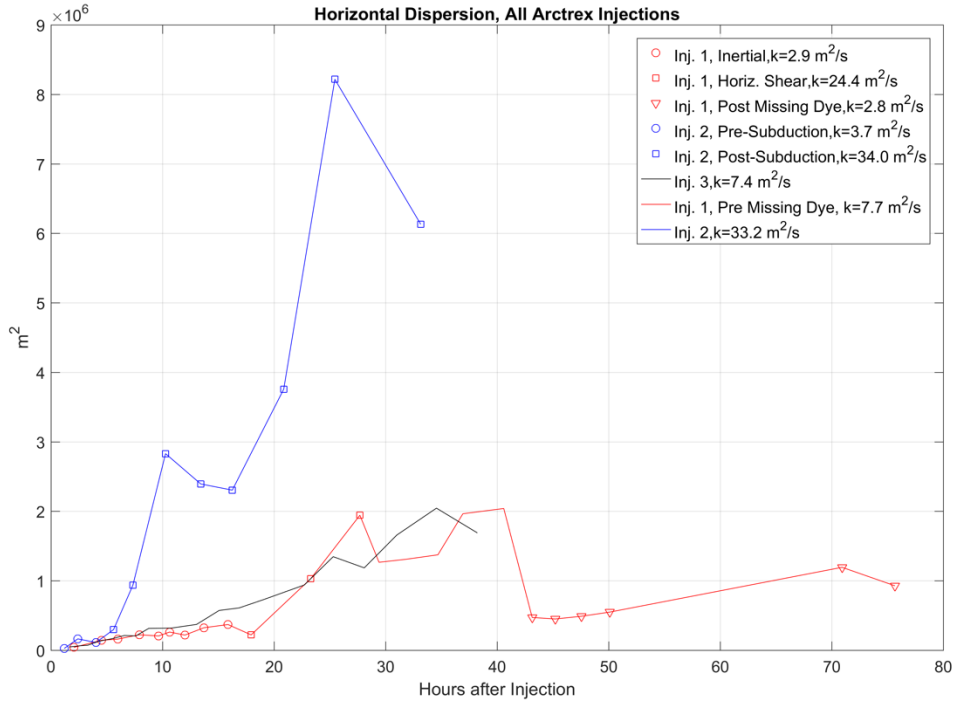

Figure 49. Horizontal dispersion, all ARCTREX injections.

The overall mean dispersion from all three experiments was found to be ~7.5 $m^2 s^{-1}$. The average dispersion from dye injection #1 in 2014 was estimated at 7.7 $m^2 s^{-1}$ over the duration of patch surveys where >90% of the released dye was detected. This is close to the overall mean dispersion from all three experiments. Dispersion during the second release in 2014 was close to an order of magnitude higher during the time period when dye was subducting along isopycnals in the frontal region. We estimate that the dispersion during this phase was ~34 $m^2 s^{-1}$, with pre-subduction values being ~3.7 $m^2 s^{-1}$. Dispersion values for the third experiment were 7.4 $m^2 s^{-1}$, close to those of the first surface experiment in 2014. Estimates of dispersion determined from the ARCTREX project fall within those reported in the literature for shelf and coastal environments by Sundermeyer and Ledwell (2001) and Ledwell et al. (2004).

The field observations showed that dye distributions were significantly influenced by shearing and straining on scales of the mixed-layer depth in the vertical (5–15 m) and 1–50 km in the horizontal. For example, during dye injection #1 in 2014, the dispersion estimated during different legs of the survey was 2.9 $m^2 s^{-1}$ immediately after injection, a period that was dominated by inertial motions. Later on, the patch experienced horizontally sheared geostrophic flow and the dispersion was estimated to be 24.4 $m^2 s^{-1}$. Simultaneous increases in the horizontal second moments of the dye patches were superimposed on these larger-scale distortions.

6.1. Internal Waves and Vertical Shear

There is evidence of internal waves in the study area. During discussion of the cross-shelf transect performed before dye injection #1, we noted that between the two well-defined layers of MW and WW in the water column offshore, there is an almost 10 m thick pycnocline at ~25 m depth (Figure 8). This border between the layers undulates with vertical excursions of 5 m with an apparent wavelength of 15–20 km as the ship moves. This Doppler shift can be corrected. Assuming that these are internal waves, they are constrained to propagate southward to fulfill $f < \omega$; propagating onshore, the actual wave length would be more like 18–23 km assuming a ship speed of 3 m s^{-1} and an internal wave speed of $c = \sqrt{\frac{g'(H_1 H_2)}{(H_1 + H_2)}}$, where H_1 and H_2 are the thicknesses of the upper and lower layers and g' is reduced gravity defined by $g' = g\Delta\rho/\rho$ where g, ρ, *and* $\Delta\rho$ are gravitational acceleration, density, and the density difference between the upper and lower layers. Taking $H_1 = H_2 = 20$ m and $\Delta\rho$ = 3.0 kg m^{-3}, c corresponds to 53 cm s^{-1}. So it is possible that internal waves are available to mix the water column within the study area.

Early and late during dye injection #1, there were prominent inertial motions that might be expected to increase mixing. That process would manifest itself through spikes in the shear between the surface and lower layers, and would contribute to variability in the rate of change of the dye's salinity and significant semidiurnal changes in the salinity. The inertial shear spikes are clearly evident in the time series from the shipboard ADCP data (Figure 50). However, the variability in the dye's salinity is insignificant compared to the overall variability of dye salinity in any one patch and the overall change through the surveys. That suggests that mixing is not significantly enhanced by inertial wave motion. Also, whereas vertical shear does contribute to dispersion in the first and final third of dye injection #1, the decrease in vertical shear between hours 20 and 40 is coincident with an increase in dispersion that corresponds to an increase in the horizontal density gradient (and horizontal shear), so vertical shear is not always important.

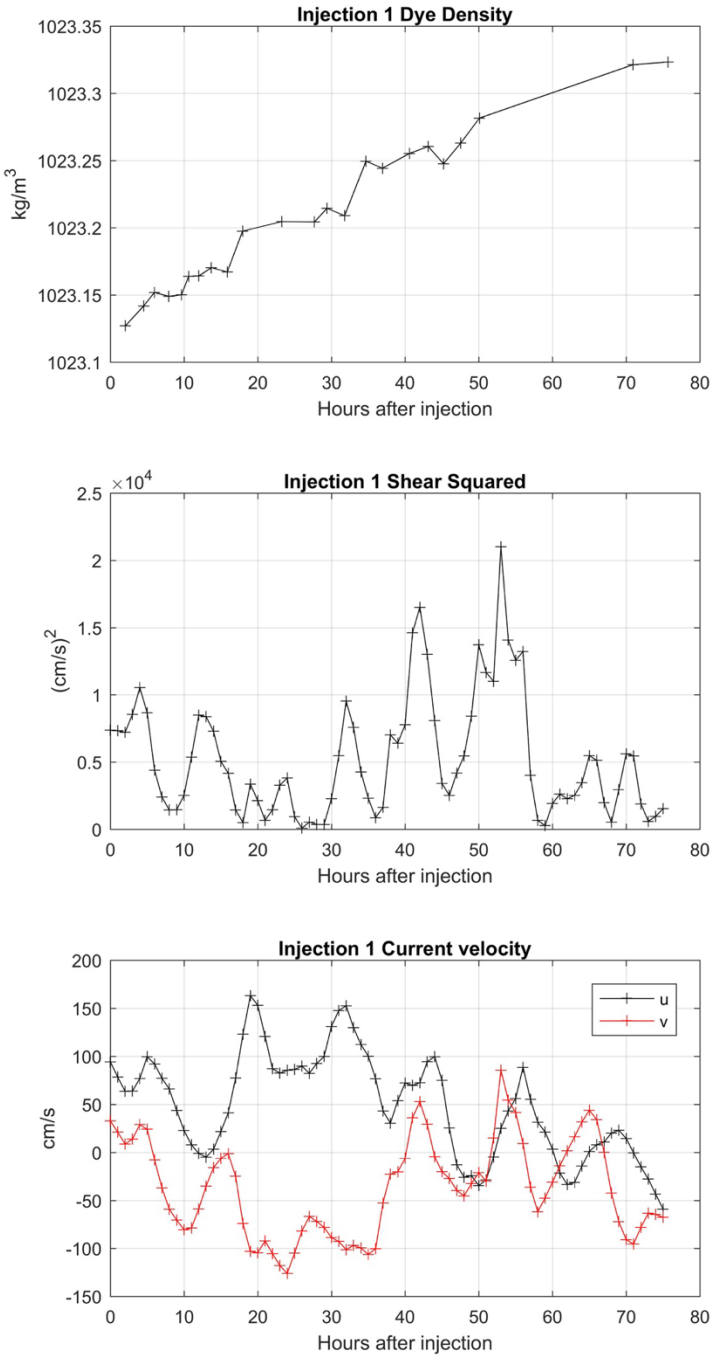

Figure 50. Time series of mean patch density, shear, and velocity. The upper panel shows density of dye over the survey. The middle panel shows shear squared between the upper and lower layers of the water column. The lower panel is current east-west (U, black) and north-south (V, red) velocity from shipboard ADCP data.

6.2. Wind Mixing

To establish a physical basis for the role of vertical mixing driven by wind stress, we utilize a one-dimensional model to estimate mixing potential (Denman and Miyake 1973) following the technique of Hauri et al. (2013). Using the hourly time series of wind speeds collected at the ConocoPhillips meteorological buoy, the rate of energy transfer from the wind into the water column (J m^{-2} s^{-1}) is:

$$\frac{\delta E}{\delta t} = \rho_a m C_d u^3$$

Where ρ_a (1.2 kg m^3) is the air density, $m \sim 10^{-3}$ is an efficiency factor, $C_d \sim 10^{-3}$ is the drag coefficient, and *uu* is the wind speed at 10 m above sea level. In a simplified two-layer ocean, the potential energy content between an upper homogeneously mixed layer (density ρ_1 and thickness h_1) and a bottom layer (density ρ_2 and thickness h_2) is given by:

$$PE = \frac{1}{2} g h_1 h_2 (\rho_2 - \rho_1)$$

where Potential Energy (*PE*) (J m^{-2}) is the amount of energy required to overcome stratification and mix the water column. Using measurements of stratification taken in the two-layer offshore water in 2014 (Figure 8) and defining the mixed layer depth as the maximum of $\partial\rho/\partial z$, we utilize values of h_1 = 18m, h_2 = 20m, ρ_1 = 1023.05 kg m^{-3}, and ρ_2 = 1026.01 kg m^{-3}, such that *PE* = 5,221 J m^{-2}. For 2015, PE is three times lower due to the lower stratification then; using h_1 = 25 m, h_2 = 15m, ρ_1 = 1024.7 kg m^{-3}, and ρ_2 = 1025.7 kg m^{-3}, *PE* = 1,837.5 J m^{-2}.

PE can then be compared to the persistence of the wind energy (*WE*) of individual wind events. *WE* is determined by integrating the rate of energy transfer, $\partial E/\partial t$, over the duration of an event, where an event is defined as a period of time when $\partial E/\partial t$ exceeds a threshold value of 0.2×10^{-3} J m^{-2} s^{-1}. In 2014, there was a prolonged wind event when wind energy inputs to the water column were significant enough to overcome stratification and mix the two-layer system (Figure 51); dye injection #1 occurred a day after the beginning of this event, and dye injection #2 occurred at the end of it. Though the winds were lower in 2015 and *WE* was roughly half (Figure 52), the lower stratification meant that 2015 also had events that could overcome stratification and mix the water column; dye injection #3 occurred at the beginning of one such event.

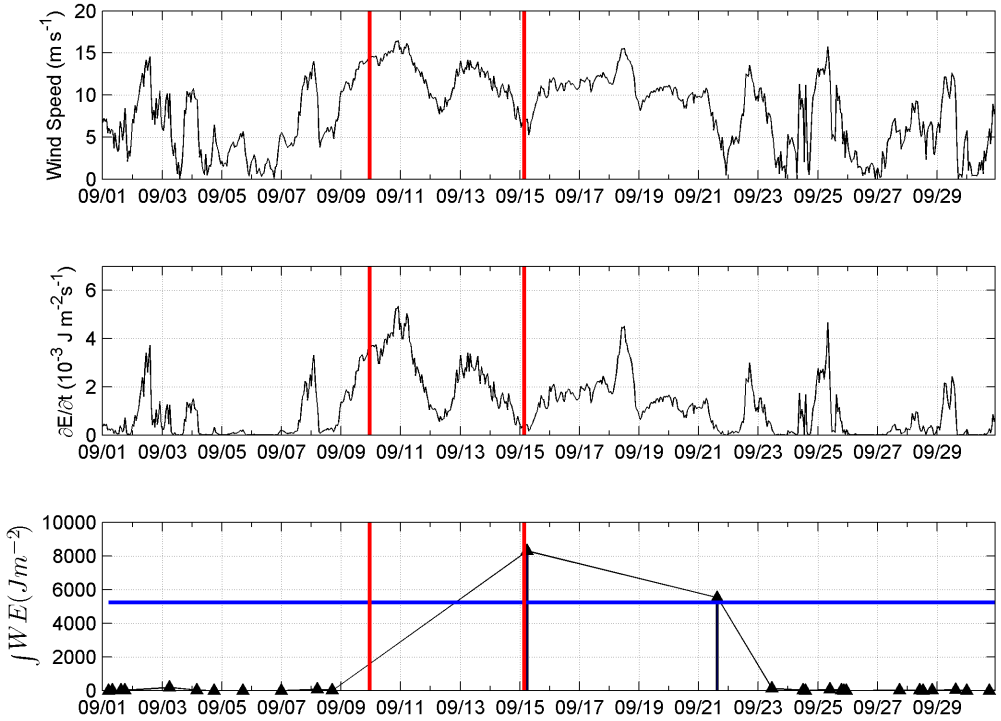

Figure 51. Analysis of wind mixing, September 2014, Klondike ConocoPhillips meteorological buoy. Top panel: wind speed. Middle panel: rate of energy transfer from the wind into the water column (∂E/∂t). Bottom panel: the sum of wind energy per event. Red vertical lines indicate the times of the two Rhodamine dye injections.

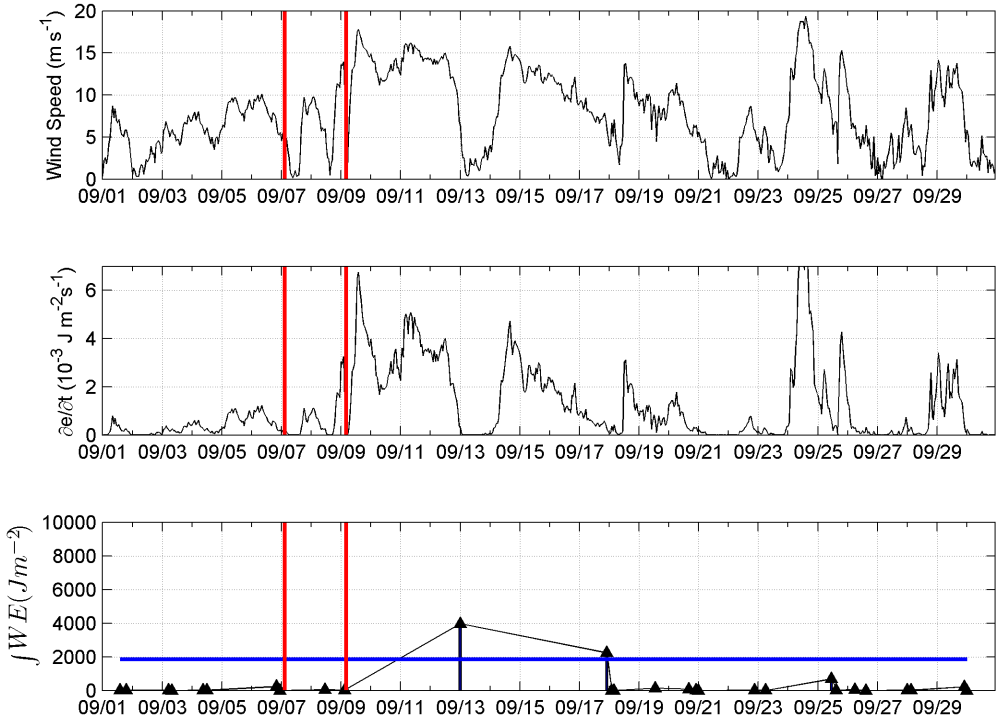

Figure 52. Analysis of wind mixing, September 2015, Klondike ConocoPhillips meteorological buoy. Top panel: wind speed. Middle panel: rate of energy transfer from the wind into the water column (∂E/∂t). Bottom panel: the sum of wind energy per event. Red vertical lines indicate the times of the two Rhodamine dye injections.

These findings are consistent with Hauri et al. (2013), in which they found that periodic late-season wind events, most frequently occurring in September and October, contained the potential to overcome stratification and mix the water column. It also reflects the results of Kawaguchi et al. (2015), who observed wind-forced mixing that stirred the upper water column and resulted in a deepening of the surface homogeneous layer. Thus it is likely that during dye injections #1 and #3, the observed deepening of the mixed layer is due to wind mixing.

6.3. Modification of Advection by Vertical Mixing

Throughout ARCTREX's experiments, dye patches advected and strained along the direction of local isopycnals. However, modifications of the dye patches' physical properties also caused them to move relative to the background salinity/density fields; they moved faster than isohalines when fronts or horizontal density gradients were advected normal to their orientation. We can investigate the contribution of vertical mixing to this process by using the value of K_v that was previously estimated assuming only vertical mixing changes the mean salinity of a dye patch. In this case, we apply a 1-D salt balance equation to the mixed layer's average salinity in the direction of the horizontal density gradient (i.e., perpendicular to isopycnals), which is:

$$\frac{\partial s}{\partial t} = -u\frac{\partial s}{\partial x} + \frac{K_v}{H}\frac{\partial s}{\partial z}$$

Where K_v is the vertical eddy diffusivity, H is the mixed layer depth, u the mean current in the direction of the horizontal salinity gradient, and $\frac{\partial S}{\partial x}$ and $\frac{\partial S}{\partial z}$ are the horizontal salinity gradient in the upper mixed layer and the vertical salinity gradient at its base, respectively.

Dividing by $\frac{\partial S}{\partial x}$ yields

$$\frac{\partial s / \partial t}{\partial s / dx} = -V_s = -u + \frac{K_v \frac{\partial s}{\partial z}}{H \frac{\partial s}{\partial x}}$$

Where V_s is the speed of an isohaline in the direction of the horizontal salinity gradient. Note that V_s is less than u by the mixing term. Thus the dye, which is transported at speed u, outruns isohalines by the strength of the mixing term. Using observed values for K_v = 1.7×10^{-5} m^2 s^{-1}, $\frac{\partial S}{\partial x} = 5 \times 10^{-5}$ m^{-1}, and $\frac{\partial S}{\partial z} = 0.5$ m^{-1} results in the second term on the right-hand side being equal to 0.011 m s^{-1}, which is close to the observed difference between the movement of the dye and that of an isohaline in the upper mixed layer, providing an explanation for this behavior.

6.4. Response Agency Interaction—Arctic ERMA

One goal of the ARCTREX project was to coordinate our field effort with NOAA's Arctic ERMA and work toward real-time data input into their response system. We worked closely with the Arctic ERMA team of the NOAA's Office of Response and Restoration in Seattle prior to, during, and after our two field seasons in 2014 and 2015. In particular, we collaborated with Dr. Amy A. Merten, the current chief, Spatial Data Branch/Assessment and Restoration Division; in 2014 with Nicolas Eckhardt and Zachary Winters at ERMA; and in 2015 with Aaron Racicot at ERMA. Before the 2014 experiment, we interfaced with the ERMA GIS team and worked out a process to send data files of dye patch extent from the field to ERMA for them to display on the Arctic ERMA page (https://erma.noaa.gov/arctic/erma.html) in near real time.

We also conducted post-cruise phone conferences discussing lessons learned, and implemented improvements for the 2015 field season. Specifically, the following improvements were made for the 2015 experiment:

1. HFR surface current maps from the National HFR Network were included in the data feeds. In 2014, the national server was down due to a server rebuild.

2. On the ship, altered details of dye patch shapefiles allowed production to be partially automated, speeding the dissemination of patch locations via the Internet.

3. The color-scheme representation of dye concentrations was improved. The units of dye concentration in 2014 had not been explained precisely enough prior to the experiment, leading to delays in the shapefile production.

4. An API interface was developed within ERMA that simplified the input of new data streams into the interface. This improved input of the dye shapefiles, but ironically delayed the posting of drifter tracklines. On our end, getting the filenames to ERMA before the experiment started would have allowed time for the necessary changes to the code to propagate to the production server.

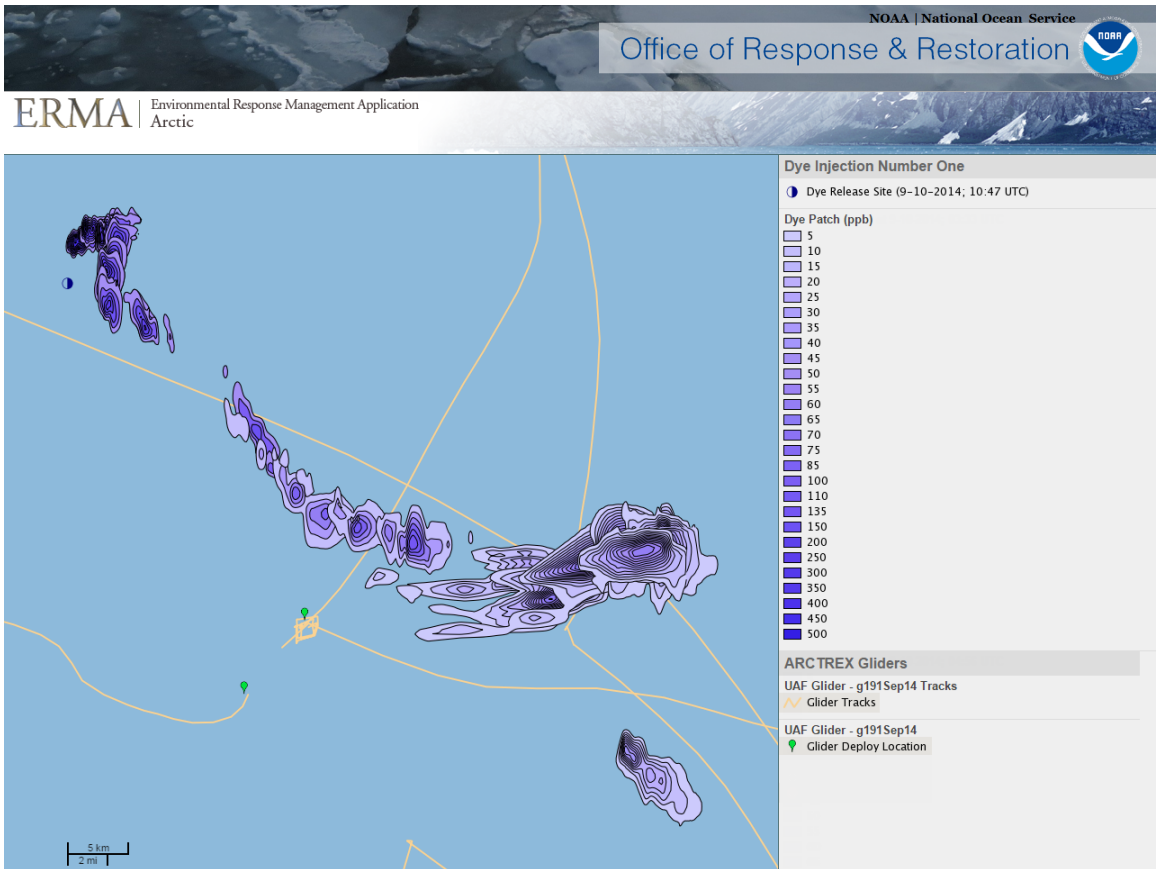

Figure 53. Arctic ERMA web display of dye injection #1, 2014. The Arctic ERMA GIS layer shows mapped dye patch extensions over time in an interactive web display.

Figure 53 shows an active GIS layer from NOAA's ERMA website during the ARCTREX project. Each dye patch in this visualization was transmitted to ERMA, enabling them to produce a time series of the dye patch evolution. The ability for us to send near real-time data from the field, and for ERMA to ingest this into their management system, was a great success. We anticipate that future experiments will be able to display three-dimensional data in various GIS layers on the ERMA website from field campaigns or during a real incident.

7. Conclusions and Recommendations

The Arctic Tracer Release Experiment (ARCTREX) project was designed to explore applications for mapping spilled oil in Arctic waters. This experiment tested the capacity of available real-time observational technology to map a dye plume that simulated an oil spill and to provide real-time data in space and time to response agencies. We utilized the existing infrastructure of the University of Alaska's ongoing ocean-observing efforts in the Chukchi Sea, including real-time, two-dimensional surface current fields from extended-range high frequency radar and existing observing assets such as AUV gliders

and a towed Acrobat vehicle. To these we added detailed microstructure measurements of ocean turbulence, satellite-tracked surface drifters, shipboard and moored ADCP current meters, remotely sensed sea surface temperature and sea ice concentration, and dedicated dye measurements sampled with fluorometers to map a dye plume and its evolution over three periods during field seasons in 2014 and 2015.

Our results show that it is feasible to track a passive dye in detail using the technologies listed above. The effort requires high-end knowledge of operating instruments and ships and becomes significantly more difficult if there is no surface expression of the dye, such as the subducting dye in release #2 in 2014. In this case, for instance, simulating dispersed oil that has sunk down into the water column and mapping the detailed three-dimensional evolution of the plume in time and space becomes challenging. We also successfully transmitted data to NOAA's Arctic ERMA and UAF's web pages in near real time, proving that this capacity does exist in the Chukchi Sea with available technology. The results from the three dye releases show that dye patches are advected and strained horizontally over the full depth of the mixed layer. Dye injection #2 in 2014 also showed that in addition to horizontal dispersion, fronts in the Chukchi Sea can significantly alter the fate of dye (and likely dispersed oil), and can generate conditions that make tracking the dye significantly more difficult. Surface features rapidly disappear due to subduction and are only able to be tracked using undulating subsurface instruments.

Other findings include:

Currents: HFR data were used onboard to identify regions of convergent flow and to find a suitable location for deploying dye; these data were also successfully added to ERMA's real-time data feed. However, they did not resolve currents on the scale of the dye patches. Of more utility at these scales were the vertical current profiles measured by the shipboard ADCP and even the moored ADCP current meters.

Drifters: Satellite-tracked drifters were deployed throughout the ARCTREX project. Generally, the paths of the 1 m drogued surface drifters diverged from the position of the centroid dye concentration of each patch after 12–24 hours. We attribute this behavior to the shallow drogue depth of the drifters, which would make them subject to more wind-wave interaction and Stoke's drift compared to the dye patch, which is spread over the entire mixed layer. However, there were conditions when drifters provided useful parameterization of surface processes, even though the trajectories of dye and drifters diverged.

Gliders: AUV gliders were able to detect dye in the water column, transmitted their data in real time, and operated successfully in harsh weather conditions, but were not able to maneuver with the agility necessary to define dye patch for dispersion calculations. Multiple gliders operating in concert would be able to estimate patch locations in a response situation.

Environmental conditions presented a number of challenges to the field operations. Delicate instruments such as the gliders, CTD, and VMP had to be very carefully lifted over the side of the ship, and as wave heights reached 2.5 m, over-the-side operations had to be halted several times to ensure safe working conditions both for the equipment and for the operators. The shallow Chukchi Sea wave environment tends to be quite choppy compared to deep water like the Gulf of Alaska, where long-period swells and 2–3 m seas are still quite feasible to work in. Over-the-side operations tend to be very hectic when the wave periods are between 5–7 s as we experienced in the Chukchi Sea. While working on the back deck, constant vigilance was required to ensure the safe movement of personnel and instrumentation. In addition, the communications channels between the bridge and back deck personnel needed to be clear and consistent, as slight changes in ship velocity or heading would result in very different conditions at the water line. All told, the Acrobat was the most resilient instrument deployed by the ARCTREX experiment. Once it was in the water and 200–300 m of tow cable was spooled out, the instrument was fairly impervious to sea state or ship motion. At times, the sea state was too rough for safe recovery for the Acrobat so the decision was made to leave it in the water and continue surveying until the weather pattern shifted toward calmer conditions. Additionally, we had planned to use a drone to survey the dye from the air, but high winds made this impractical.

From this extensive fieldwork and analysis, recommendations emerge for future direction and research:

- Advanced observational-modeling framework: Currently, NOAA ERMA utilizes slab models or simpler circulation models in oil spill response applications. The results presented here show the need for a more complex treatment of ocean physics and dynamics. We recommend that coupled detailed observations and three-dimensional ocean modeling of dye and/or oil-in-water be performed.

- Oil-like dye: The dye used in this study, Rhodamine-WT, is excellent for detailed studies of a fully passive tracer. However, it is not a perfect simulation of oil in water, not even when dispersed. For more realistic oil spill applications, we encourage development efforts for a more positively buoyant dye with oil-like properties. Alternatively, smaller ocean experiments with oil in water would be illuminating.

- Detailed physical oceanography studies: Our fieldwork highlights the complex nature of ocean fronts and small-scale (<300 m horizontal) physics on passive tracers and their evolution in time and space. A dedicated study at these scales is recommended to build on the work presented here. This includes a critical need for near-shore dye studies of the fate of an oil spill and interaction with buoyant coastal waters.

- Lab experiments on buoyant dispersed oil droplets and their interaction with a turbulent environment: The fate of dispersed oil droplets in a turbulent boundary layer is not well studied and would be advised in order to parameterize this process into general circulation models.

8. Acknowledgments

We would like to acknowledge the captain and crew of the RV *Norseman II* for their skill and flexibility in conducting these exercises in adaptive sampling. Cayman Irving produced the drifter analysis as part of his work on the U.S. Dept. Interior, Bureau of Ocean Energy Management (BOEM) Cooperative Agreement #M12AC00008 ("Characterization of the Circulation on the Continental Shelf Areas of the Northern Chukchi and Western Beaufort Seas"). Chase Stoudt provided the figures of SSMI sea ice concentration. Elizabeth Dobbins, Hank Statscewich, and Eli Hunter provided additional data analysis and text, and prepared the report. Shell, ConocoPhillips, and Statoil provided data from their current meter moorings, and ASL Environmental Services analyzed these data. Gliders were partly funded by the Alaska Ocean Observing System (AOOS). Additional funding for the HFR array was provided by BOEM (#M12AC00008).

9. References

Aagaard, K. 1988. Current, CTD, and pressure measurements in possible dispersal regions of the Chukchi Sea. Final Report. U.S. Department of the Interior, Alaska Outer Continental Shelf Region, 255–333.

Aagaard, K., T.J. Weingartner, S.L. Danielson, R.A. Woodgate, G.C. Johnson, and T.E. Whitledge. 2006. Some controls on flow and salinity in Bering Strait. *Geophysical Research Letters* 33 **(**19): L19602. https://dx.doi.org/10.1029/2006GL026612.

Bowden, K. 1965. Horizontal mixing in the sea due to a shearing current. *Journal of Fluid Mechanics* 21 (1): 83–95. https://doi.org/10.1017/S002112065000058.

Coachman, L.K., K. Aagaard, and R.B. Tripp. 1975. *Bering Strait: The Regional Physical Oceanography*. Seattle: University of Washington Press.

Danielson, S.L. 1996. *The Chukchi Sea Tidal Currents* (Master's thesis). Fairbanks, Alaska: University of Alaska Fairbanks.

Danielson, S.L., T.J. Weingartner, K.S. Hedstrom, K. Aagaard, R. Woodgate, E. Curchitser, and P.J. Stabeno. 2014. Coupled wind-forced controls of the Bering–Chukchi shelf circulation and the Bering Strait throughflow: Ekman transport, continental shelf waves, and variations of the Pacific–Arctic sea surface height gradient. *Progress in Oceanography* 125:40–61. https://dx.doi.org/10.1016/j.pocean.2014.04.006.

Denman, K.L., and M. Miyake. 1973. Behavior of the mean wind, the drag coefficient, and the wave field in the open ocean. *Journal of Geophysical Research* 78 (12): 1917–1931. https://dx.doi.org/10.1029/JC078i012p01917.

ERMA. 2015. Atlantic Environmental Response Management Application (web application). National Oceanic and Atmospheric Administration. Retrieved September 2015. http://erma.noaa.gov/arctic.

Fang, Y.-C., T.J. Weingartner, R.A. Potter, P.R. Winsor, and H. Statscewich. 2015. Quality assessment of HF radar–derived surface currents using optimal interpolation. *Journal of Atmospheric and Oceanic Technology* 32:282–296. https://dx.doi.org/10.1175/JTECH-D-14-00109.1.

Ferrari, R., and G. Boccaletti. 2004. Eddy-mixed layer interactions in the ocean. *Oceanography* 17 (3): 12–21. http://dx.doi.org/10.5670/oceanog.2004.26.

Fischer, H.B. 1972. Mass transport mechanisms in partially stratified estuaries. *Journal of Fluid Mechanics* 53 (4): 671–687. https://doi.org/10.1017/S002211207200412.

Fischer, H.B., E.J. List, R.C.Y. Koh, J. Imberger, and N.H. Brooks. 1979. *Mixing in Inland and Coastal Waters.* New York: Academic Press.

Geyer, W.R., R.J. Chant, and R.W. Houghton. 2008. Tidal and spring-neap variations in horizontal dispersion in a partially mixed estuary. *Journal of Geophysical Research* 113 (C7): C07023. http://dx.doi.org/10.1029/2007JC004644.

Gong, D., and R.S. Pickart. 2015. Summertime circulation in the eastern Chukchi Sea. *Deep-Sea Research II* 118:18–31. https://dx.doi.org/10.1016/j.dsr2.2015.02.006.

Gong, D., and R.S. Pickart. 2016. Early summer water mass transformation in the eastern Chukchi Sea. *Deep-Sea Research II* 130:43–55. https://dx.doi.org/10.1016/j.dsr2.2016.04.015.

Gregg, M. 1999. Uncertainties and limitations in measuring ϵ and χT. *Journal of Atmospheric and Oceanic Technology* 16:1483–1490. https://doi.org/10.1175/1520-0426(1999)016<1483:UALIMA>2.0.CO;2.

Hauri, C., P. Winsor, L.W. Juranek, A.M.P. McDonnell, T. Takahashi, and J.T. Mathis. 2013. Wind-driven mixing causes a reduction in the strength of the continental shelf carbon pump in the Chukchi Sea. *Geophysical Research Letters* 40 (22): 5932–5936. https://dx.doi.org/10.1002/2013gl058267.

Hunkins, K.L. 1965. Tide and storm surge observations in the Chukchi Sea. *Limnology and Oceanography* 10 (1): 29–39. http://dx.doi.org/10.4319/lo.1965.10.1.0029.

Johnson, W.R. 1989. Current response to wind in the Chukchi Sea: A regional coastal upwelling event. *Journal of Geophysical Research* 94 (C2): 2057–2064. http://dx.doi.org/10.1029/JC094iC02p02057.

Kawaguchi, Y., S. Nishino, and J. Inoue. 2015. Fixed-point observation of mixed layer evolution in the seasonally ice-free Chukchi Sea: Turbulent mixing due to gale winds and internal gravity waves. *Journal of Physical Oceanography* 45:836–853. https://dx.doi.org/10.1175/JPO-D-14-0149.1.

Ledwell, J.R., T.F. Duda, M.A. Sundermeyer, and H.E. Seim. 2004. Mixing in a coastal environment: 1. A view from dye dispersion. *Journal of Geophysical Research* 109:C10013. https://dx.doi.org/10.1029/2003JC002194.

Lueck, R.G., F. Wolk, and H. Yamazaki. 2002. Oceanic velocity microstructure measurements in the 20th century. *Journal of Oceanography* 58:153–174. https://dx.doi.org/10.1023/A:1015837020019.

Martini, K.I., H.L. Simmons, C.A. Stoudt, and J.K. Hutchings. 2014. Near-inertial internal waves and sea ice in the Beaufort Sea. *Journal of Physical Oceanography* 44:2212–2234. https://dx.doi.org/10.1175/JPO-D-13-0160.1.

Mudge, T.D., A. Slonimer, J. Barrette, N. Milutinovic, D. Sadowy, and K. Borg. 2017. Analysis of ice and metocean measurements, Chukchi Sea 2014–2015, for BOEM. Project report. Bureau of Ocean Energy Management, Anchorage, Alaska. ASL Environmental Sciences Inc., Victoria, B.C.

Münchow, A., and E.C. Carmack. 1997. Synoptic flow and density observations near an Arctic shelf break. *Journal of Physical Oceanography* 27:1402–1419. https://doi.org/10.1175/1520-0485(1997)<1402:SFADON>2.0.CO;2.

Okubo, A.1973. Effect of shoreline irregularities on streamwise dispersion in estuaries and other embayments. *Netherlands Journal of Sea Research* 6:213–224. https://doi.org/10.1016/0077-7579(73)90014-8.

Osborn, T.R. 1980. Estimates of the local rate of vertical diffusion from dissipation measurements. *Journal of Physical Oceanography* 1:83–89. https://dx.doi.org/10.1175/1520-0485(1980)010<0083:EOTLRO>2.0.CO;2.

Paquette, R.G., and R.H. Bourke. 1974. Observations on the coastal current of Arctic Alaska. *Journal of Marine Research* 32 (2): 195–207.

Pickart, R.S., L.J. Pratt, D.J. Torres, T.E. Whitledge, A.Y. Proshutinsky, K. Aagaard, T.A. Agnew, G.W.K. Moore, and H.J. Dail. 2010. Evolution and dynamics of the flow through Herald Canyon in the western Chukchi Sea. *Deep Sea Research Part II: Topical Studies in Oceanography* 57 (1–2): 5–26. https://dx.doi.org/10.1016/j.dsr2.2009.08.002.

Pingree-Shippee, K.A., N.J. Shippee, and D.E. Atkinson. 2016. Overview of Bering and Chukchi Sea wave states for four severe storms following common synoptic tracks. *Journal of Atmospheric and Oceanic Technology* 33:283–302. https://dx.doi.org/10.1175/JTECH-D-15-0153.1.

Rainville, L., and R.A. Woodgate. 2009. Observations of internal wave generation in the seasonally ice-free Arctic. *Geophysical Research Letters* 36:L23604. https://dx.doi.org/10.1029/2009GL041291.

Simpson, J.H., W.R. Crawford, T.P. Rippeth, A.R. Campbell, and J.V. Cheok. 1996. The vertical structure of turbulent dissipation in shelf seas. *Journal of Physical Oceanography* 26:1579–1590. https://dx.doi.org/10.1175/1520-0485(1996)026<1579:TVSOTD>2.0.CO;2.

Spall, M.A. 2007. Circulation and water mass transformation in a model of the Chukchi Sea. *Journal of Geophysical Research* 112:C05025. https://dx.doi.org/10.1029/2005JC003364.

Sumer, S.M., and H. B.Fischer. 1977. Transverse mixing in partially stratified flow. *Journal of the Hydraulics Division* 103:587–600.

Sundermeyer, M.A., and J.R. Ledwell. 2001. Lateral dispersion over the continental shelf: Analysis of dye release experiments. *Journal of Geophysical Research* 106 (C5): 9603–9621. https://dx.doi.org/10.1029/2000JC900138.

Sverdrup, H.U. 1926. *Dynamics of Tides on the North Siberian Shelf. Results from the Maud Expedition.* Geofysiske Publikasjoner 4(5).

Timmermans, M.-L., and P. Winsor. 2013. Scales of horizontal density structure in the Chukchi Sea surface layer. *Continental Shelf Research* 52:39–45. https://doi.org/10.1016/j.csr.2012.10.015

Tolman, H.L. 1997. User manual and system documentation of WAVEWATCH-III version 1.15. NOAA / NWS / NCEP / OMB Technical Note 151.

Webb, D.C., P.J. Simonetti, and C.P. Jones. 2001. SLOCUM: an underwater glider propelled by environmental energy. *IEEE Journal of Oceanic Engineering* 26:447–452. https://dx.doi.org/10.1109/48.972077.

Weingartner, T., K. Aagaard, R. Woodgate, S. Danielson, Y. Sasaki, and D. Cavalieri. 2005. Circulation on the north central Chukchi Sea shelf. *Deep Sea Research Part II: Topical Studies in Oceanography* 52 (24–26): 3150-3174. https://dx.doi.org/10.1016/j.dsr2.2005.10.015.

Weingartner, T., P. Winsor, R.A. Potter, H. Statscewich, and E.L. Dobbins. 2012. Application of high frequency radar to potential hydrocarbon development areas in the northeast Chukchi Sea. Final report. U.S. Department of the Interior, Alaska Outer Continental Shelf Region Contract M09AC15207, OCS Study BOEM 2012-079.

Weingartner, T., E. Dobbins, S. Danielson, P. Winsor, R. Potter, and H. Statscewich. 2013. Hydrographic variability over the northeastern Chukchi Sea shelf in summer-fall 2008–2010. *Continental Shelf Research* 67:5–22. https://dx.doi.org/10.1016/j.csr.2013.03.012.

Weingartner, T., C. Irvine, E. Dobbins, S. Danielson, L. DeSousa, B. Adams, R. Suydam, and W. Neatok. 2015. Satellite-tracked drifter measurements in the Chukchi and Beaufort Seas. Final report. U.S. Department of the Interior, Alaska Outer Continental Shelf Region Contract M11AC00001, OCS Study BOEM 2015-022.

Weingartner, T.J., R.A. Potter, C.A. Stoudt, E.L. Dobbins, H. Statscewich, P.R. Winsor, T.D. Mudge, and K. Borg. 2017. Transport and thermohaline variability in Barrow Canyon on the Northeastern Chukchi Sea Shelf. *Journal of Geophysical Research* 122:3565–3585. https://dx.doi.org/10.1002/2016JC012636.

Winsor, P., and D.C. Chapman. 2004. Pathways of Pacific water across the Chukchi Sea: A numerical model study. *Journal of Geophysical Research* 109:C03002. https://dx.doi.org/10.1029/2003JC001962.

Woodgate, R.A., K. Aagaard, and T.J. Weingartner. 2005. A year in the physical oceanography of the Chukchi Sea: Moored measurements from autumn 1990–1991. *Deep Sea Research Part II: Topical Studies in Oceanography* 52 (24–26): 3116–3149. https://doi.org/10.1016/j.dsr2.2005.10.016.

Woodgate, R.A., K. Aagaard, and T.J. Weingartner. 2006. Interannual changes in the Bering Strait fluxes of volume, heat and freshwater between 1991 and 2004. *Geophysical Research Letters* 33:L15609. https://dx.doi.org/10.1029/2006GL026931.

Young, W.R., P.B. Rhines, and C.J.R. Garrett. 1982. Shear-flow dispersion, internal waves and horizontal mixing in the ocean. *Journal of Physical Oceanography* 12:515–527. https://doi.org/10.1175/1520-0485(1982)012<0515:SFDIWA>2.0.CO;2